UNIVERSITY OF BERGEN

MASTER THESIS

Post-Caledonian topographic and structural evolution of the Nordfjord region in Western Norway – Insights from Apatite Fission Track thermochronology and structural mapping

Anna Katharina Karoline von der Ahe

Department of Earth Science, February 2023

Supervision: Prof. Dr. Joachim Jacobs & Åse Hestnes

Abstract

The topographic and tectonic post-Caledonian evolution of western Norway is still not fully understood. Improving resolution in the low-temperature thermochronological database, this study focuses on a constrained area around the Nordfjord in western Norway, where little previous data is available. Aim of the study is to understand the development of the Nordfjord region in the frame of the post-Caledonian evolution of western Norway, studying vertical movements, fault activity and the tectonic architecture.

8 samples at elevations from 3 to 56 masl were analysed by LA-ICP-MS apatite fission track dating. The obtained ages range from 133 ± 9 to 325 ± 41 Ma (Middle Carboniferous to Early Cretaceous). Most ages are Late Triassic to Late Jurassic. The ages are strongly offset, suggesting fault activity during Triassic-Cretaceous between samples. A reliable number of track lengths could be measured for 3 samples. Mean track lengths are rather short, ranging from 11.91± 1.60 to 12.29±1.67 µm and suggesting comparably slow cooling through the PAZ. Thermal history modelling of these 3 samples suggests a period of faster cooling (1.5-2°C/Ma) driven first by exhumation due to Devonian extension and then Permian-Triassic flexural rift plank uplift, followed by a period of slower cooling (0.2-0.4°C/Ma) from 250-150 Ma until present. Differences between the models have been explained by localized faulting during exhumation.

Structural geological field work provided an extensive database of foliation, fracture and slicken fibre lineation measurements, accompanied with interpretation of fault kinematics based on slicken fibres. Essentially two main types of fractures have been observed in the: 1) ~ N-S-striking fractures, with a steep dip to the west and mainly normal kinematics, closely followed by sinistral kinematics. 2) E-W to NE-SW striking, less steeply dipping fractures with mainly sinistral kinematics and some normal kinematics in the south, often parallel ductile precursors. Whereas the N-S trending faults are interpreted to have formed possibly as early as Late Devonian-Carboniferous, but mainly in relation to rifting in the North Sea, NE-SW and E-W trending were most likely formed during Devonian extension. The latter are suggested to have been reactivated as normal or strike-slip faults. Based on the kinematics a transtensional regime is suggested for the area. A model of localized normal faulting along preferential oriented structures and sinistral strike-slip kinematics along less preferential oriented precursor structures, the latter balancing and releasing stress built up by normal faulting and differential extension, is suggested for the study area during post-Caledonian. The study stresses the importance of structural inheritance, influencing fault orientations and perturbing the regional stressfield locally, as has been suggested for the North Sea.

Acknowledgements

I would like to thank Cecily Ogunjobi and Emil Sivertsvik for their company and hard work in the field. I would also like to thank Åse Hestens, Andreas Lambach Viken and Leif-Erik Pedersen for sample preparation and measurements. I also thank the DAAD for supporting me with a generous scholarship. My biggest thanks go to Emil for all his support and patience.

Table of contents

Abstract 2
Acknowledgements 4
List of abbreviations 8
1 Introduction 9
2 Geological Setting 11
2.1 Proterozoic evolution and Caledonian orogeny 11
2.2 Post-Caledonian structural evolution 12
2.2.1 Devonian post-orogenic extension 12
2.2.2 Palaeozoic and Mesozoic extension linked to rift development 14
2.3 Geological overview of the study area 15
2.4 Apatite Fission Track studies in Western Norway 16
3 Methods 18
3.1 Apatite fission track dating 18
3.1.1 Theoretical background 18
3.1.2 Sample preparation 23
3.1.3 Fission track counting and length measurement 24
3.1.4 Thermal age calculation and Thermal history modelling 27
3.2 Structural geology 28
3.2.1 Fieldwork 28
3.2.2 Data processing 31
4 Results 31
4.1 Apatite fission track analysis 31
4.1.1 Sample quality 32
4.1.2 Thermal ages and track lengths 35
4.1.3 Factors influencing age and track lengths 36
4.2 Thermal history modelling 38
4.3 Field work 42
4.3.1 Geology of the study area: Lithologies, foliation and ductile kinematics 42
4.3.2 Mineralizations on fracture planes 45
4.3.3 Fractures and brittle kinematics 46
4.3.4 Subregions showing different structural trends 50
5 Discussion and Interpretation 64
5.1 Reliability and validity 64
5.1.1 Apatite fission track analysis 64

5.1.2 Thermal history modelling 66
5.1.3 Structural field work 67
5.2 Implications from AFT ages 68
5.2.1 Age interpreation 68
5.2.2 Age offsets and fault activity 69
5.2.3 Thermal history 71
5.3 Structural activity in the region 74
5.3.1 Paleo-stress field and kinematic regime 75
5.4 Implications from both structural geology and AFT dating 78
6 Conclusions 80
References 81
Appendix 88
A Length measurements 88
A1 Sample VAH_23 88
A2 Sample VAH_26 89
A3 Sample VAH_31 90
A4 Sample VAH_42 91
A5 Sample MLM_134 94
A6 Sample VAH_48 97
A7 Sample VAH_44-2 98
A8 Durango A2 Standard 101
B Count data 104
B1 Sample VAH_23 104
B2 Sample VAH_26 107
B3 Sample VAH_31 110
B4 Sample VAH_42 113
B5 Sample MLM_134 116
B6 Sample VAH_48 119
B7 Sample VAH_78 122
B8 Sample VAH44_2 125
C Durango A2 Standard count data 128
D LA-ICP-MS analysis 132
D1 Instrumentation and operational settings for apatite trace element analysis 132
D2 Quality control / validation 134
E Structural field data 138

List of abbreviations

AFT - Apatite fission track

BASZ - Bergen Arc Shear Zone

EDM - external detector method

HP - High-pressure

LA-ICP-MS - laser ablation inductively coupled plasma mass spectrometry

LAFT - AFT dating using LA-ICP-MS

MTL -Mean track length

MTFC -Møre-Trøndelag fault complex

NSDZ - Nordfjord- Sogn Detachment Zone

PAZ - partial annealing zone

SZ - shear zone

TINT - track-in-track

TINCLE - track-in-cleavage

UHP - Ultra-high pressure

WGR - Western Gneiss Region

1 Introduction

The tectonic and topographic evolution of western Norway following the Caledonian orogenic collapse is still incompletely understood. Low-temperature thermochronology can give insights about vertical movements and fault activity, where due to a lack of sediment cover, no other source of information is available. Previously published studies came to very different or even opposing conclusions from studying low-temperature thermochronological data. The still developing method allows a wide range of interpretation and studies show a strong variation in approaches to data handling and modelling, allowing different results and conclusions from the same dataset. As a result, low-temperature thermochronological data has so far failed to provide clear arguments in the debate around the post-Caledonian tectonic and topographic evolution of western and southern Norway. Studies argument for evolutions more or less in line with one of the two endmember models that have been presented: The Classical model (e.g., Japsen & Chalmers, 1999; Gabrielsen et al., 2010) and a recently developed ICE (Isostacy-Climate-Erosion) model (e.g., Nielsen et al., 2009; Steer et al., 2012). After the Classical model, the Caledonides were eroded to sea level during port-Caledonian times, forming a peneplain surface, which was tectonically uplifted in Neogene to the present elevation. The ICE model proclaims a gradual erosion of the Caledonides to the present-day topography, carved by glacial and periglacial erosion around and above the equilibrium line altitude.

It is important to understand a region's structural framework when interpreting thermochronological data. The topographical evolution can be strongly obscured if the area is treated as an undissected block without internal vertical translations. Rohrmann et al. (1995) investigated the topographical evolution of the entire southern Norway, however, did not take faulting into account. Local apatite fission track studies in western Norway, focusing also on the brittle structural framework, exist for the Bergen area (Ksienzyk et al., 2014), the Hardangerfjord area (Johannessen et al., 2013) and the Møre-Trøndelag fault complex (Redfield et al., 2004, 2005b). These fours studies stressed the importance of faulting in the interpretation of fission track data in western Norway. They support a model of gradual erosion after the Caledonian orogeny to the present-day topography, dissected by faulting, without the formation of peneplains.

Another regional study, Green et al. (2022), studied an immense database of previously published and new apatite fission track data across all of Fennoscandia, defining reoccurring periods of regional burial and exhumation. They also observed kilometre-scale differential

vertical displacements between their data. However, they also argumented for a history of reoccurring peneplanation and uplift cycles, of which the latest cycle was a peneplain created by early Miocene exhumation, followed by Pliocene uplift and dissection, resulting in the modern landscape of southern Norway and Sweden. Their work is in favour of the Classical model.

This study has the aim to fill the geographical gap between the local, detailed studies in western Norway and to add the puzzle piece of the Nordfjord region (see Figure 1). Heart of the study is the analysis of 8 apatite fission track samples, complemented with extensive field work to gain insight into the brittle structural architecture and kinematics. The study does not have the aim to find the solution to the debate around the two endmember models, but to investigate the relationship between thermochronological data and structural geology in a constrained, local area in western Norway, and to contribute to the overall database in order to allow for more confined interpretations in regional studies. An extensive AFT database without lateral gaps, ideally using commonly agreed methodology, and complemented with structural data, will be the best approach to unravel the post-Caledonian tectonic and topographic evolution.

The main aim of this study is to understand the development of the Nordfjord region in the frame of the post-Caledonian evolution of western Norway, studying vertical movements, fault activity and the tectonic architecture.

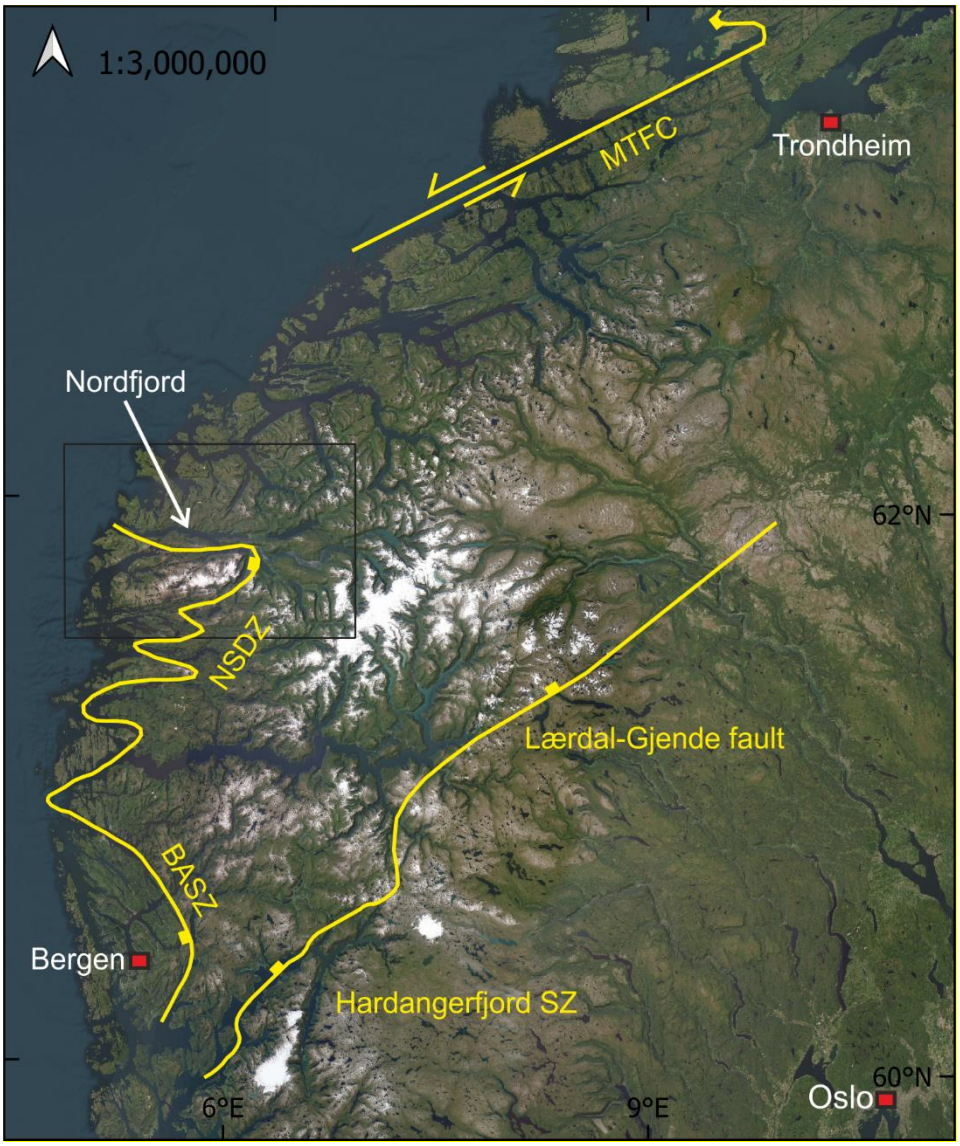

Figure 1: Overview map of western Norway, showing the study area marked by a rectangle. Devonian extensional fault system after Wiest et al. (2021) consisting of the BASZ – Bergen arc shear zone, NSDZ – Nordfjord Sogn detachment zone, Hardangerfjord shear zone, Lærdal-Gjende fault and Møre-Trændelag fault complex.

2 Geological Setting

2.1 Proterozoic evolution and Caledonian orogeny

The present surface geology of Western Norway can be roughly subdivided into Devonian basins, Caledonian thrust nappes and a basement window, the Western Gneiss Region (WGR).

The Baltican basement of western Norway formed essentially during Gothian times (1.66-1.52 Ga) at the accretionary margin of Fennoscandia located at the outer edge of the Columbia supercontinent (Roberts & Slagstad, 2015). Accretion ended with the Sveconorwegian orogeny (1.14-0.9 Ga), which reassembled, deformed and metamorphosed

the Baltican basement and led as part of the Grenvillian orogeny to the formation of the supercontinent Rodinia, with Fennoscandia at the interior (Bingen et al., 2008; Roberts & Slagstad, 2015). During the break-up of Rodinia, the Iapetus Ocean opened between Baltica and Laurentia from the Late Neoproterozoic (Cawood, 2005).

From Late Cambrian, the Iapetus Ocean was progressively closing, setting the stage for the Caledonian orogeny which culminated in the continent-continent collision of Laurentia and Baltica during the Scandian phase (425-405 Ma; Fossen et al., 2016). During the early stages of collision, the Baltican margin was partially subducted below Laurentia, resulting in the regional occurrence of ultra-high-pressure rocks in the WGR (Hacker et al., 2010). Large-scale SE-ward thrusting produced a stack of nappes, resting upon a basal decollement (see Figure 2), formed as a sliding surface in the Neoproterozoic – Silurian metasedimentary basement cover (Gee et al., 2008). The nappes are derived locally from the Baltican margin, but also from the Iapetus Ocean and the Laurentian plate and have been subdivided by Gee et al. (1985) into Lower, Middle, Upper and Uppermost allochthons (Gee et al., 2008).

2.2 Post-Caledonian structural evolution

2.2.1 Devonian post-orogenic extension

The Caledonian SE directed compressional fabrics are overprinted and obliterated by post-orogenic extension with a weaker metamorphic imprint, commencing from c. 405 Ma (Fossen, 1992, 2000). Early extension included a reactivation of the basal decollement leading to backsliding of the Caledonian orogenic wedge towards NW, eduction of the Baltican basement, and formation of micro- to mesoscale folds and shear bands with top-to-the-northwest and regionally top-to-the-west kinematics (Mode I extension after Fossen 1992; Fossen, 2000, 2017; Figure 2). Exhumation of the subducted hinterland led to a rotation of the basal decollement to sub-horizontal, resulting in an orientation less favourable for slip (Fossen, 2000). The ongoing Devonian crustal collapse therefore continued with the formation of new, steeper dipping, extensional basement shear zones, cutting the old decollement and causing folding and faulting also in the nappes on top (Mode II; Fossen, 1992, 2000, 2010). The structures itself comprise wide, km-scale zones of mylonites. All Mode II shear zones show hinterland directed hanging wall translations and dip towards NW to W (Fossen, 2000, 2017). Major Mode II shear zones from north to south are the Møre-Trøndelag fault complex, the Nordfjord Sogn Detachment Zone, the Bergen Arc Shear Zone and the Hardangerfjord Shear Zone (Fossen, 2010; Figure 1). The brittle surfacing expressions of those shear zones have created a network of Devonian supradetachment basins,

some of which in the hanging wall of the Nordfjord Sogn detachment zone were preserved (e.g., the Hornelen basin in the study area; Fossen et al., 2017). Ductile Mode I and II extension was followed by the formation of brittle faults during the progressing Devonian cooling, enabling the continuation of NW-SE extension (Mode III; Fossen, 2000, 2017). The faults are interpreted by Fossen (2000) and Fossen et al. (2017) to have formed when the today exposed part of the crust passed the brittle-ductile transition. Most Mode III faults are

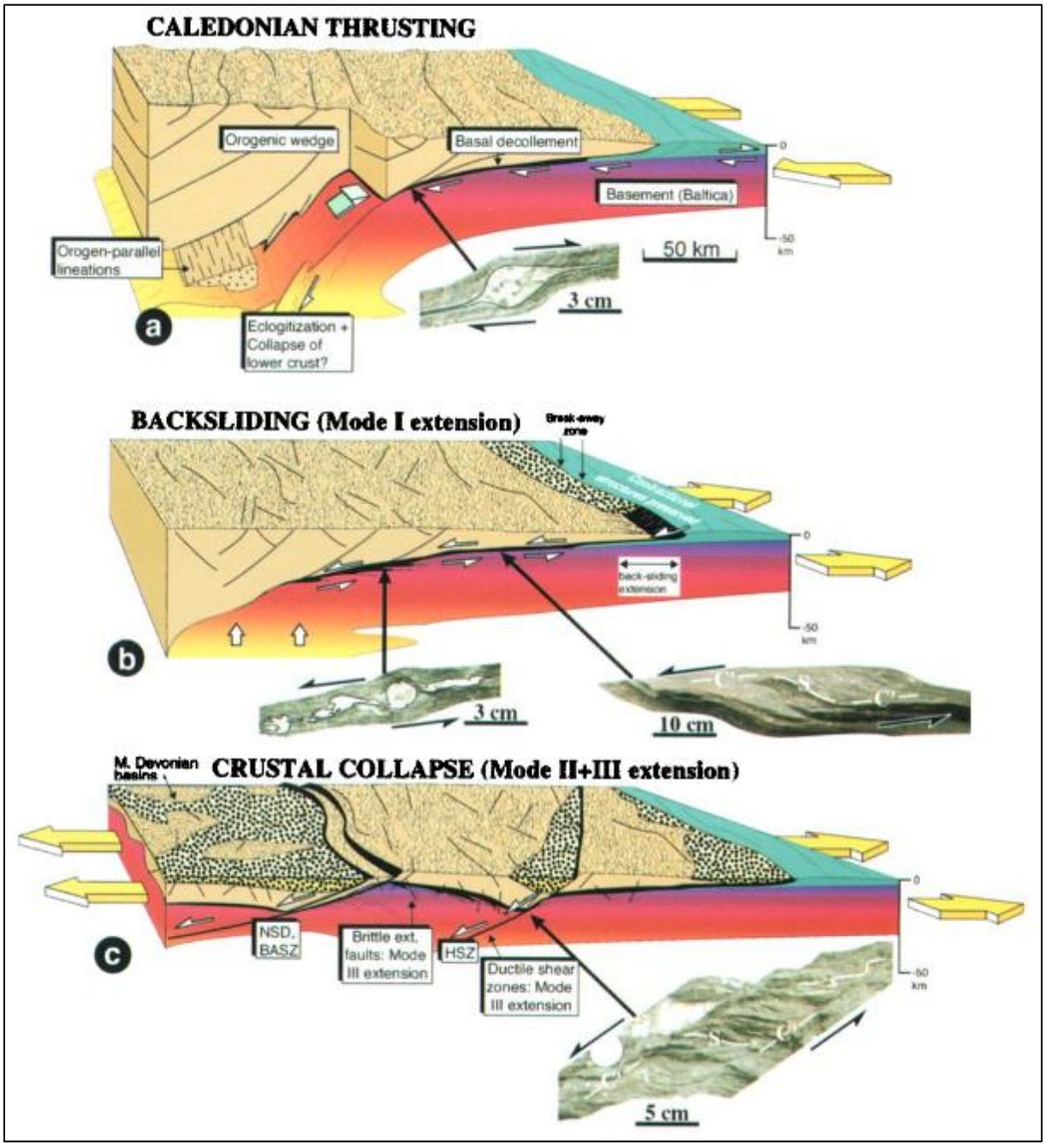

Figure 2: Schematic illustration showing typical structures and kinematics of a: Caledonian thrusting and b, c: Devonian extension Mode I (ductile), Mode II (ductile) and Mode III (brittle) following Caledonian collision. Photographs of characteristic ductile textures of the Caledonian collision and Mode I and II extension are additionally included. From Fossen (2000).

steep and crosscut Mode II shear zones, however, the largest Mode III faults such as the Lærdal-Gjende fault or the Hornelen fault, developed inside the wide, exhumed Mode III shear zones, following their low-angle orientation (Fossen et al., 2017, Fossen et al., 2021). The faults are trending mostly NE-SW and show striated surfaces with epidote mineralization (Fossen, 2000).

2.2.2 Palaeozoic and Mesozoic extension linked to rift development

Offshore, the initiation of extension in the northern North Sea region resulted in two main rift phases, rift phase 1 in late Permian-Early Triassic and rift phase 2 during Late Jurassic-Early Cretaceous (Færseth, 1996, Phillips et al., 2019). Rifting in the North Sea was deserted and continued in early Cretaceous in the northwest with the future North Atlantic and succeeded in Eocene with the continental break-up of Pangea (Dore et al., 1999). The direction of the ongoing extension in the North Atlantic is NW-SE until present (Dore et al., 1999). The Oslo rift to the east was active from Late Carboniferous to Early Triassic (Larsen et al., 2008), but it has not been shown as of now, that it has influenced western Norway. Onshore Norway became the eastern rift margin of the North Sea rift with beginning extension (Fossen et al., 2021). Early extension led to a reactivation of Devonian extensional structures as low-angle normal faults (Fossen et al., 2017). New N-S trending, coast parallel faults and fractures cutting older NE-SW trending faults show E-W extension related to rift phase 1 (Fossen et al., 2017). The timing of rift phase 1 is well documented in western Norway due to the intrusion of around rift parallel dikes in Permian and Triassic (Fossen & Dunlap, 1999). Fossen et al. (2021) confirmed onshore fault activity from late Devonian, with distinct Permian and Jurassic peaks in the early stages of the two rift phases, suggesting that localised rifting in the northern North Sea was preceded by widespread extension in an area significantly larger than the resulting rift. After their study, the onshore basement was significantly involved in North Sea rifting since 70% of illite K–Ar ages of dated faults showed Permian-Early Cretaceous ages and the fault density is increasing westward towards the coast and the main rift (Fossen et al., 2021). Ksienzyk et al. (2016) also dated illite gouges of 9 faults around Bergen and determined four periods of onshore fault activity. A first Late Devonian–Early Carboniferous (>340 Ma) period is still related to the decreasing Caledonian orogenic collapse. Fault activity in the latest Carboniferous–Mid Permian (305–270 Ma) is widely distributed and marks a second period correlating with the onset of phase 1 rifting. Some onshore fault activity can be shown for the Late Triassic–Early Jurassic (215–180 Ma), between rift phase 1 and 2, however, this period is poorly documented onshore. An increase in faulting in the Early

Cretaceous (120–110 Ma) could either be a late response to rift phase 2 of the North Sea or correlated to initiation of rifting in the North Atlantic (Ksienzyk et al., 2014).

2.3 Geological overview of the study area

The study area is located in western Norway, stretching over a constrained region with the Nordfjord at the centre (Figure 1). The Devonian Hornelen basin is situated centrally in the study area, south of the Nordfjord (Figure 3). To the south, the basin is juxtaposed to Caledonian nappes. A major part of the study area consists of basement rocks of the Western Gneiss Region (WGR). The foliation of the WGR is trending around E-W (Labrousse et al., 2004) related to the Nordfjord-Sogn Detachment zone and the Nordfjord Shear Zone (Wiest et al., 2021).

The Hornelen Basin is framed by the low-angle brittle Hornelen detachment fault. The detachment is cut by steeper brittle faults, the S-dipping Bortnen fault at the northern side of the Hornelen Basin and the NNW-dipping Haukå Fault at the southern side (Fossen et al., 2017). The Haukå fault and the Eikefjord fault in the south form a major horst structure (Figure 3), the narrowest part of which is the Florø Horst (Fossen et al., 2017). Normal down-to-the-north offset along the Haukå fault exceeds 500 m in the eastern part (Braathen, 1999). The brittle-ductile Bortnen fault shows K-feldspar-epidote alteration, breccia and pseudotachylite, while movement along the fault was interpreted to be sinistral with a minor normal component (Young et al., 2011; Fossen et al., 2017). Fossen et al. (2021) dated a close, subparallel fault to an age of 57 Ma, which was the youngest fault activity reported in SW-Norway up to that date.

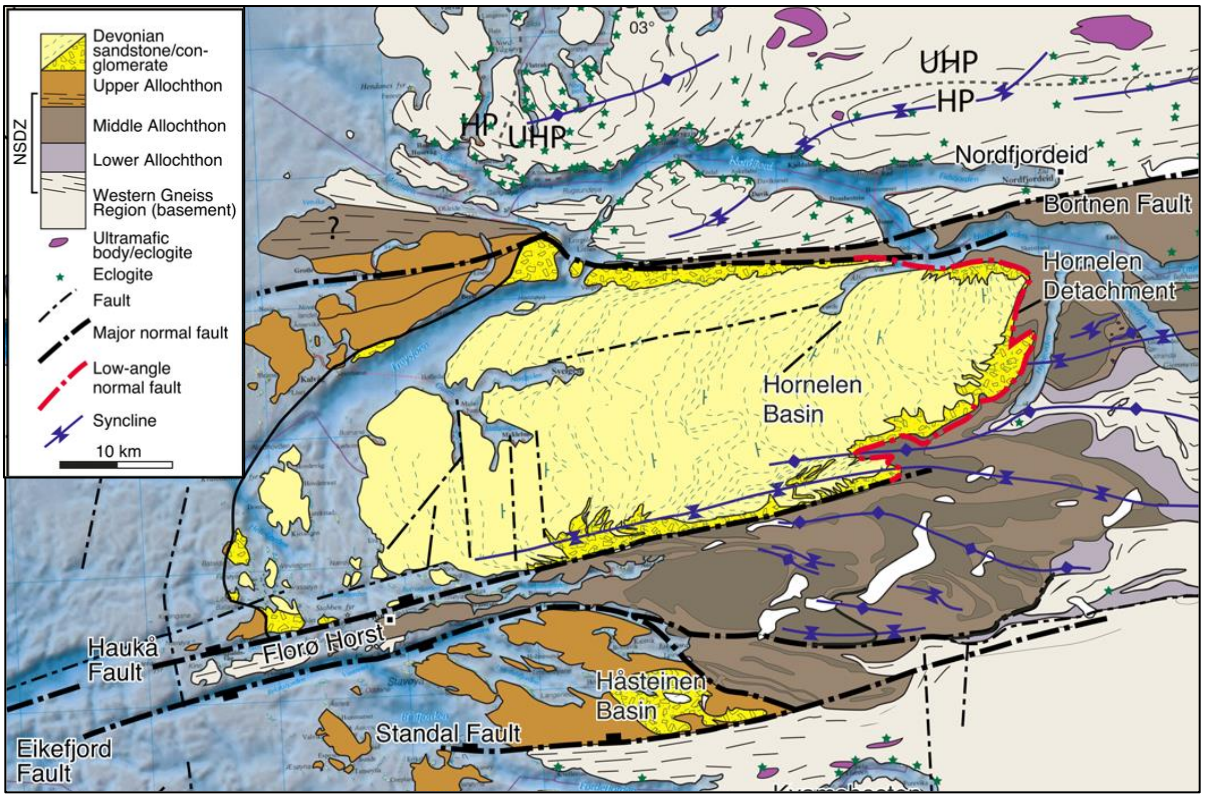

Figure 3: Geological overview of the study area showing structural domains and major faults. Modified after Fossen et al. (2017)

2.4 Apatite Fission Track studies in Western Norway

Apatite Fission Track studies produced opposing conclusions about the topographic evolution of Norway following the Devonian extension.

Rohrmann et al. (1995) investigated 45 apatite fission track basement samples distributed across all southern Norway and found two main events of rapid exhumation. They correlated the first event, during Triassic in the south and east and during Jurassic in the west, to rift flank uplift and erosion. A second event in Neogene from about 30 Ma, produced a domal pattern of AFT ages following today's topography, with the youngest ages at low elevations in the centre of Southern Norway. The Neogene domal uplift was interpreted to correlate with mantle convection and plate reorganizations in the North Atlantic, based on the observation that these domes exist in several regions around the North Atlantic, and was overprinted by Plio-Pleistocene glacial erosion (Rohrmann et al., 1995). While the earlier event was obtained from studying AFT ages directly, the second event was inferred from thermal history modelling of ages and track length distributions. The study by Rohrmann et al. (1995) was followed by more local studies, covering smaller areas in detail. Ksienzyk et al. (2014) investigated apatite fission track and apatite and zircon (U–Th)/He ages of 59 samples located around Bergen. Using thermal modelling of the data, they also found a period of rapid

exhumation (2-3°C/Ma) correlating to rifting in North Sea during Permian to early Jurassic which was stronger recorded in coastal samples. Since Jurassic times, the coastal samples were close to the surface and were reburied (up to 30-50°C) during Cretaceous to earliest Paleogene, whilst inland samples showed little response to rifting and were slowly and consistently exhumed (1,8°C/Ma) during Jurassic and Cretaceous, remaining below the surface until the Cenozoic (Ksienzyk et al., 2014). Johannessen et al. (2013) investigated 32 samples more inland in the Hardangerfjord region using the same methods as Ksienzyk et al. (2014) and reported two distinct periods of increased cooling (2–6°C/Ma) during Permian-Triassic (flexural rift shoulder uplift) and latest Cretaceous-Cenozoic. Both Ksienzyk et al. (2014) and Johannessen et al. (2013) stressed the importance of fault activity as the studied AFT ages were offset across faults, concluding that the sustained topography was most likely periodically rejuvenated during the Cenozoic because of reoccurring tectonic activity. Also earlier studies by Redfield et al. (2004, 2005b) of AFT thermochronology across the Møre-Trøndelag fault complex, showed a Mesozoic to Cenozoic exhumation history significantly offset across major structural blocks. A recent study by Green et al. (2022) used an immense database of 331 samples from boreholes and exposed basement, cover, and intrusions across all Fennoscandia, including both old and newly acquired AFT data. They concluded with five periods of enhanced exhumation in post-Caledonian times: 311–307 Ma (late Carboniferous), 245–244 Ma (Middle Triassic), 170–167 Ma (Middle Jurassic), 102–92 Ma (mid-Cretaceous) and 23–21 Ma (early Miocene). Enhanced cooling was alternating repeatedly with periods of peneplanation and reburial (Green et al., 2022). These periods are not constraint to rift margins, but extend across all of Fennoscandia (Green et al., 2022). After Green et al. (2022), the early Miocene exhumation resulted in peneplanation of southern Norway and Sweden, before being uplifted in Pliocene. They interpreted their obtained exhumation events as resultant from mantle processes or wide range tectonic stresses since they correlate with similar events all around the North Atlantic (Green et al., 2022). It must be pointed out that Green et al. (2022) did not use thermal history modelling like Rohrmann et al. (1995), Johannessen et al. (2013) and Ksienzyk et al. (2014) in interpreting periods of enhanced cooling, but a different approach of using AFT ages and track length distributions directly. The variation in approaches of dealing with AFT data obscures the comparability and consistency of conclusions made in the studies.

3 Methods

The work for this thesis comprises two methods: Apatite LA-ICP-MS (laser ablation inductively coupled plasma mass spectrometry) fission track dating and structural field work. The workflow for each method will be described in the following.

3.1 Apatite fission track dating

3.1.1 Theoretical background

Apatite fission track (AFT) dating gives insight in the low-temperature thermal history of a rock sample, with a sensitivity to temperatures between ~120 and 60 °C (Wagner et al., 1989). It is based on the formation of lattice defects ('fission tracks') which are trails left behind by the spontaneous fission of ^{238}U contained in apatite. The fission tracks have an initial length of c. 16 µm (Lisker et al., 2009). There will be no record of the thermal history at temperatures above 120 °C in the sample, since fission tracks being formed completely anneal. The clock starts when the sample cools due to uplift and erosion and enters the partial annealing zone (PAZ; ~ 120 - 60 °C; Figure 4). Inside the PAZ, tracks accumulate but shorten at the same time. Annealing ceases at around 60 °C and below that temperature fission tracks continue to accumulate and are almost completely retained (Wagner et al., 1989).

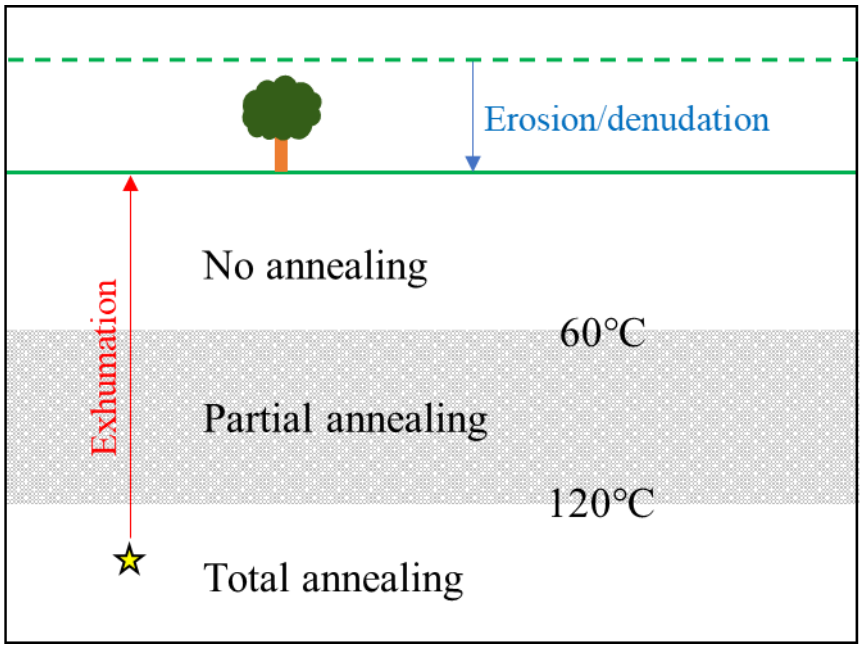

Figure 4: Schematic illustration of the partial annealing zone, erosion/denudation and exhumation of a rock sample (shown as star).

The cooling or heating information obtained by low temperature thermochronology can be used to understand the evolution of the topography in terms of exhumation of the rock sample, in turn allowing for interpretations about tectonic uplift and erosion (denudation), or

sedimentary/tectonic burial (Figure 4). These interpretations are based on assuming a constant geothermal gradient.

By chemical etching the fission tracks can be made visible under the microscope and counted. The thermal 'age' (t) is calculated from the ratio of the density of spontaneous tracks on an internal surface (ρ_s), counted manually, and the abundance of parent ^{238}U [atoms per unit volume] in the apatite crystal (Equation 1 from Cogné et al., 2020). The age equation also requires the total decay constant of ^{238}U (λ_d), the spontaneous fission decay constant of 238U (λ_f), the etchable length (R), and the etch efficiency factor (η).

$$t = \frac{1}{\lambda_d} ln\left(1 + \frac{\lambda_d}{\lambda_f} \frac{\rho_s}{[^{238}U]\, R\, \eta}\right)$$

Equation 1

The established way of determining ^{238}U in the crystal ('External detector method, EDM'; e.g., Hurford and Green, 1982) is to first reveal the geologically formed, spontaneous fission tracks by chemical etching and then induce additional fission tracks by irradiating the sample in a reactor. During thermal neutron irradiation, ^{235}U contained in the crystal will be induced to fission. As the ratio of ^{238}U/^{235}U can be assumed to be constant in nature, the amount of ^{238}U in the crystal can be determined (Hurford, 2019). The amount of ^{235}U in the crystal is obtained from the density of counted induced tracks (ρ_i) in a mica plate that is placed on the sample prior to irradiation and the neutron flux used during irradiation, as countable induced tracks in a dosimeter glass of known U concentration (ρ_d). The use of a ζ (zeta) calibration approach involving dating of samples of known age abolishes the need to determine values for parameters (e.g., λ_f), which are difficult to determine experimentally (Cogné et al., 2020). See the age equation adapted to the EDM below (Equation 2 from Cogné et al., 2020).

$$t = \frac{1}{\lambda_d} ln\left(1 + \lambda_d\, \zeta\, \rho_d\, \frac{\rho_s}{\rho_i}\right)$$

Equation 2

Recent advances in digital imaging and analysis of microscopic images made way for the possibility of using destructive methods such as laser ablation inductively coupled plasma mass spectrometry (LA-ICP-MS) for determining the 238U concentration of the crystal as the studied crystals can be preserved digitally. A system ('Trakscan Plus') that additionally enables fully automated counting of fission tracks, was developed by the Australian scientific instrument manufacturing company 'Autoscan Systems Pty. Ltd' and the fission track dating

group at the University of Melbourne (e.g., Gleadow et al., 2018). A major advantage of AFT dating using LA-ICP-MS (LAFT) compared to the EDM is that it reduces the time required for analysis, mainly because it avoids the irradiation process in a reactor and the associated "cooling" period afterwards. It additionally avoids dependency on another facility providing irradiation services, thereby enabling the whole analysis being carried out in one place. Comparisons of the results of the traditional EDM and LAFT dating yielded a high degree of agreement, thereby validating the approach and allowing for routine use in AFT dating (e.g., Guibaldo et al., 2022).

Absolute LAFT ages can be calculated by simply using the fundamental age equation (Equation 1) and directly inserting the ^{238}U concentration. However, the accuracy of this approach is "fundamentally limited by the accuracy of the U concentration measurements, the fission track decay constant and the etching and counting efficiencies", resulting in a potential unquantifiable bias (Veermesch, 2018, p. 1491). These systematic errors can be reduced by normalizing to a standard of known fission track age (e.g., Durango age standard) and defining a new 'zeta' calibration factor (ζ_{ICP}) (Veermesch, 2018). The LAFT single grain ages (t_i) are computed using the following equation after Cogné et al. (2020):

$$t_i = \frac{1}{\lambda_d} ln\left(1 + \lambda_d \, \zeta_{ICP} \, \frac{N_{s,i}}{P_i \, \Omega_i}\right)$$

Equation 3

Here, ζ_{ICP} is the zeta calibration factor based on a LA-ICP-MS age standard, $N_{s,I}$, is the number of counted spontaneous fission tracks for grain i, Ω_i is the area over which tracks were counted on grain i and P_i is the $^{238}U/^{43}Ca$ ratio of grain i (Cogné et al., 2020).

The associated standard error of the single grain age t_i after Cogné et al. (2020) is given by:

$$s_{t_i} = t_i \left[\frac{1}{N_{s,i}} + \left(\frac{S_{P_i}}{P_i}\right)^2 + \left(\frac{S_{\zeta_{ICP}}}{\zeta_{ICP}}\right)^2\right]^{\frac{1}{2}}$$

Equation 4

where $s_{\zeta ICP}$ is the standard error of ζ_{ICP} and s_{Pi} is the analytical error of the LA-ICP-MS measurement of P_i.

Like in the EDM, the zeta calibration factor ζ_{ICP} in LAFT is determined empirically by employing an apatite fission track reference material of known age and using the rearranged age equation:

$$\zeta_{ICP} = \frac{e^{\lambda_d t_{std}} - 1}{\lambda_d \sum N_{s,i} \Big/ \sum P_i \, \Omega_i}$$

Equation 5

where t_{std} is the accepted age of the reference material (Cogné et al., 2020). The associated standard error of the zeta calibration factor is:

$$\sigma_{\zeta_{ICP}} = \left[\frac{\zeta^2_{ICP}}{\sum N_{s,i}} + \zeta^2_{ICP} \frac{\sum \left(S_{P_i} \, \Omega_i\right)^2}{\left(\sum P_i \Omega_i\right)^2} + \left(\frac{\sigma_{t_{std}} \left(e^{\lambda_d t_{std}}\right)}{\sum N_{s,i} \Big/ \sum P_i \, \Omega_i} \right)^2 \right]^{\frac{1}{2}}$$

Equation 6

where σ_{tstd} is the uncertainty of the age standard (Cogné et al., 2020).

The ζ_{ICP} calibration factor has to be determined for every LA-ICP-MS session as plasma tuning conditions may change. The zeta calibration factor can be a major source of uncertainty as it is primarily dependent on the counted spontaneous tracks (Ns) in the age standard. To obtain a reasonable uncertainty, e.g., below 2%, an unreasonably large Ns (> 2500) would need to be counted for every session (Cogné et al., 2020).

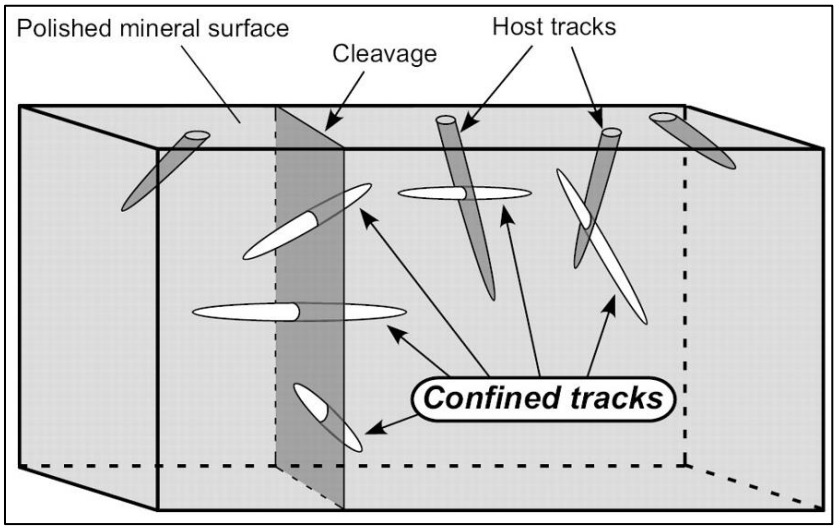

Figure 5: Schematic illustration of fission tracks in an apatite crystal. The top surface would here be the visible etched surface, tracks intersecting it are etched directly by the acid entering through the openings (host tracks). Confined tracks are etched indirectly through other tracks (track-in-track/TINT) or cleavages (tracks-in-cleavage /TINCLE). From Tagami & O'Sullivan (2005).

Chemical etching of the sample surface will also make fission tracks below the surface visible, if these are intersected by fission tracks cut at the surface (host tracks), or by

cracks/cleavage (Figure 5 and 7). Hereby, the acid enters through the surficial opening of another fission track intersecting the horizontal fission track or through cracks, intersecting the horizonal track. Tracks made visible by the first process are called TINT, short for track-in-track, and those made visible by the second process are called TINCLE, short for track-in-cleavage (Tagami & O'Sullivan, 2005). If these confined tracks are horizontal, their length can be measured, since they capture the full length of fission tracks in the sample (Figure 5). These original, entire track lengths can be used to estimate the true length distribution in the sample. The distributions of measured track length give information about the cooling rate i.e., the residence time in the PAZ. Simplified, a relationship between long lengths and fast cooling/exhumation through the PAZ, and short lengths and slow cooling/exhumation i.e., a complex cooling history, can be seen in general.

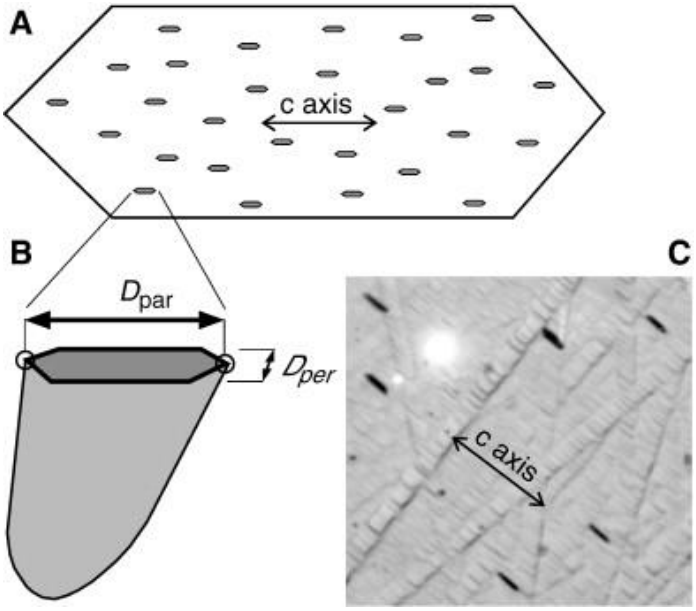

Figure 6: Illustration of the Dpar. A shows a schematic view of the surface of an etched apatite with fission track etch pits. B shows the Dpar measurement of an etch pit and the fission track below surface. C. Photograph of real etch pits in apatite in reflected light. From Sobel & Seward (2010).

Both during counting and during length measurements of fission tracks, the mean diameter of the fission track etch-pits parallel to the crystallographic c-axis is measured (Dpar, see Figure 6). The Dpar value reflects the etching rate which allows conclusions on the chemical compositions of the analysed apatites and thus the annealing kinetics (Donelick et al., 2005). When the apatite grain is cut orthogonal to the c-axis, the openings of the fission tracks cut by the surface will align, with the longest diameter (Dpar) parallel to the c-axis (see Figure 6 and 7). This way, c-axis parallel grains can be identified, which can then be used to count fission tracks and measure horizontal confined tracks (see Figure 7).

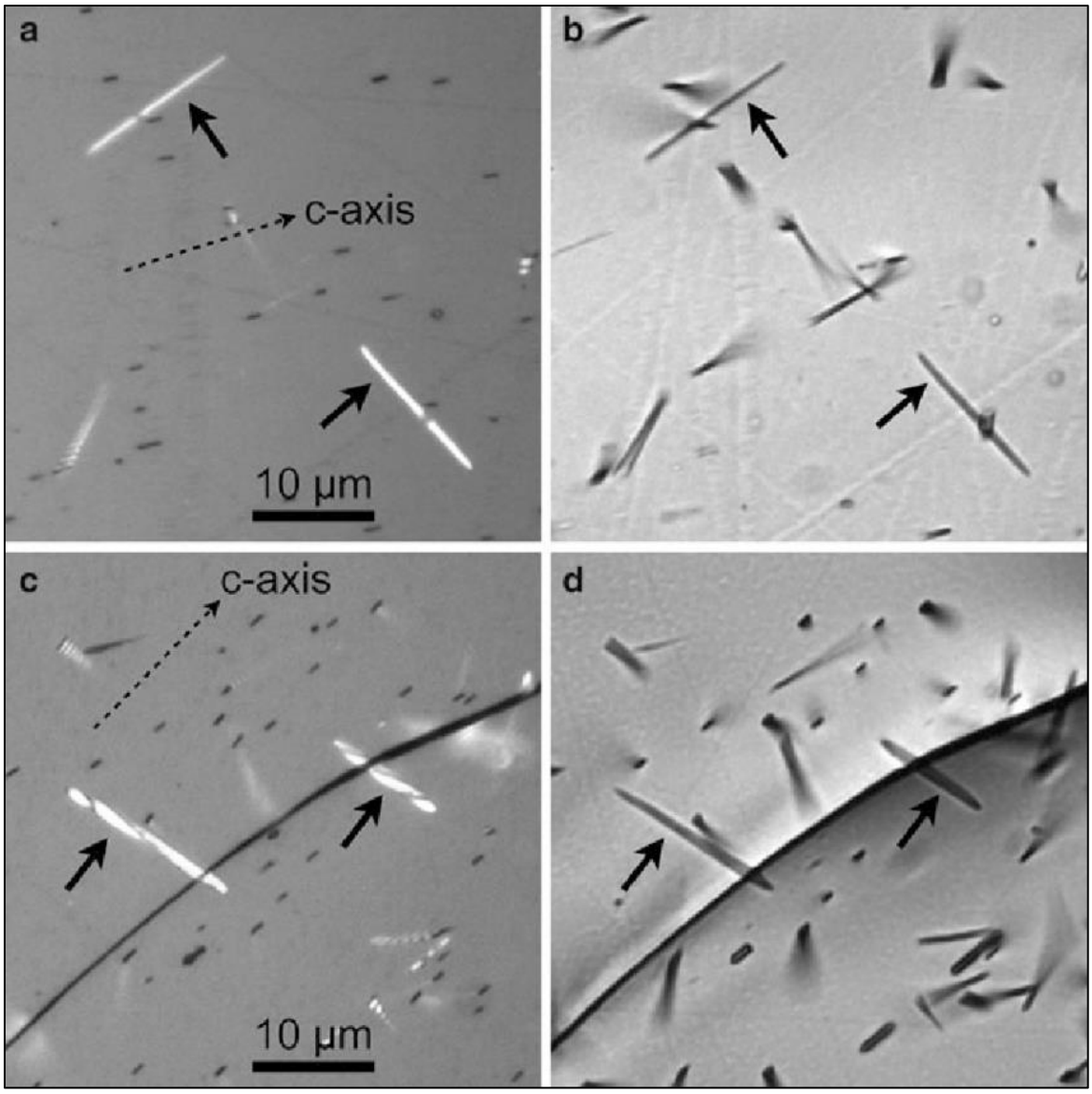

Figure 7: Photomicrographs of confined tracks in apatite. Horizontal TINTs in reflected light (a) and in transmitted light (b). Horizontal TINCLEs in reflected light (c) and in transmitted light (d). The c-axis is shown in the reflected light pictures as it is defined by the elongation of the fission track etch pits at the surface. From Gleadow & Seiler (2014).

3.1.2 Sample preparation

The samples were collected during field work in summer 2019 by Åse Hestnes, who also carried out the sample preparation. At each location, around 1.5-2.5 kg rock material of apatite rich lithologies (e.g., Granite or Gneiss) were sampled. The apatite crystals required for the analysis were extracted from the bulk rock material sample in several steps. Firstly, a separation of the rock sample in size was carried out by crushing to a size of sand and smaller using a disc mill and sieving it afterwards. From the mineral fraction with a size below 315 µm, the fraction with the highest density was extracted using the Wilfley table. Magnetic minerals were removed from the sample in a Frantz magnetic separator using 0.3 A in the first

run and 0.6 A in a second run. If there was still a lot of material left in the sample, the procedure was repeated a third time using 1 A to make the separate even cleaner and remove for example apatite grains with inclusions. The sample was further enriched in apatite by heavy liquid separation with LST (solution of sodium heteropolytungstates in water; density of 2.9 g/cm^3 at 25 °C) and DIM (diiodomethane; with a density of 3.3 g/cm^3) heavy liquids. The method uses the specific density differences of the minerals to first remove all minerals with a density lower than apatite and zircon and then separate zircons from apatites.

The samples were prepared after the workflow of the University of Melbourne using the cold mounting method. For mounting the samples, small glass slides were prepared by rounding the edges and engraving the respective sample names. The epoxy resin ('EpoFix' or 'SpeciFix' by Struers) for cold mounting was prepared by carefully and slowly mixing resin and hardener in the amounts of the volume ratio 15:2 (EpoFix, SpeciFix 25:10). The sample was then sprinkled into a drop of ethanol on a Teflon plate between two glass slides with 1 mm height, serving as 'bridge pillars' later in the process. After the ethanol had evaporated, the sample was completely covered in drops of epoxy resin and the small glass slide was carefully placed on top, resting on the 'bridge pillars' on both sides and topped with a weight. After 8 hours, the mounts were removed from the Teflon plate and polished. This method ensures a uniform and level thickness (1mm) for each mount, without having to cut or grind it later. The process was finalized by polishing to minimize surface relief.

The samples were etched with 5 M HNO3 (nitric acid) at 20 ±0.5 °C by holding them in the acid for 20 seconds and then rinsing them in running water over night. When dried, three marks (copper A's) were glued on the glass mount and used as reference points for alignment during further analysis.

3.1.3 Fission track counting and length measurement

Systems used for fission track analysis

First training, as described below, was carried out on a manual Olympus BX51 microscope installed with a computer driven stage, which is the old system previously used for the EDM.

All further fission track analysis, length measurements and calibrations were carried out using the new Trackscan PlusDeluxe Automated counting system developed for the LAFT method. This system includes a Zeiss Axiolmager Z2m microscope installed with a Zeiss stepper-motor stage and IDS digital colour camera. Even though the system is capable of counting fission tracks automatically, all counting was done manually. The software used is Fission Track Studio by Autoscan Systems Pty, which consists of two programs; TrackWorks and

FastTracks.

Using the new system, the microscope is connected to a pc and can be controlled solely by using the pc. The microscopic images of the thin slices of the samples are displayed on the pc screen. For using the microscope and taking pictures of the sample, the program TrackWorks is used. Pictures can be taken of the reflected and the transmitted light image, the latter as a 'stack' of pictures, allowing to focus into the depth of the crystal. The further analysis is independent of the microscope as by taking the pictures, a 'virtual', 3D sample has been generated. It is carried out on the images using the program FastTracks.

Training component

Training in fission track recognition, counting and length measurement was carried out prior to the work on the samples. The first part of the training was an abbreviated version of the approach previously used to 'calibrate' the counting of the individual worker ('Zeta calibration', e.g., Hurford 1990) for the External detector method (EDM). Using the manual Olympus BX51 microscope, two 'irradiations' (NOB-021 and NOB-017) were counted. Each irradiation consists of dosimeter glasses and two literature-defined standards, a Durango and a Fish Canyon Tuff (FCT) sample. The ages of the standards could not be calculated for comparison because the Zeta-value would be required in the age calculation, and to obtain the Zeta-value, the full calibration would need to be carried out. However, comparing the dosimeter glass count to those obtained by previous workers, it yielded mostly average results. As a Durango standard was counted along with each sample, the obtained age can be compared to literature values, providing an indication whether counting is done reliably. The second part of the training consisted of learning how to count fission tracks on the new microscope and

Fission track analysis and track length measurements

Prior to counting, suitable grains were chosen and pictures of those were taken using TrackWorks. The mounted sample was aligned so that exact coordinates of each grain could be saved. C-axis parallel (see section 3.1.1) apatite grains were selected by manually scanning through the mount and marking the location of ~40 suitable grains. Pictures were taken at 100x magnification in both reflected and transmitted light. Counting was done using the pictures in the program FastTracks. Here, it is possible to zoom in to see details. Firstly, a ROI (region of interest) is defined, which is the area that will be counted, and which will later be 'shot', using the mount, by the laser during LA-ICP-MS in order to determine the Uranium concentration. On the pictures, the c-axis is defined parallel to the Dpar orientation and 6

Dpars per picture/area are measured. C-axis, Dpar measurements and count points, drawn by clicking on the tracks, are drawn onto the pictures in FasTracks. For each sample, 20 areas in c-axis parallel grains were counted. For quality control, for each sample around 20 areas in the Durango standard were counted which were also measured in the same LA-ICP-MS session as the sample. Counting was done analogue to the samples.

For track length measurements the aim was to choose 100 or more measurable lengths in c-axis parallel grains. Only horizontal confined tracks were chosen for measurement. I only measured TINTs and avoided TINCLEs in samples where I found a sufficient number of track lengths (≥100). In samples where it was difficult to find track lengths, I also measured TINCLEs (see section 3.1.1).
The selected confined tracks were marked, and pictures were taken using TrackWorks analogue to the procedure for counting. Track length measurement was carried out in FastTracks. The resolution was higher than during counting as TrackWorks only pictures the area directly around the confined track. Measurement was done by clicking each end point and drawing on the image. If the confined track is not quite horizontal, the program can register the user zooming further into the image until the end point is clear (not blurry), and provide the dip angle of the track. Also here, the c-axis was defined and 6 dpars were measured for each track length.

Calibration

A calibration of the user specific track length measurement had to be carried out in order to be able to use the measured track lengths for thermal history modelling in HefTy. The calibration consisted of measuring 100 track lengths in a sample of the Durango A2 annealed standard. My mean measured track length in the Durango was 15.53 ± 0.94 µm and for the Dpar 1.41±0.06 µm. After Ketcham et al. (2015), a calibrated personal factor of 1.02 (aLen) for track length measurements and of 1.43 (aDpar) for Dpar measurements was obtained, which will be used later in the modelling process. The calibration factors were calculated by dividing the mean measurement obtained by several workers (Ketcham et al., 2015) by the mean measurement obtained by me.

LA-ICP-MS measurement

The ^{238}U concentration was determined using trace element analysis of the apatite grains by LA-ICP-MS after the pictures of the samples had been taken. This trace element analysis of the apatite grains was performed at Bergen Geoanalytical Facility at the University of Bergen using a 193 nm ArF excimer laser ablation system (RESOlution M-50 LR) coupled to an HR-

SC-ICP-MS (Nu Instruments Attom ES) using parameters reported in Appendix D1. The apatite grains were ablated for 30 s, after 15 s of blank measurement, using a 26 µm spot size, 5 Hz, and a fluence of ~2.5 J/cm^2 in a standards-bracketing fashion. The ablated areas were the same areas (ROI) used for counting. NIST612 (external) and Durango apatite (quality control) was used as standards. The data were acquired in FastScan Mode, measuring the masses 29Si, 43Ca, 147Sm, 232Th, and 238U.

Data reduction was done using Iolite 4 (v. 4.4.5) with the Trace Elements Next (Longerich et al. 1996) data reduction scheme. Data reduction methodology follows Paton et al. (2011) and includes a correction for gas blank, laser-induced elemental fractionation, and instrument mass bias using NIST612 as an external standard with 43Ca as the internal standard. Counts for blank measurements and instrumental bias were corrected with an automatic spline function. For quality control, the Durango apatite were measured frequently, and values are reported in Appendix D2.

In case of vertical zonation in the ^{238}U concentration through the crystal, the first incoming 'peak' of the signal was assumed to reflect the ^{238}U concentration at the surface and was used for further analysis.

3.1.4 Thermal age calculation and Thermal history modelling

Thermal ages for all samples were calculated using the online tool IsoplotR version 5.0 (Vermeesch, 2018). The program was used to calculate single grain ages and to generate a radial plot and the weighted mean for each sample. Calculations were done using the ICP (absolute) method for apatite in the program, not requiring a Zeta-value, analogue to Equation 1 (section 3.1.1).

Samples for which both count, and sufficient length data could be obtained, were modelled using the program HeFTy version 2.0.9 from 2022 (Ketcham, 2005).

HeFty requires a zeta calibration factor to calculate ages for the modelling. For each sample which was to be modelled using HeFty, a session specific zeta calibration factor and associated error was calculated using Equation 5 and 6 and the Durango age standard. The Durango age standard was measured in each LA-ICP-MS session and the areas used for the session were counted prior to the work on the sample measured in the same session.

For apatite, P_i in Equation 3-6 (section 3.1.1) may either stand for the ^{238}U-concentration (in ppm) or for the U/Ca ratio measurement (Veermesch, 2018). In this study, the ^{238}U-concentration was used. For the total decay constant of ^{238}U (λ_d) a value of 1.55125×10^{-10} (Jaffey et al., 1971) was used. The age standard used is a Durango. The precise ^{40}Ar–^{39}Ar

reference age used for the Durango standard is 31.44±0.18(2σ) Ma (McDowell et al., 2005). Track lengths implemented in the modelling were accompanied by the calibrated personal factors for track length measurements and for Dpar measurements (section 3.1.3).
The program was set to use the annealing model by Ketcham et al. (2007b), the c-axis projection by Ketcham et al. (2007a) and the Dpar value as a kinetic parameter.

Muscovite 40Ar/39Ar dates along the Nordfjord range from 398–387 Ma after Young et al. (2011) and 392-388 Ma after Walsh et al. (2013). Using the closing temperature of the muscovite 40Ar/39Ar system of approx. 425°C (Harrison et al., 2009) a tentative starting constraint can be set.

For the end constraint the present-day temperature was used. In order to estimate a present-day temperature, I used historical open-source weather data (meteorological institute) of the two closest weather stations to the south (Florø lufthavn) and north (Fiskåbygd) of the study area. Using all available data between 1980 and today, I calculated a mean annual temperature in Fiskåbygd (41 masl) between 1980 and 2017 of 7.1°C and 8.2°C at Florø lufthavn (9 masl) between 2006 and 2022. Based on this data I set the present-day temperature on 7.6°C ± 5°C to allow for variation.

By adjusting the basal heat flow in HeFTy to 45 mW/m^2, the geothermal gradient was set to 15 °C/km after Green et al. (2022).

3.2 Structural geology

3.2.1 Fieldwork

Fieldwork in the study area was carried out during two field trips between 01.-07.08.2021 and 07.-14.07.2022. To be able to cover a large area I focused on studying road cut outcrops. These offer study locations with easy accessibility. Planning prior to the field work contained literature research and studying maps, including investigation of the streets by the means of google street view. Locations where apatite fission track samples were taken served as starting points, then following the streets in between, outcrops for further study were investigated. See Figure 9 for an overview of all studied outcrops in relation to the AFT sample locations. Field notes and measurements were written down in a field book and later digitalized in Excel for further use. For all measurements an analogue, high precision Breithaupt compass was used (Figure 8).

Figure 8: Compass measurement in the field.

The workflow at each locality was the same:

1. Noting the coordinates using an iPhone SE, the date, time, and the weather. Apart from an outcrop number, each location received a name or a short and re-recognizable description and the street number or a description of how to get there.
2. A rough description of the outcrop or special characteristics.
3. A description of the lithology based also on a rock sample taken using a hammer.
4. Measurement of the foliation or the bedding (dip direction and dip).
5. Sketching fractures and the outcrop if the structural architecture is complex.
6. Measurement of fractures (dip direction and dip), focusing on fractures with mineral growth on fracture surfaces.
7. Description of the mineralization, if any, and measurement of lineation / slicken fibres (trend and plunge), if any.
8. Interpretation of kinematics based on slicken fibres.
9. Judging quality of lineation (1 vague – 3 clear) and certainty of kinematics interpretation (1 uncertain – 3 certain)
10. Description of the age relationship of the mineralizations if there are several generations.
11. Taking pictures.

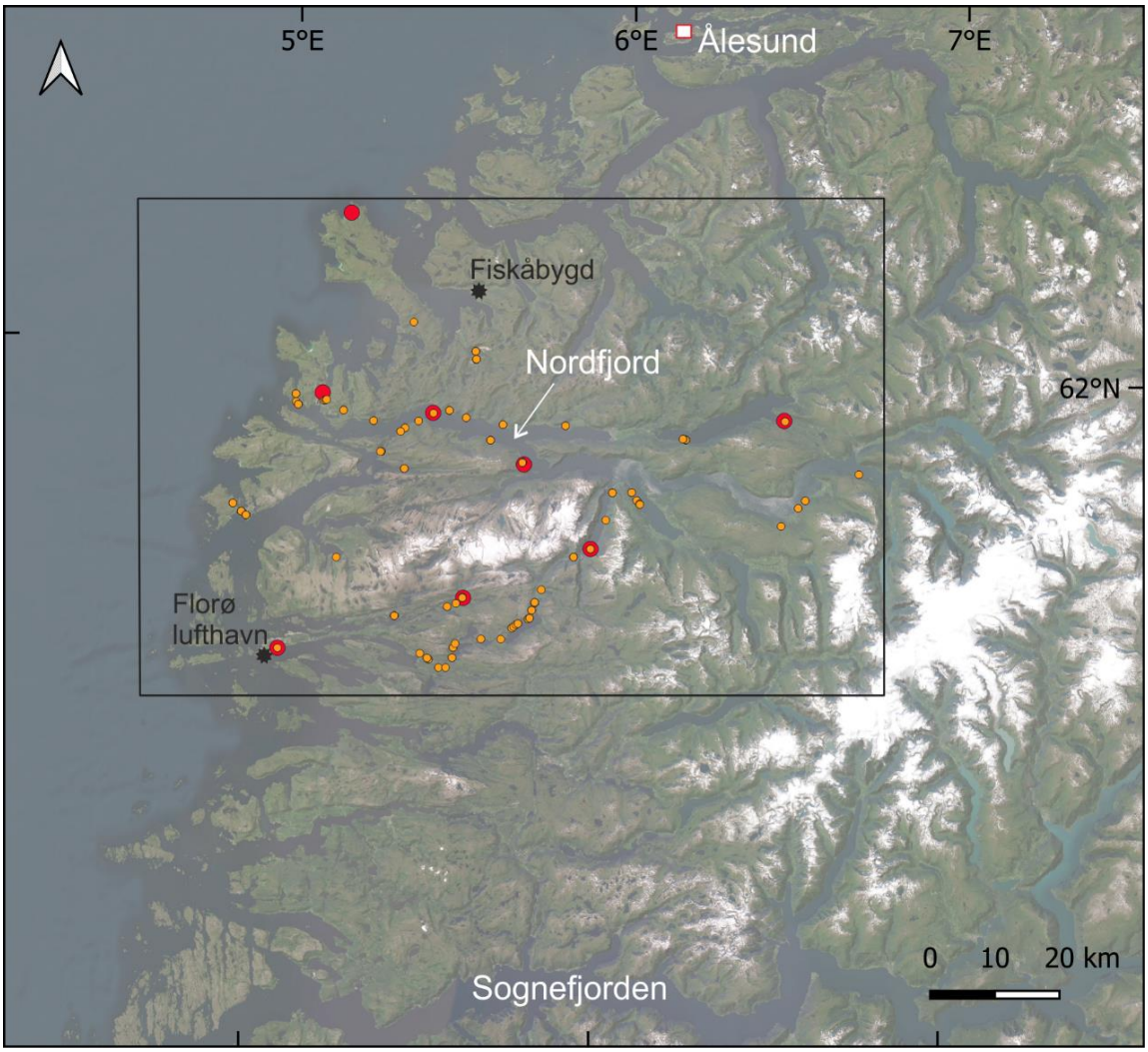

Figure 9: Overview showing the study area marked with a rectangle. Apatite fission track sample locations are marked in red, and outcrops studied in the field are marked in orange. Weather stations used for the end-constraint in thermal modelling marked by black stars.

I focused on fractures with mineral growth to acquire information about movement direction i.e., the kinematics and thus the type of fault (normal/reverse, sinistral/dextral). This approach is based on the assumption that lineation on a fault surface (slickenside) represents the displacement direction of the latest movement along the fault (Fossen 2010b). The type of lineation that I encountered mostly during field work was minerals crystalized as fibres (slicken fibres). If there is movement along the fault and mineral condensation from a circulating fluid, minerals will preferentially grow in the movement direction on the lee side of irregularities (Figure 10a; Fossen, 2010b). These slicken fibres can tear off with edges pointing towards the slip direction of the missing surface i.e., the moved block. The tear-off-edges can be big and visually observable (Figure 10b and c), or so minor that they can barely

be felt as roughness by sliding the fingers along the mineralization; the surface will feel rougher against movement direction and smoother along the movement direction.

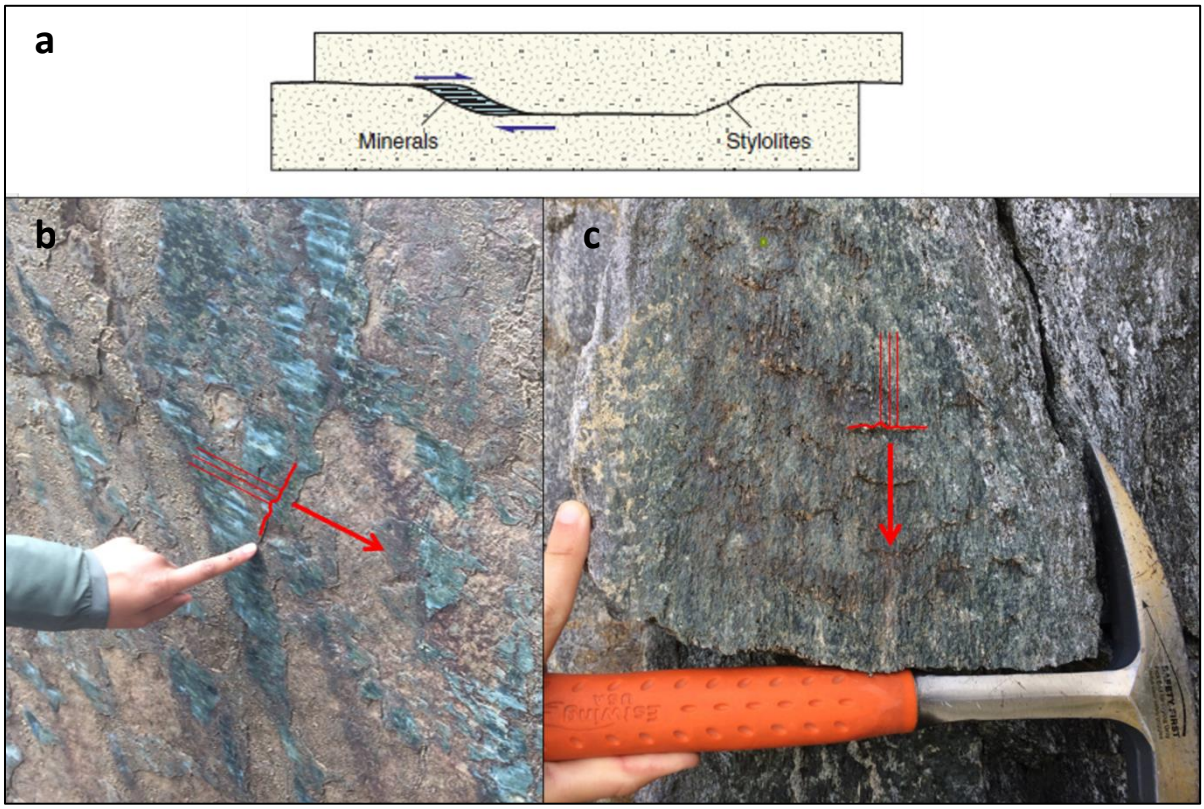

Figure 10: Slicken fibres. a: Irregularities along a fault surface creating steps where slicken fibres (mineral growth) or stylolites, respective of the step orientation and movement direction, can form (from Fossen, 2010b). b, c: examples of slicken fibres and torn off edges observed during my field work. Lineation of the slicken fibres and interpreted slip direction of the missing fault block are indicated in red.

3.2.2 Data processing

The analogue field data were digitalized from the field book to Excel. Maps displaying fracture and foliation orientations and kinematics were produced using QGIS 3.16.5. All structural data was furthermore stereographically plotted using Stereonet 11.

The kinematics were subdivided into strike-slip (dextral, sinistral) and dip-slip (reverse, normal) ignoring oblique-slip for simplification. Strike-slip was defined by a slicken fibre pitch of 0-44° and dip-slip was defined by a pitch of 45-90°.

4 Results

4.1 Apatite fission track analysis

8 apatite samples were analysed by the new LAFT method. The results are presented in Table 1 and in Figures 11 and 12.

4.1.1 Sample quality

All samples showed zonation in apatite grains during the uranium measurement. Many samples showed very low uranium concentrations, for several single grains below the detection limit. Low uranium concentrations lead to fewer fission tracks and therefore fewer confined tracks. Due to this, only in three samples a sufficient number of measurable track lengths could be found to obtain a reliable distribution. In samples with enough measurable fission tracks only TINTs were measured, in samples with only few, also TINCLEs were measured, knowing that these are less reliable, as the etching response may vary.

Samples south of Hornelen basin

VAH_23 was a good sample and without a persistent error with the microscope it would most likely have been possible to count enough track length for a reliable track length distribution. Less than half of the grains were zoned or weakly zoned. VAH_26 showed zonation both during counting and during the LA-ICP_MS measurement, where most grains were identified as zoned. Some grains were difficult to count as the fission tracks were dense due to high uranium concentrations. In addition, many grains showed dislocations, making counting challenging as these cannot always be differentiated clearly from fission tracks. Only few measurable track lengths could be found. Only less than half of the grains counted for sample VAH_31 were zoned or weakly zoned. Due to a low uranium concentration the sample was easy to count but only very few measurable track lengths could be found, as confined tracks are more likely to become visible if the number of surficial track openings is high (see section 3.1.1)

Samples north of Hornelen basin

In VAH_42 most grains were zoned or weakly zoned. It was a good sample, and it was possible to measure 100 tracks. MLM_134 contained few zoned grains, but some grains showed dislocations. It was challenging to pick grains to count since many grains had uranium concentrations below the detection limit. However, many grains also had high uranium concentrations, enabling measurement of more than 100 track lengths. VAH_48 was a good sample to count, but only few measurable track lengths were found. Most of the counted grains were zoned. VAH_78 was a good sample to count, but no measurable track lengths could be found in the sample within a reasonable amount of time. A bit more than a third of the analysed grains were zoned or weakly zoned. VAH_44-2 was of good quality and a bit more than 100 track lengths could be measured. A bit more than a third of the analysed grains were zoned or weakly zoned.

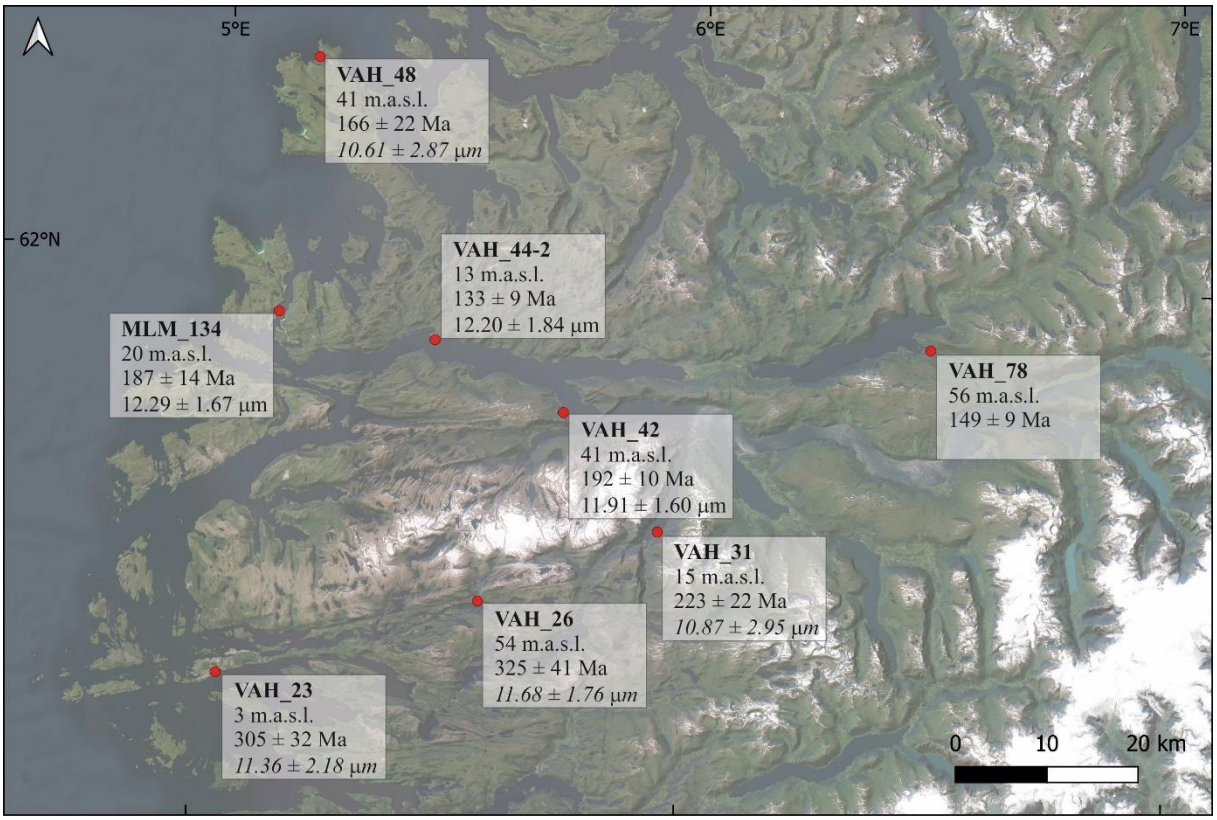

Figure 11: Overview of the AFT samples including elevations, ages (central age) and mean track lengths.

*Table 1: Results from the AFT analysis. EL – elevation. Quality (Sample quality): z – Uranium concentration zoned, d – dislocations found in the sample. n(G) – number of grains counted. Ns – number of spontaneous fission tracks counted. ^{238}U – Uranium concentration measured by LA-ICP-MS. SD – Standard deviation. $P(x^2)$ – the p-value of a chi-square probability for homogeneity. Disp. – Dispersion. MTL – mean track length. n(L) – number of fission track lengths measured. *If possible 100 or more lengths were measured, in the case of VAH_23 more track lengths could have been measured, but due to a microscope failure this was not possible. **For all samples the Dpar is based on measurements carried out during track length measurements (5 Dpars per track length) except for VAH_78 where no measurable track length could be found. Here the Dpar is obtained from measurements carried out during counting.*

Sample	EL [m.a.s.l.]	Lithology	Quality	n(G)	Ns	Mean track density [10^5/cm^2]	Mean ^{238}U [ppm] ± SD	Central age [Ma]±1σ	$p(x^2)$	Disp.	Durango central age Ma ±1σ	MTL ±SD [µm]	n(L)	Type	Dpar [µm]±SD
VAH_23	3	Augen gneiss	z,d	22	1401	18.9518	14.6±13.0	305±32	.00	47%	29.7±0.9	*11.36±2.18**	28	T	1.19±0.12
VAH_26	54	Gneiss	z,d	16	1344	23.6284	16.7±17.1	325±41	.00	48%	25.19±1	*11.68±1.76*	36	T, C	1.18±0.09
VAH_31	15	Gneiss with augen	z,d	21	604	5.5413	4.8±2.1	223±22	.00	39%	25.19±0.9	*10.87±2.95*	11	T, C	1.02±0.06
VAH_42	41	Augen gneiss	z	21	1687	29.3980	30.4±22.7	192±10	.00	21%	28.3±0.8	11.91±1.6	100	T	1.39±0.08
MLM_134	20	Mangerite	z,d	18	650	10.3605	11.6±12.8	187±14	.00	22%	29.2±1	12.29±1.67	120	T	1.37±0.11
VAH_48	41	Augen gneiss	z,d	19	827	8.6944	13.2±12.1	166±22	.00	54%	28±0.9	*10.61±2.87*	15	T, C	1.07±0.06
VAH_78	56	Gneiss	z	21	913	7.9441	10.6±7.5	149±9	.00	20%	30.4±0.8				0.98±0.10**
VAH_44-2	13	Granitic gneiss	z	21	1375	11.6910	17.3±11.7	133±9	.00	26%	29.2±1	12.2±1.84	103	T	1.56±0.14

4.1.2 Thermal ages and track lengths

Single grains with uranium concentrations below 0.5 ppm showed naturally large errors and unrealistic ages and were therefore systematically excluded from the analysis and the age calculation. Grains used for the age calculation can be seen in Appendix B. For each sample, a radial plot and a weighted mean plot were made to control single grain age distributions and relationship to the weighted mean and central age. The plots can be seen in Appendix B for each sample. The central age was used as the thermal age for the sample, termed only 'age' in the following.

The ages of the 8 samples range from 133 ± 9 to 325 ± 41 Ma (Middle Carboniferous to Early Cretaceous) at present-day elevations of 3 masl to 56 masl (Table 1, Figure 11). Most ages are Late Triassic to Late Jurassic.

The mean track lengths of the 7 samples with measurable track lengths range from 10.61 ± 2.87 to 12.29 ± 1.67 µm. The 3 samples with more than 100 measurable track lengths range from 11.91 ± 1.60 to 12.29 ± 1.67 µm. The track length distribution for those samples is shown in Figure 12. All samples with fewer measurable track lengths show a shorter MTL, below this range. These MTLs will not be used in the thermal history modelling and in the further interpretation, as they are seen as not reliable since it is possible that not the whole spectrum of the distribution is sampled. In addition, the MTL may be skewed as both TINTs and TINCLEs were measured. The coastal sample MLM_134 showed the longest MTL and a dominant long track length population in the distribution (Figure 12). The MTLs of all samples agree within error margins, especially the 3 samples with reliable MTL are very close together. In general, the MTL are rather short, suggesting comparably slow exhumation through the PAZ.

Ages seem to be in general older towards the south of the study area and towards the coast (Figure 11, Figure 13). The biggest jump in age is to samples VAH_26 and 23 in the south, with up to 100 Ma difference. The youngest age (VAH_44-2) is located centrally at the Nordfjord. It has the second lowest elevation (9 masl), however, the coastal sample at the lowest elevation (3 masl) shows one of the oldest ages (VAH_23). The sample at the highest elevation (56 masl) on the other hand, shows the second youngest age (VAH_78). For AFT ages, the general build-up should be older ages at high elevations and younger ages at lower elevation. This is based on the assumption that the topography is generated by non-tectonic processes such as fluvial or glacial erosion. Here, samples at higher elevation will be above the other samples in the crust and closer to the surface, therefore they will pass through the

PAZ earlier, resulting in older ages. As this relationship is not given, tectonic activity in the region can be assumed. This will be discussed further in section 5.2.2.

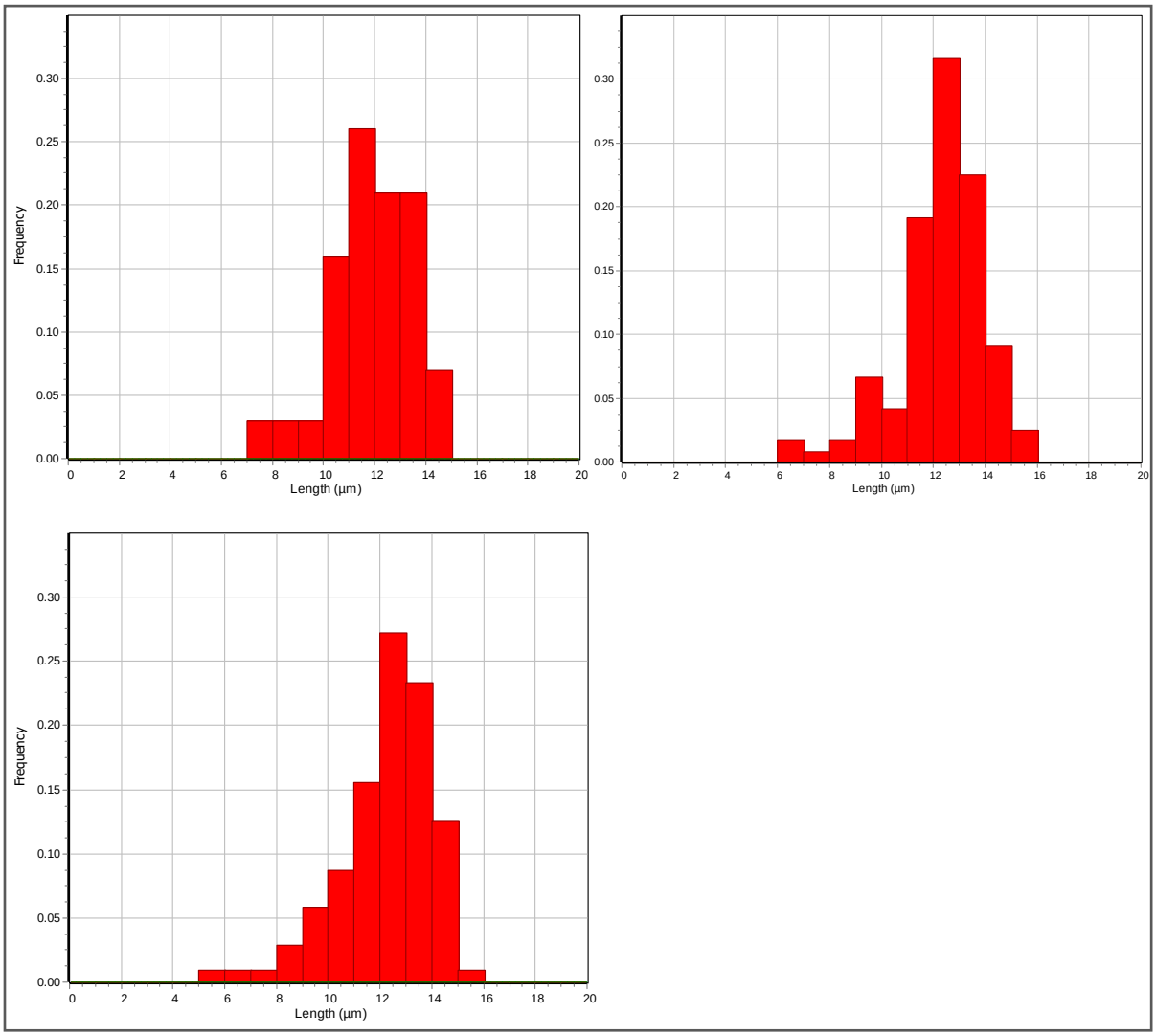

Figure 12: Track length distribution of VAH_42 (top left), MLM_134 (top right) and VAH_44-2 (bottom). Extracted from HefTy.

4.1.3 Factors influencing age and track lengths

The mean Dpars of the 8 samples have a rather narrow range from 0.98 to 1.56 µm. The 3 samples, in which more track lengths were measured and thus also more Dpars, range from 1.37 to 1.56 µm. The narrow range indicates homogeneous compositions. The Dpar-MTL plot (Figure 13) shows a strong correlation, with the sample with fewer measurements showing both shorter track lengths and Dpars. This could point to the correlation between Dpar and annealing kinetics or indicate that fewer measurements have in general lead to an underestimation of the length. The ages show no correlation with the uranium concentration and an insignificant correlation with the measured Dpar (Figure 13). This indicates that there is no correlation between the measured age and the chemical composition of the analysed

sample. The age-elevation plot shows an insignificant correlation. As mentioned before, samples at similar elevation partly show strong age offsets. A very weak correlation with ages decreasing towards the east and a strong correlation of ages decreasing towards the north can be shown (Figure 13).

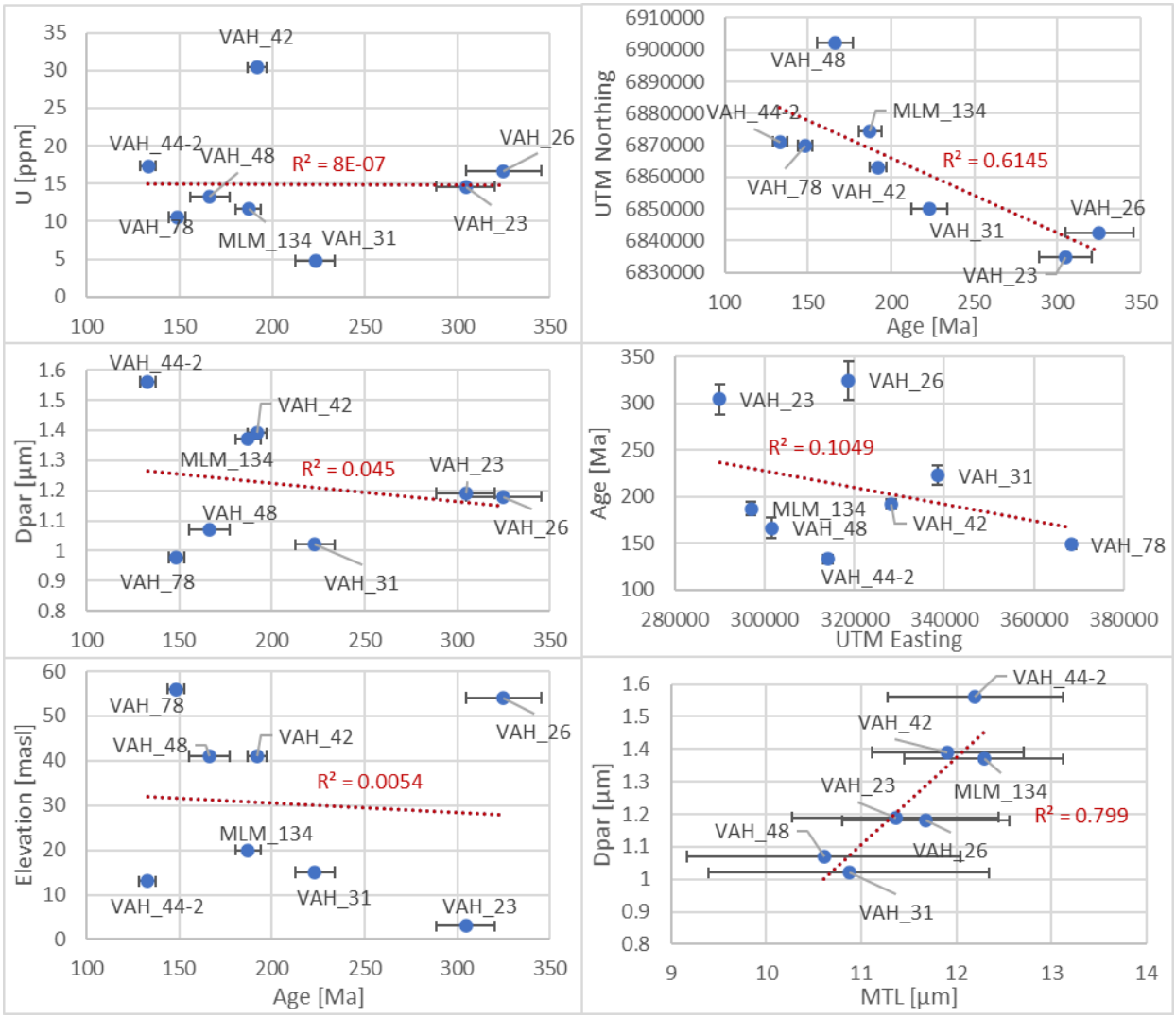

Figure 13: Left from top to bottom: Age-Uranium concentration plot, Age-Dpar plot and Age-elevation plot. Right from top to bottom: Age-UTM Northing plot, UTM Easting-age plot and MTL-Dpar plot. 1σ error for the ages and standard deviation for MTLs indicated. Trend and corresponding R^2 value indicating correlation shown in red. R^2=0 no correlation, R^2=1 full correlation.

In Table 2, the Durango standard measured together with each sample can be seen for quality control. For comparison, the reference age for the Durango standard is 31.44±0.18 Ma (McDowell et al., 2005). Comparing the age calculated by the absolute approach (Equation 1 in section 3.1.1) and the zeta calibrated age (Equation 3), it can be seen that the zeta calibrated age is older and shows a larger error. Both ages overlap within error margins, however. The zeta calibration factor ($\zeta_{ICP,}$ Equation 5) was calculated for ages used in thermal modelling as HeFTy requires it as input.

Table 2: Comparison of the Durango age, the age calculated by the absolute approach (central age), the zeta calibration factor (ζ_{ICP}) and the zeta calibrated age. Dur - Durango standard. See equations 1-6 in section 3.1.1.

Sample	Dur central age [Ma] ±1σ	Dur $P(x^2)$	Dur Dispersion	ζ_{ICP}[yr cm^2] ± $\sigma_{\zeta ICP}$	Absolute sample age ± 1σ	Zeta calibrated age
VAH-23	29.68 ± 1.70	0.360			305±32	
VAH-26	25.19 ± 2.01	0.014	0.112 ± 0.085		325±41	
VAH-31	25.19 ± 1.80	0.110			223±22	
VAH-42	28.31 ± 1.63	0.980		2151.6 ± 62.42	192±10	203 ± 17
VAH-44_2	29.19 ± 1.96	0.200		2097.1 ± 64.71	133±9	139 ± 12
VAH-48	29.98 ± 1.17	0.180			166±22	
MLM-134	29.18 ± 1.91	0.450		2096.8 ± 69.87	187±14	185 ± 20
VAH-78	30.42 ± 1.66	0.600			149±9	

4.2 Thermal history modelling

Only for three samples a sufficient number of track lengths could be measured to obtain a reliable track length distribution and to use for meaningful thermal modelling.

These samples were inversely modelled using the Monte Carlo search method trying one million paths. The models show acceptable paths, good paths, and a weighted mean path. For modelling parameters and start-and end-constraints see section 3.1.4. For model input, the zeta corrected age was used.
The samples could not be modelled together. VAH_42 and MLM_134 could be modelled together but only acceptable paths were found by the program.

For sample VAH_42 at 41 masl present-day elevation furthest east, both the weighted mean path and the good path distribution indicate fairly fast cooling through the PAZ until around 220 Ma (Figure 14). Based on the weighted mean path cooling through the PAZ would be ~2 °C/Ma. After that the model suggests a slow exhumation (~0.2 °C /Ma), with faster exhumation during the last 30 Ma years until present. However, this last 30 Ma period of fast exhumation cannot be recorded by the apatite fission track system as it is only sensitive to temperatures between around 120 and 60 grad C (PAZ). If there is no reburial, the sample will not record the younger history.
Sample VAH_44-2 at a present elevation of 13 masl is the youngest sample. The weighted mean path indicates gradual cooling (~0.9 °C /Ma) through the PAZ, while the distribution of good paths rather indicates a steep cooling through the PAZ, similar to VAH_42, until around 150 Ma (Figure 15). The weighted mean path is based on all paths, including the acceptable paths. Based on the distribution of good paths, a period of faster cooling of ~1.54 °C /Ma can be estimated, followed by a period of slower cooling (~0.4 °C /Ma).

Sample MLM_134 was located at an elevation of 20 masl furthest to the west. Similar to VAH_44-2, it also showed a weighted mean path differing from the distribution of good paths (Figure 16). While the weighted mean path indicated gradual cooling (~0.69 °C /Ma) through the PAZ until present-day, the good paths distribution suggests faster cooling through the PAZ, analogue to VAH_42, until around 200 Ma, followed by slow cooling until present-day. Based on the distribution of good paths, the period of faster cooling can be estimated with ~2.03 °C /Ma, and the period of slower cooling with ~0.25 °C /Ma.

In difference to VAH_44-2, the weighted mean path in the model for MLM_134 is not in agreement with the distribution of good paths. Therefore, for both MLM_134 and VAH_44-2 the weighted mean path is seen as not as reliable. However, both the weighted mean path in both models in in agreement with steeper cooling until around 250 Ma (Permian-Triassic boundary), which in turn is in agreement with the model for VAH_42. After that, the weighted mean and the distribution of good paths for both samples disagree on whether the steep cooling continues through the PAZ or is followed by a shallower cooling path.

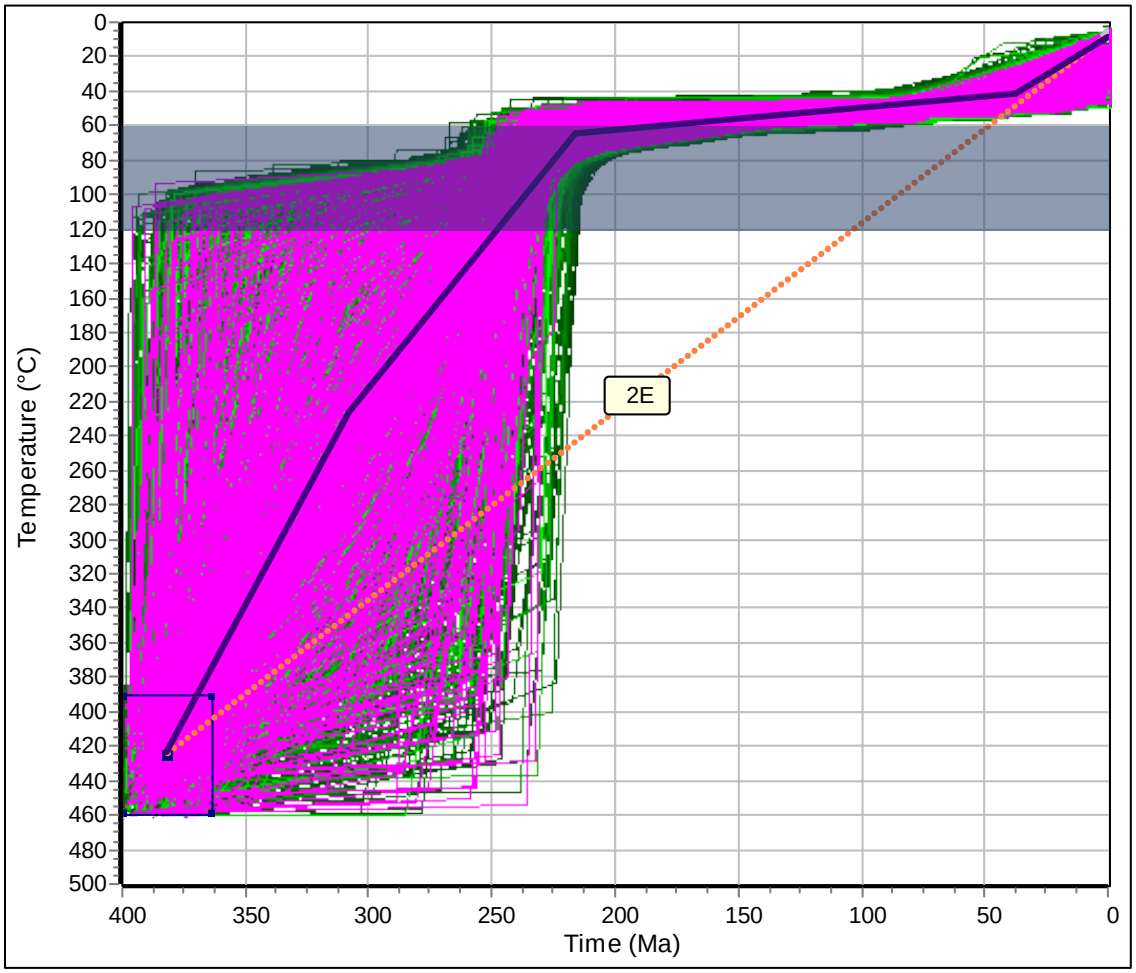

Figure 6: Thermal history model of sample VAH_42. For start- (blue box) and end- constraints see section 3.1.4. Green paths – acceptable, pink paths – good. Blue thick path is the weighted mean path. Extracted from HeTTy. The PAZ is indicated in grey.

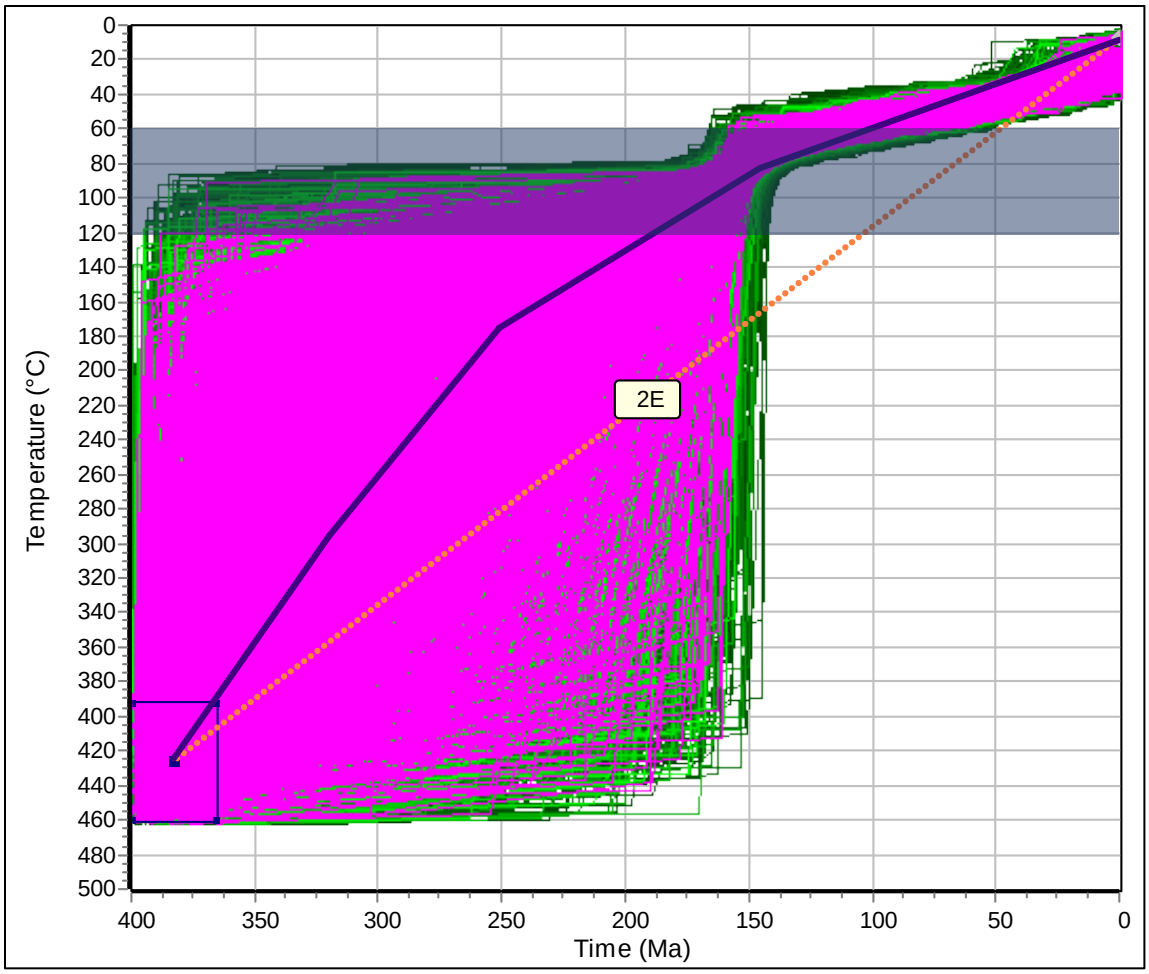

Figure 15: Thermal history model of sample VAH_44-2. For start- (blue box) and end- constraints see section 3.1.4. Green paths – acceptable, pink paths – good. Blue thick path is the weighted mean path. Extracted from HeTTy. The PAZ is indicated in grey.

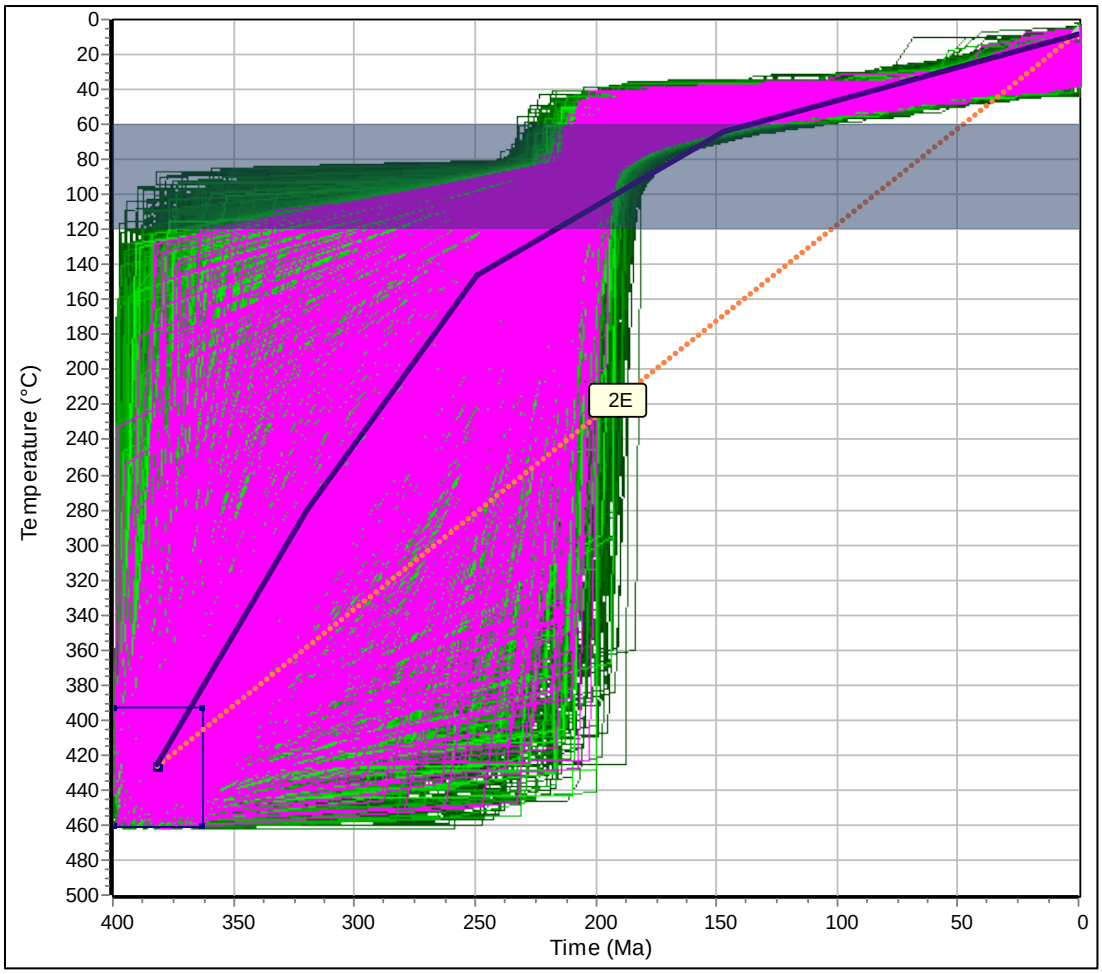

Figure 7: Thermal history model of sample MLM_134. For start- (blue box) and end- constraints see section 3.1.4. Green paths – acceptable, pink paths – good. Blue thick path is the weighted mean path. Extracted from HeTTy. The PAZ is indicated in grey.

4.3 Field work

4.3.1 Geology of the study area: Lithologies, foliation and ductile kinematics

The only sedimentary rocks found in the study area are located in the Hornelen basin, the bedding of the sandstone was measured to be shallowly dipping to the NW (041/15, see Appendix E). All other outcrops studied during field work are part of the WGR or the Lower, Middle or Upper Allochthon (compare Figure 3 and Figure 9). The northern part of the study area including most of the Nordfjord until Nordfjordeid belongs to the WGR, while the areas studied south and east of the Hornelen basin consist of the Middle Allochthon. The outcrops studied on Bremangerlandet are in rocks from the Upper Allochthon.

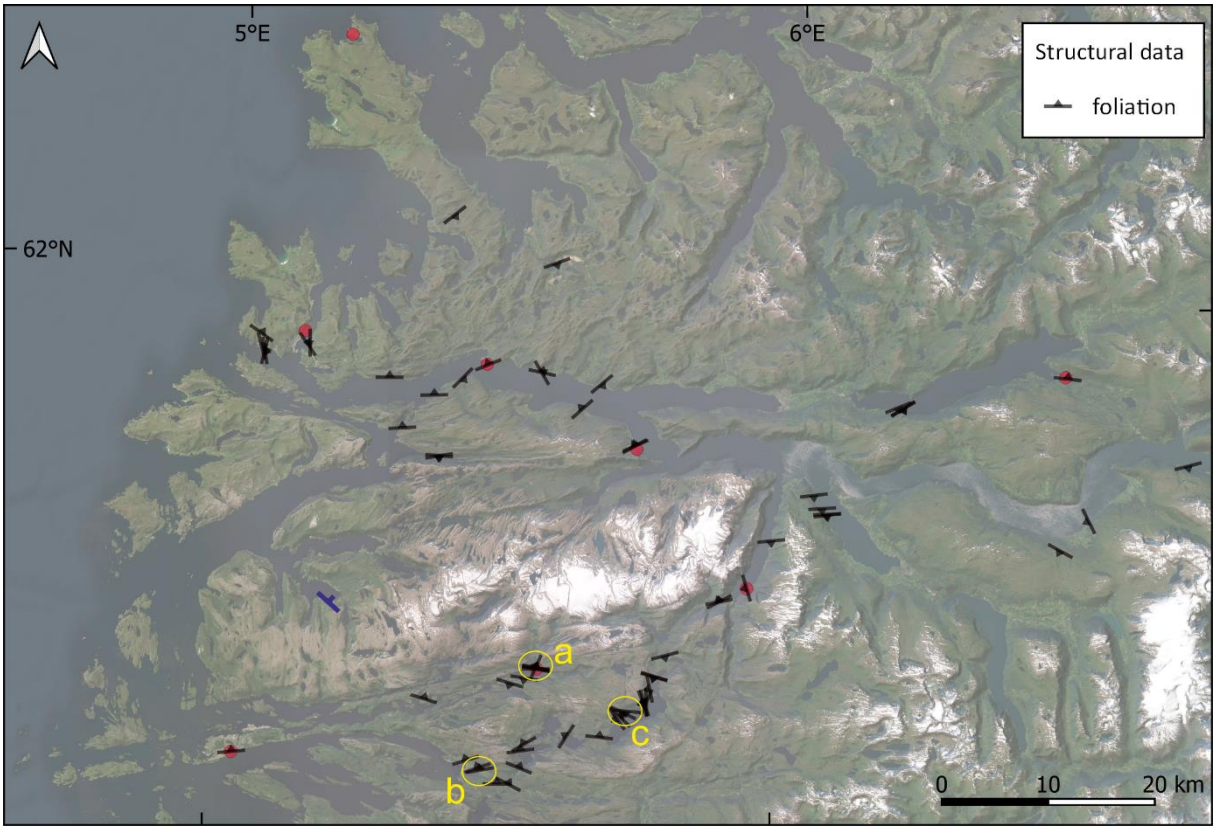

Figure 17: Overview of the measured foliation showing strike and dip. The blue measurement is the bedding of the sedimentary Hornelen basin. AFT sample locations are marked in red. a, b and c mark locations where ductile kinematics were observed.

Most rock types encountered were metamorphic, mostly gneisses. Occasionally mylonitic gneiss or mylonite was found, indicating the presence of Caledonian and Post-Caledonian ductile shear zones. Mylonite was found at several locations inside the southernmost Middle Allochthon province and along the Haukå fault and the Bortnern fault, where it intersects Hornindalsvatnet in the NE of the study area.

Two AFT samples in the south of the study area are located in WGR basement windows. Sample VAH-31 is located in a window formed in the center of an anticline, here migmatitic

and mylonitic textures have been observed in the augengneiss. Sample VAH_23 is located at the Florø horst, also here granitic augengneiss has been observed.
In the Middle Allochthon, metasediments such as quartzite and paragneiss have been observed, especially along the Haukå fault and north of the anticline basement window (northern part of subregion 7) but also granitic gneisses, mafic gneisses and other less well-defined gneisses. Close by the Haukå fault, a strongly altered, slightly foliated anorthosite has been observed. Both lighter (e.g., granitic) and more mafic gneisses were encountered in the WGR.
The gneisses of the Middle Allochthon located north of the anticline basement window are partly strongly deformed and folded. Also along the Haukå fault south of the Hornelen basin, the paragneiss was strongly deformed and folded. At two locations along the road 616 at the southern bank of the Nordfjord, the gneiss of the WGR had been eclogitized to varying degrees, in parts occurring as garnet-bearing gneiss. Here, the gneisses were also observed to be strongly folded. In the WGR, at the mainland side of the Måløy bridge, garnet-bearing, unfoliated granulite has been observed. Further to the north, on Stadlandet close to Selje beach, another occurrence of eclogite was observed. On the northern bank of the Nordfjord at the quarries at road 15 between Tennebø and the crossing with road 618 towards Åheim, the gneiss was also observed to be strongly folded.
Magmatic rocks were encountered on Bremangerlandet (granodiorite) and close to Åheim (peridotite; compare Figure 3: Ultramafic body). The peridotite was here observed at two locations, being more fine-grained and foliated at one of the locations. The non-foliated peridotite was also observed southwards at one locality at the northern bank of the Nordfjord. For an extensive list of all lithologies observed and locations of the lithologies see the field data in Appendix E.

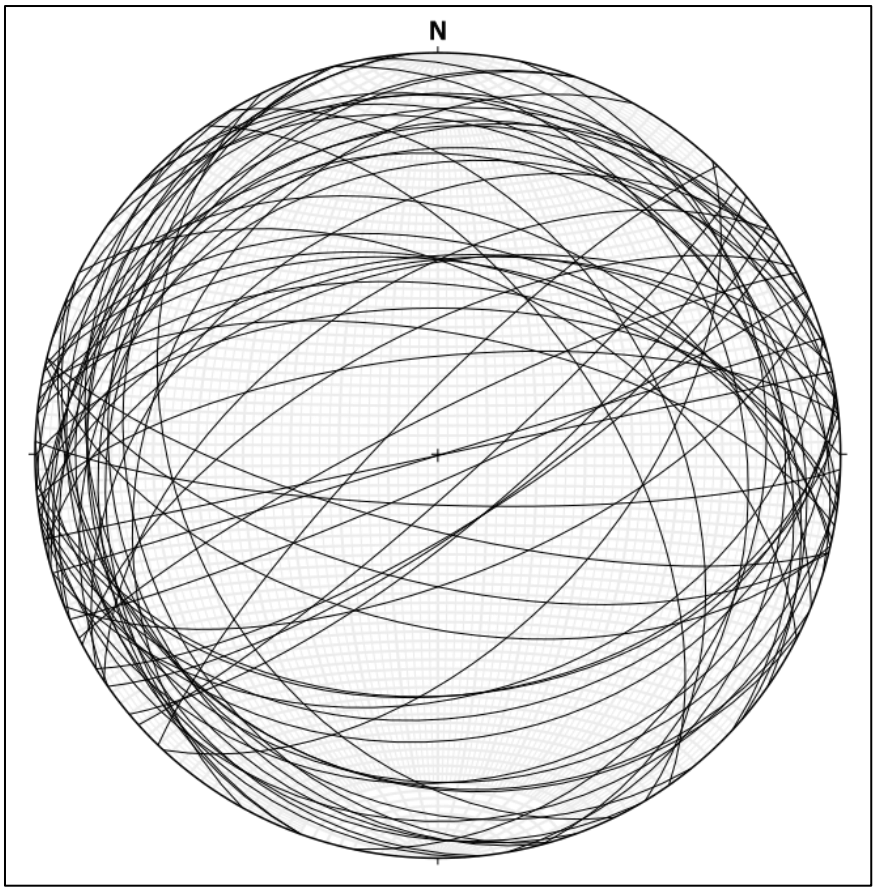

Figure 18: Stereoplot of all foliation measurements

Even though the focus was not on the ductile elements, an extensive database of foliation measurements has been obtained (Figure 18). The foliation is mostly shallowly dipping towards E or W but some steeper foliation dipping N or S can also be observed. At some locations, folding has been observed as described above. A clear overall trend for the whole region cannot be identified. Local trends will be described for defined subregions in section 4.3.4.

At three locations ductile kinematics have been identified. Sigmoidal clasts and pressure shadows show top to the W/NW movement in the mylonitic gneiss along the Haukå fault at the transition from the Middle allochthon to the Hornelen basin, with a foliation dip towards W and N (a in Figure 19). Also at a locality b, top to the W kinematics were observed, with a foliation dip towards NNW. At a locality c, with a foliation dip towards SSW, mostly top to the SE kinematics but also opposite, top to the NW kinematics, have been observed. While locality a and b can be correlated to the ductile Devonian extension, c most likely developed during the Caledonian orogeny and was partly overprinted by Caledonian collapse and Devonian extension.

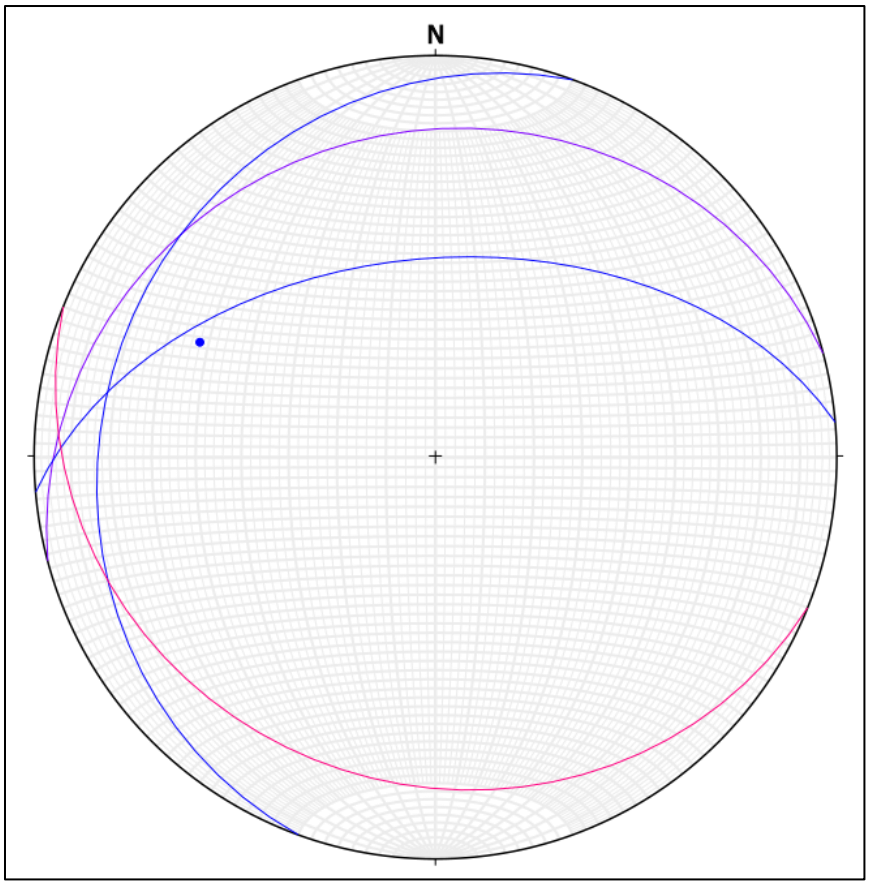

Figure 19: a (blue): ductile kinematics top to the W/NW on foliation planes 290/18 and 355/49, the latter with measured ductile kinematics 296/35. b (purple): top to the W, foliation plane 345/20. c (pink): mostly top to the SE but also opposite, foliation plane 203/20

4.3.2 Mineralizations on fracture planes

The most observed minerals were chlorite and epidote, often in paragenesis, but on many occasions also alone. They often occurred together with zeolite (mostly white variety). In the southern Middle Allochthon, iron and pyrite were also found to be covering fracture surfaces, however, did not show lineation. On the northern bank of the Nordfjord close to Måløy, as well as on the southern bank of the Nordfjord in the WGR, muscovite has been observed at few locations. It was only possible to measure lineation formed by muscovite at one location, as muscovite crystallizes flaky. Also, quartz and calcite only occurred at few locations.
At the peridotite locations described above, an abundance of minerals occurred, which allowed for an extensive identification of slicken fibres and kinematics. As can be seen in Figure almost all fractures measures should identifiable kinematics. Minerals observed here were chlorite, serpentine, talc, soapstone, epidote, zeolite, calcite and olivine (rare). At a nearby gneiss locality, serpentine was also observed, suggesting a fluid circulation system connecting the gneiss locality and the peridotite location, as it can be assumed that the

serpentine was dissolved from the peridotite.
The granodiorite on Bremangerlandet showed joints at the western most locality and fractures with kinematics towards the east. Both joints and fractures contained mainly epidote, at the eastern locations also together with zeolite and possibly quartz.

It was observed that in general, mineralization was more abundant in the WGR than in the Allochthons, where many fractures did not contain mineralizations, making identification of kinematics easier in the WGR. This relationship may be due to less minerals being dissolved in fluids circulating in certain areas and therefore less mineral crystallization, or in general less kinematics/fault movements. Both in the WGR and in the Middle Allochthon, chlorite was mainly observed, often occurring together with epidote and zeolite. At certain locations, epidote occurred alone or together with zeolite. In general, a relationship between the lithology at the location and the mineral type has been observed. Fractures in mafic lithologies i.e., mafic gneisses showed abundant mineralization and well developed slicken fibres, mostly chlorite, sometimes with epidote and zeolite. In granitic gneisses or granitic lithologies, traces of epidote were found on fracture planes, but those rarely formed well measurable lineation and tear-off-edges (see 3.2.1). Here, zeolite sometimes occurred with epidote, forming measurable slicken fibres. This relationship may be due to fluids dissolving mainly chlorite from mafic host rocks and epidote from granitic host rocks and in most conditions, minerals do not remain dissolved in the fluid over a long period of time and therefore get deposited close to where they were dissolved. However, this relationship is most likely more complex, as fluids can carry dissolved minerals between connecting fault systems. In addition, at many locations no mineralization has been found in lithologies similar to those where mineralizations have been found previously.

Around the Hauká fault (subregion 5) in the Middle Allochthon, where mainly paragneiss and the altered anorthosite have been encountered, most fractures did not have mineralization. Only few fractures with measurable slicken sides were observed, these mainly contained zeolite and epidote.

4.3.3 Fractures and brittle kinematics

A stereoplot of all measured fractures across the study area, both with and without slicken fibres, shows a preferred NNW-SSE striking trend, a lesser preferred E-W striking trend and a minor, vague NE-SW striking trend (Figure 20).

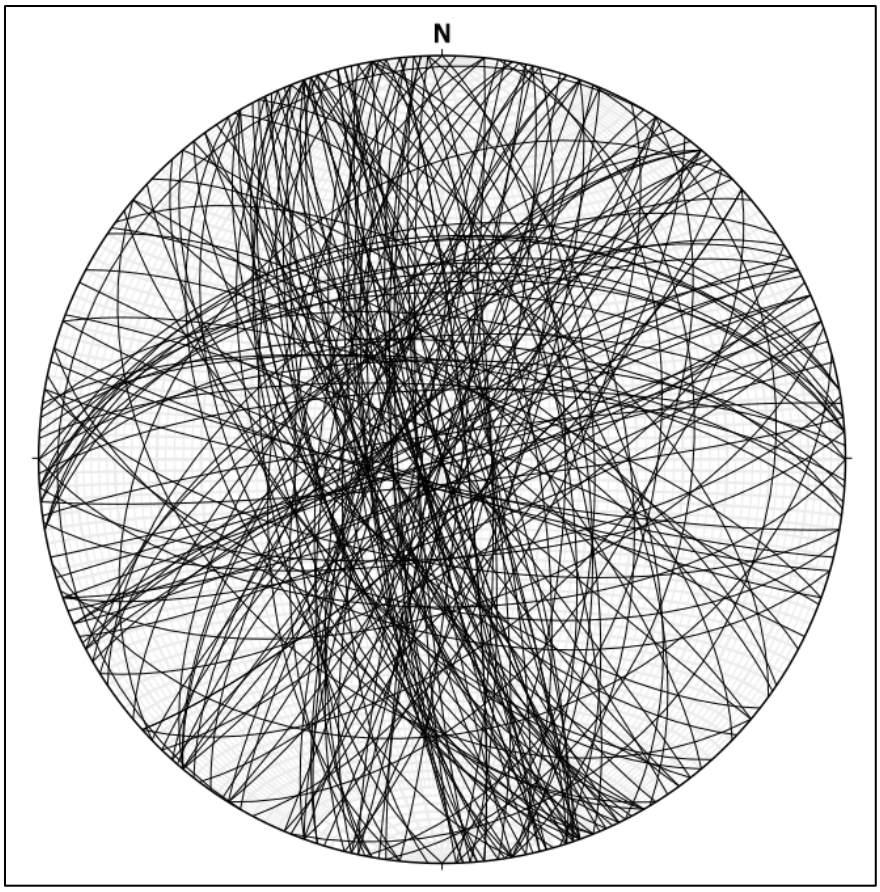

Figure 20: Stereoplot of all measured fractures.

On a map of all measured fractures, showing also kinematics, it can be observed that most kinematics were interpreted as sinistral. However, both illustrations appear convoluted due to the high number of measurements, therefore a division in subregions has been carried out. The data points (outcrops) included in each subregion can be seen in Appendix E. Subdivision was done based on similar trends/characteristics of the measurements, spatial proximity on the map and knowledge about the structural domains of the study area, as described in the Geological background chapter. The subregions are indicated on Figure 21 and 22. For Figure 22, only defined kinematics with an assigned certainty of 2 or 3 (most certain) were used, excluding the most uncertain (1) interpretations of kinematics, in order to make it more concise and manageable. Here, it can be seen that fractures in the east of the Nordfjord are parallel to the foliation while this happens rarely at other locations. In addition, the quarry location in subregion 1 still appears to be cluttered. Due to the abundancy in slicken fibres at the location as mentioned previously, many certain interpretations of the kinematics could be made.

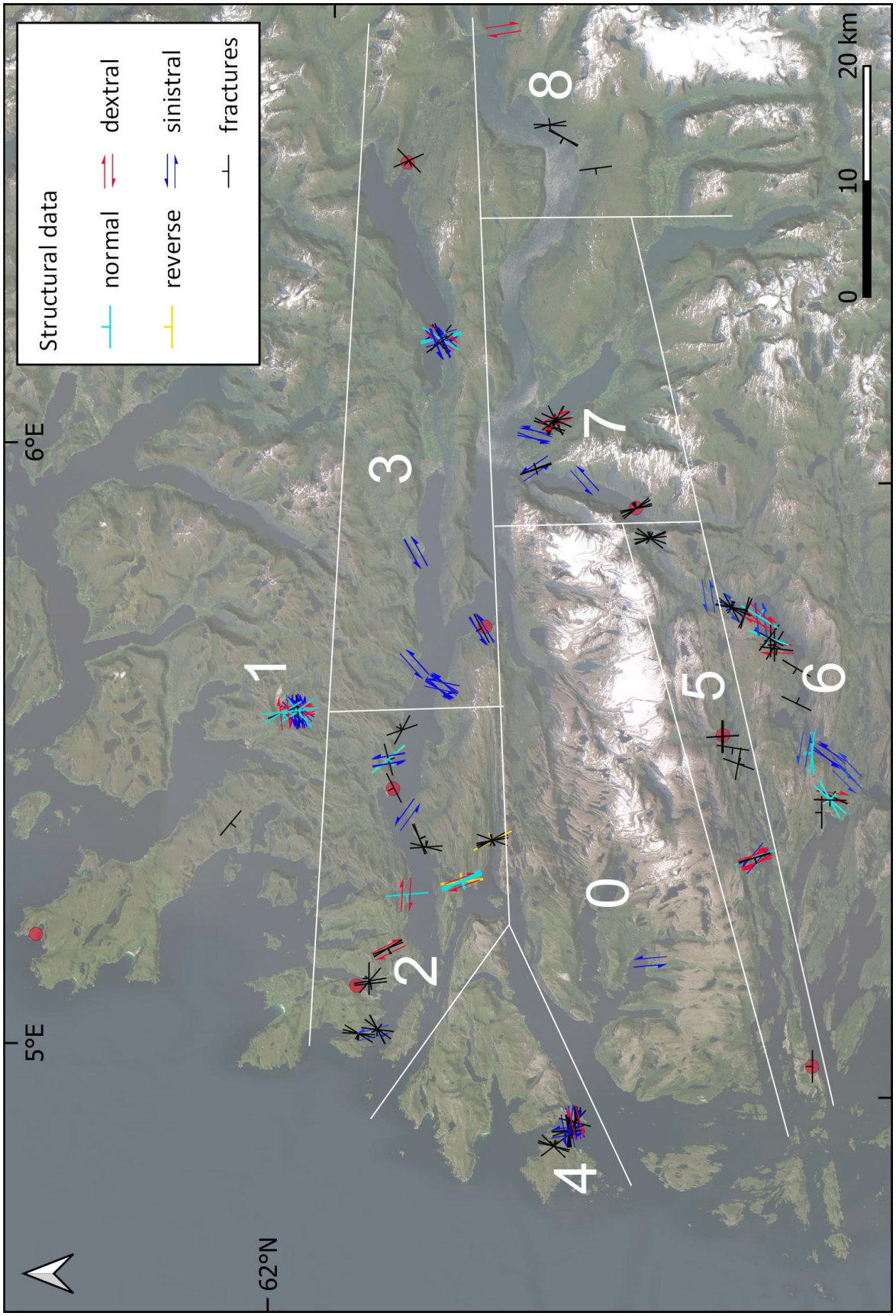

Figure 21: Overview of all measured fractures showing strike, dip and kinematic. Fractures without kinematic indicators are black. AFT sample locations are indicated in red. The defined subregions are marked in white. Data points (outcrops) included in each subregion can be seen in Appendix E.

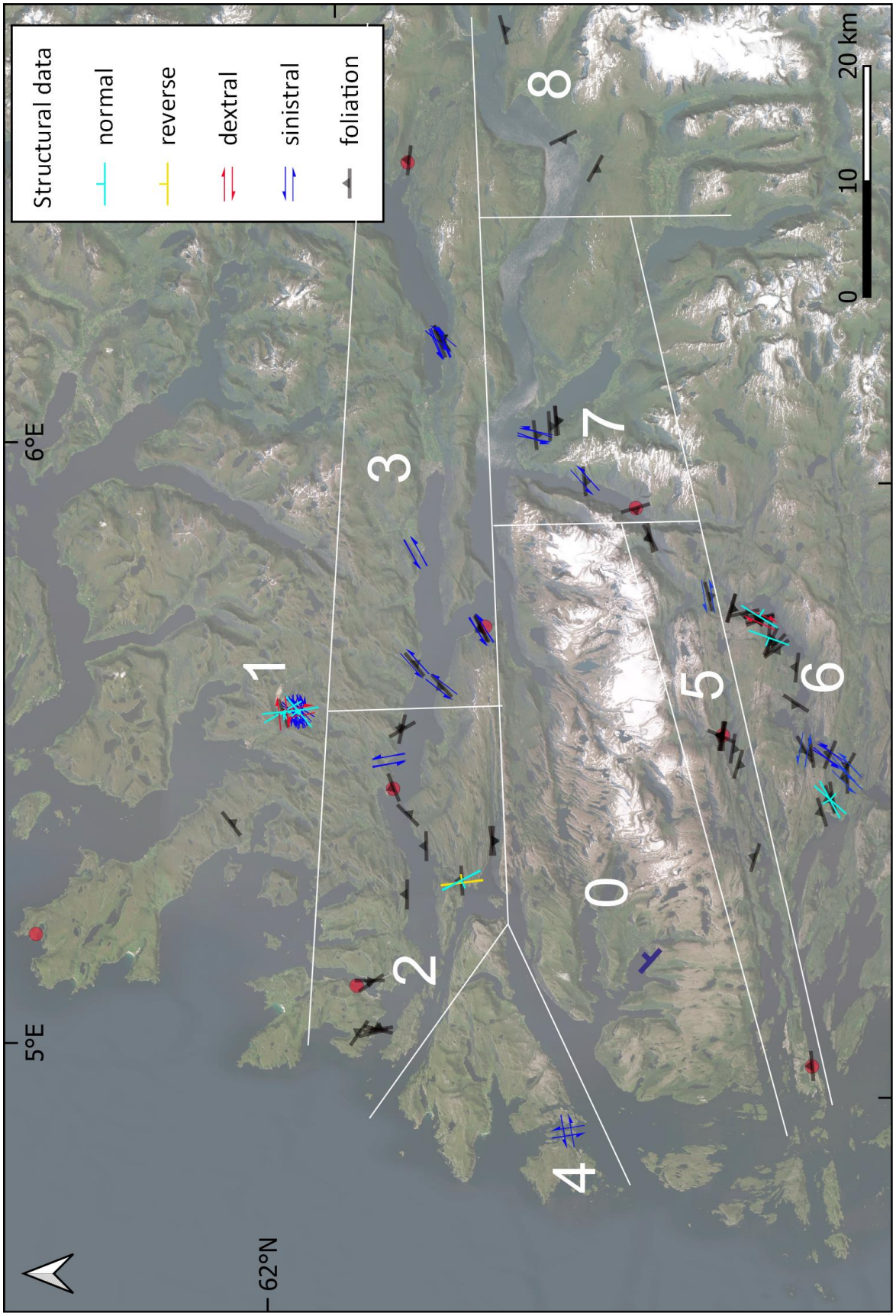

Figure 22: Overview of measured fractures showing strike, dip and kinematic. Only fractures with defined kinematics with certainty judgement of 2 and 3 are shown, excluding uncertain (1) interpretations, to make it more concise. For comparison, foliation measurements are added. Hornelen basin bedding measurement marked in purple. AFT sample locations are indicated in red. The defined subregions are marked in white.

4.3.4 Subregions showing different structural trends

Hornelen basin (0)

At the only locality in Hornelen basin, one fracture has been measured, striking around N-S and dipping steeply (76 °) to the W (Figure 14, appendix F: Outcrop no. 1). Based on calcite slicken fibres, the kinematics have been interpreted as sinistral with a low certainty (1).

North of the Nordfjord (1)

As mentioned before, almost all measured fractures showed signs of identifiable kinematics due to abundant mineralization (Figure 23). From the fracture orientations alone, no clear trend can be identified. However, it can be seen that fractures with normal kinematics mostly strike NNW-SSE and dip towards the west. Most fractures with dextral kinematics strike N-S dipping towards east. And E-W to NE-SW striking fractures show sinistral kinematics. Most fractures showed sinistral kinematics, followed by normal kinematics. It can also be observed that most slicken fibre kinematic interpretations have been assigned a high certainty. The foliation is steeply dipping to the SSE.

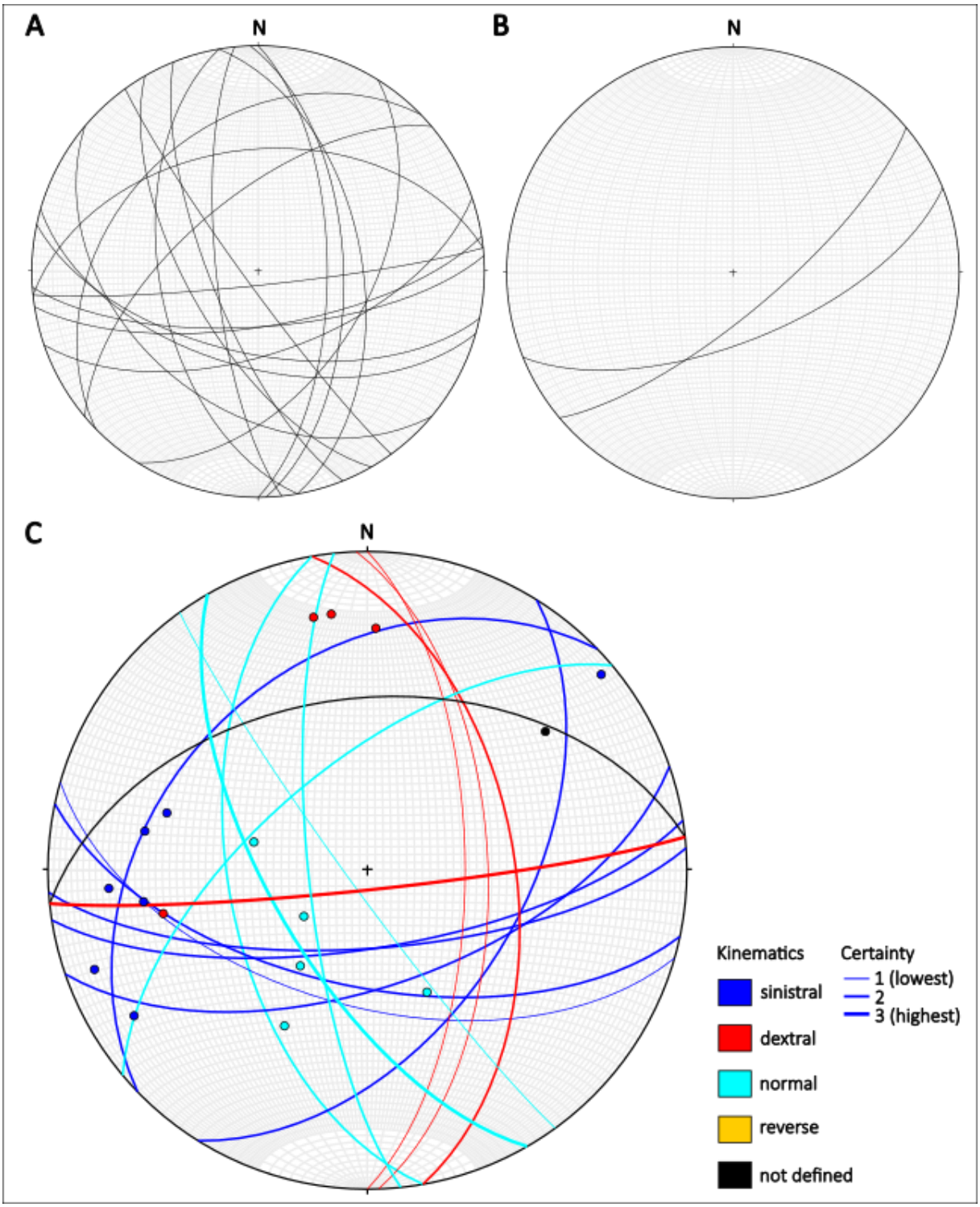

Figure 23: Subregion North of the Nordfjord (1). A: All fractures. B: Foliation. C: Fractures (drawn as half circles) with slicken fibre lineation (drawn as points), coloured after defined kinematic.

Western part of the Nordfjord (2)

A general preferred fracture orientation striking NNW-SSE and steeply dipping mostly west, but some also east, can be observed (Figure 24). The kinematics are mainly normal, but also sinistral, reverse and few dextral observations have been made. The foliation is either striking E-W with a fairly steep dip, or shallowly dipping towards the NE. No relationship between foliation and fractures can be observed.

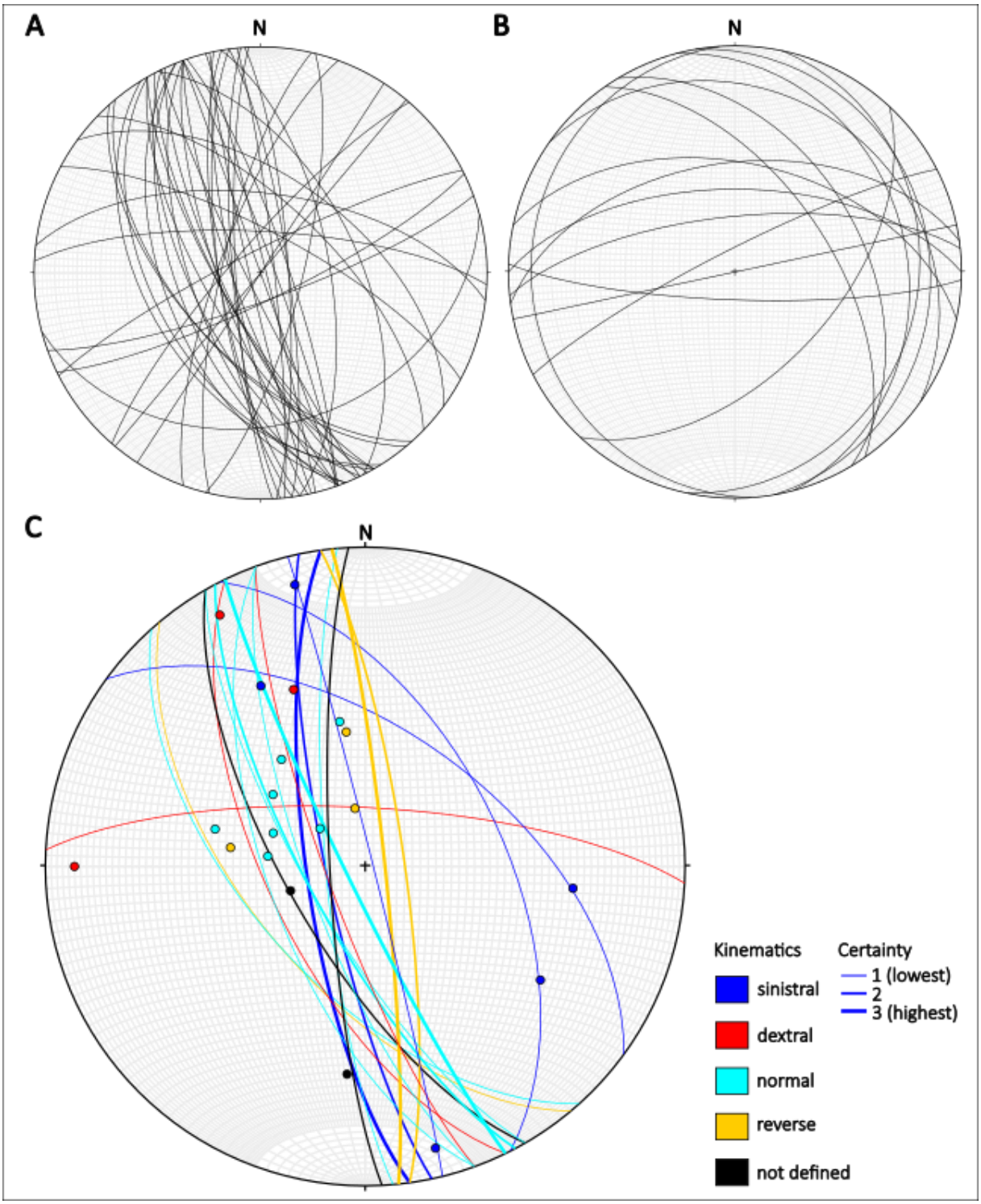

Figure 24: Subregion Western part of the Nordfjord (2). A: All fractures. B: Foliation. C: Fractures (drawn as half circles) with slicken fibre lineation (drawn as points), coloured after defined kinematic.

Eastern part of the Nordfjord (3)

A preferred trend of NE-SW- strike can be observed (Figure 25). The dip is less steep than in the Western part of the Nordfjord, but still quite steep. It can be seen that it is mostly parallel to the foliation. The overall kinematic is sinistral. Two normal faults are striking NNW-SSE as in the Western part of the Nordfjord. The steeply dipping foliation is striking NE-SW. The fractures here are mostly parallel to the foliation and movement seems to take place along foliation planes.

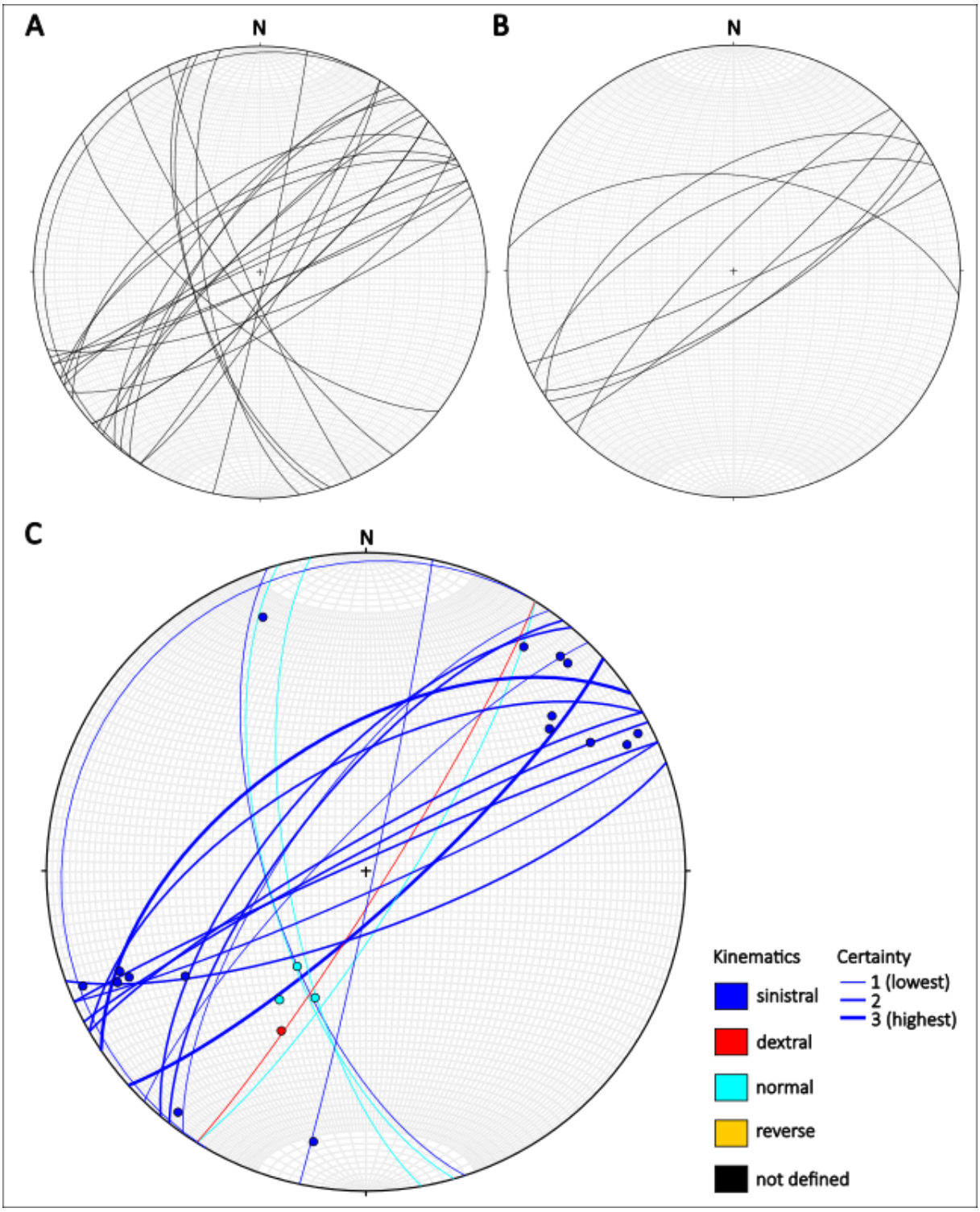

Figure 25: Subregion Eastern part of the Nordfjord (3 . A: All fractures. B: Foliation. C: Fractures (drawn as half circles) with slicken fibre lineation (drawn as points), coloured after defined kinematic.

Bremangerlandet (4)

On Bremangerlandet, fractures show a dominant E-W striking trend with a dip towards north (Figure 26). Another visible trend is steeply dipping, N-S striking. A very certain (3) interpretation assigned sinistral kinematics to a N-S striking fracture, however, all other fractures with visible kinematics were around E-W striking. Also these showed sinistral kinematics. The granodiorite on Bremangerlandet was not foliated.

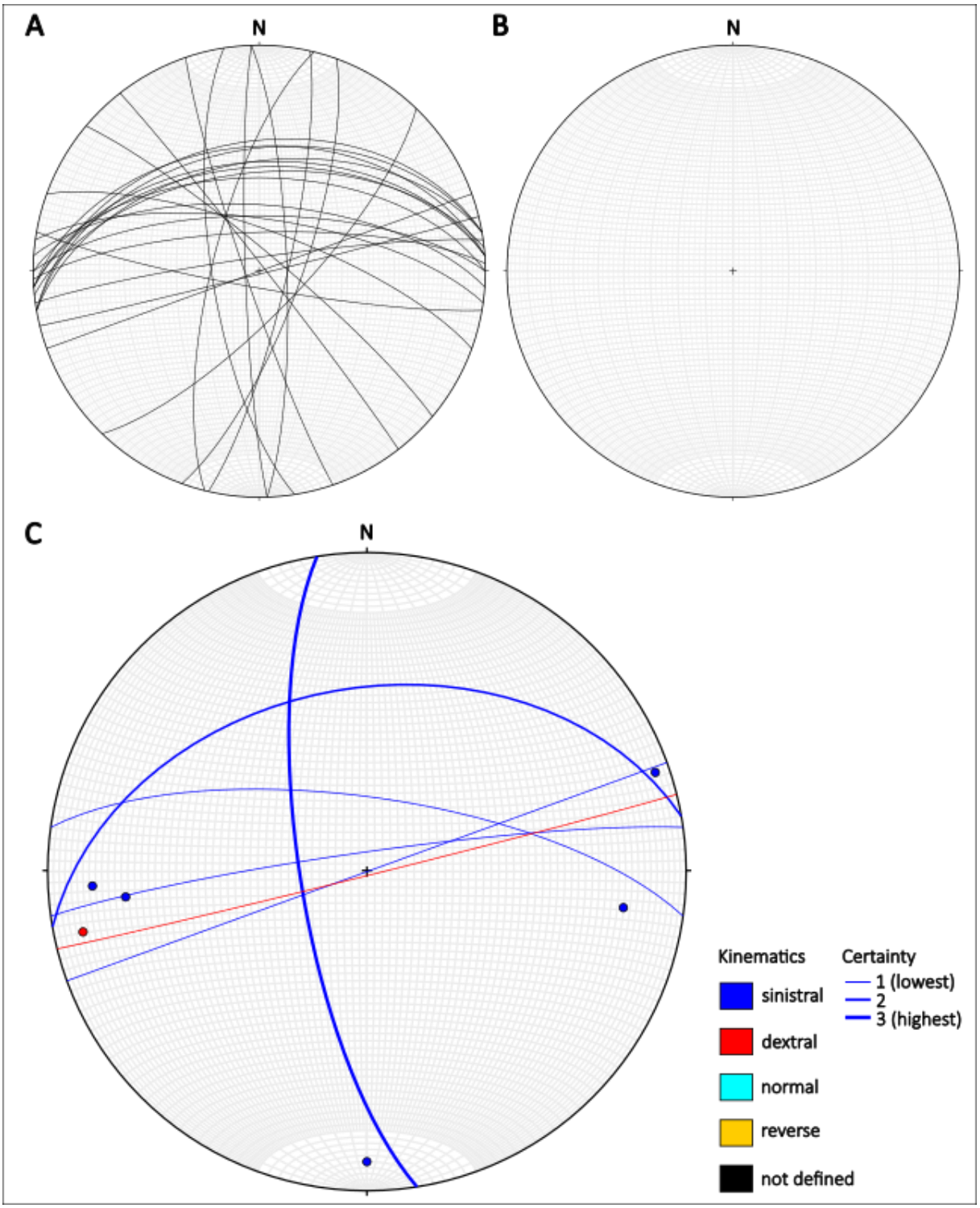

Figure 26: Subregion Bremangerlandet (4). A: All fractures. B: Foliation. C: Fractures (drawn as half circles) with slicken fibre lineation (drawn as points), coloured after defined kinematic.

Haukå fault (5)

Most of the fractures show a preferred NNW-SSE to NNE-SSW strike (Figure 27). Of the two directions, only the NNW-SEE striking fractures showed kinematics, which were mostly dextral. The kinematic interpretation was in general uncertain, as only little mineralization was encountered in this region and slicken fibres were weakly developed. A steeply dipping, NEE-SWW striking fracture has been interpreted to be a sinistral fault with much higher certainty. However, the fracture is located to the very east of the subregion (see Figure 15) and in addition, both the lithology (dark gneiss) and the slicken fibres (chlorite) differed strongly from the observations in the rest of the subregion (metasediments, zeolite/epidote). It can therefore be argumented that the locality should rather be included into subregion 6. The foliation is mostly shallow dipping towards north.

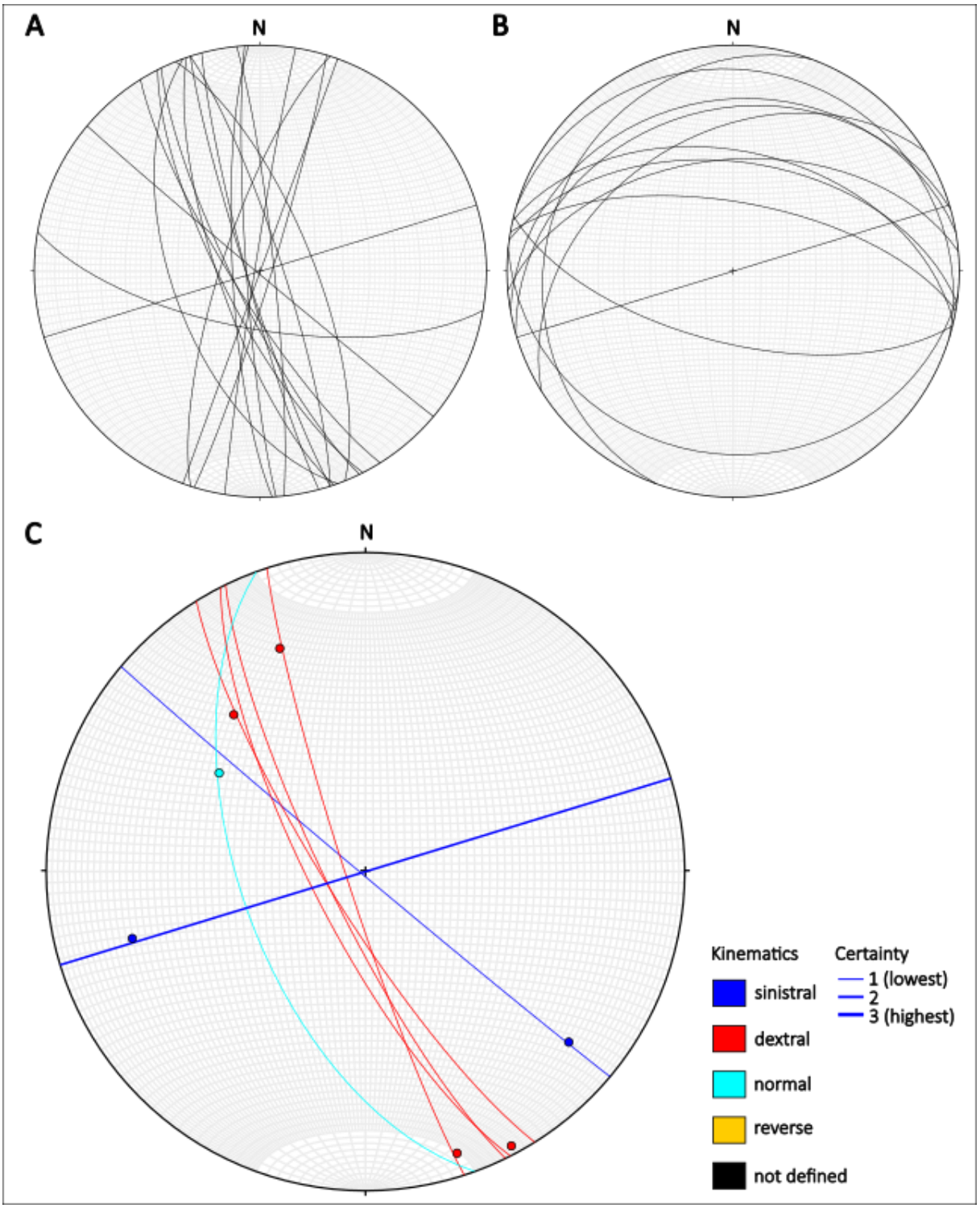

Figure 27: Subregion Hauså fault (5). A: All fractures. B: Foliation. C: Fractures (drawn as half circles) with slicken fibre lineation (drawn as points), coloured after defined kinematic.

Southern Middle Allochthon (6)

The fractures here are characterized by a roughly NNE-SSW striking trend and a minor around E-W striking trend (Figure 28). Both trends show sinistral and normal kinematics, around the same number of sinistral as of normal faults has been identified. Some dextral faults have also been identified, striking around N-S. The fractures are not parallel to the foliation. The foliation mostly shows a very shallow dip towards SE to NE.

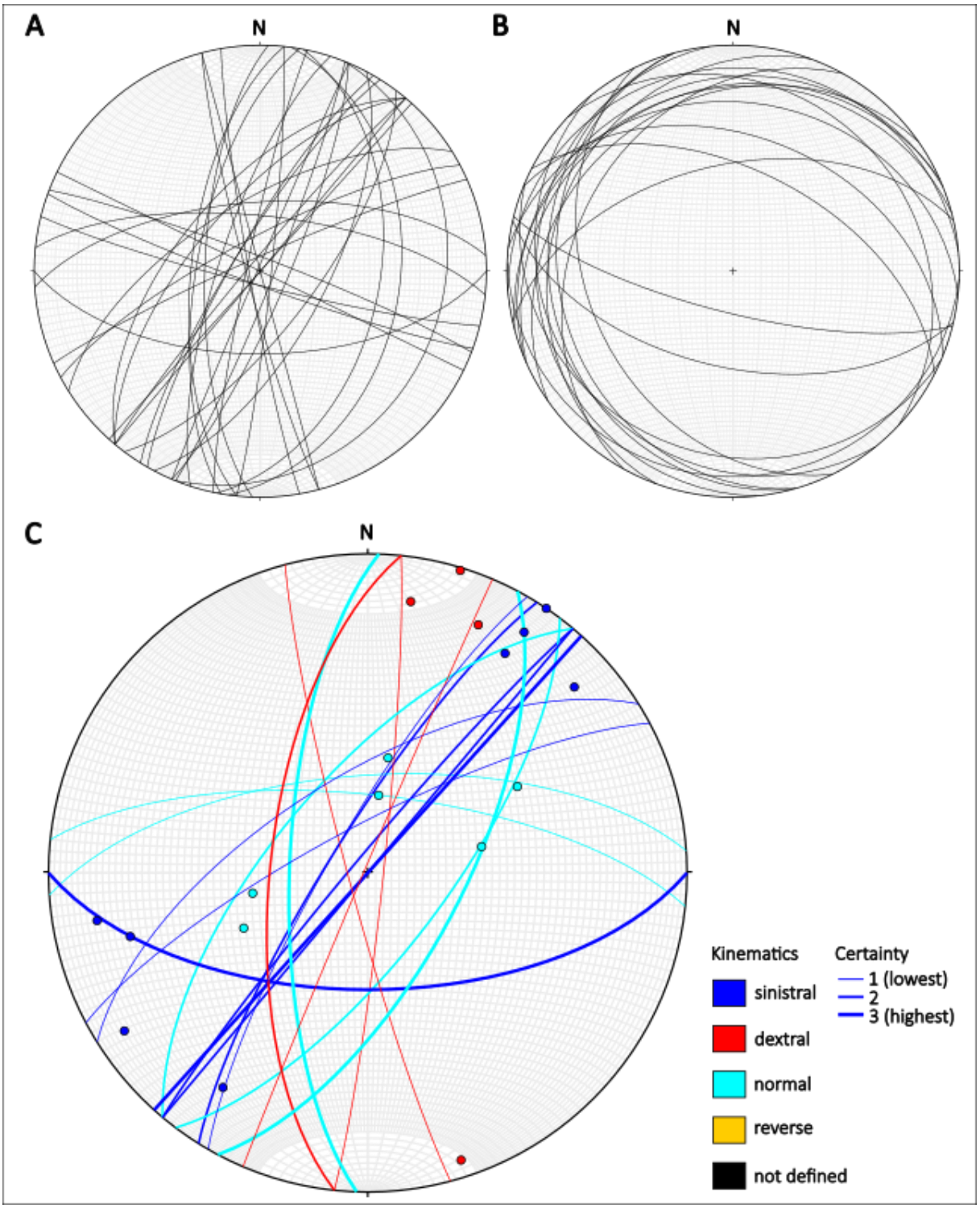

Figure 28: Subregion Southern Middle Allochthon (6). A: All fractures. B: Foliation. C: Fractures (drawn as half circles) with slicken fibre lineation (drawn as points), coloured after defined kinematic.

East of Hornelen basin (7)

NNW-SSE strike and a N-S to NNE-SSW strike (Figure 29). When it comes to kinematics, the most certain interpretations are sinistral NNE-SSW to NE-SW striking faults. The foliation is mostly shallowly dipping towards the south.

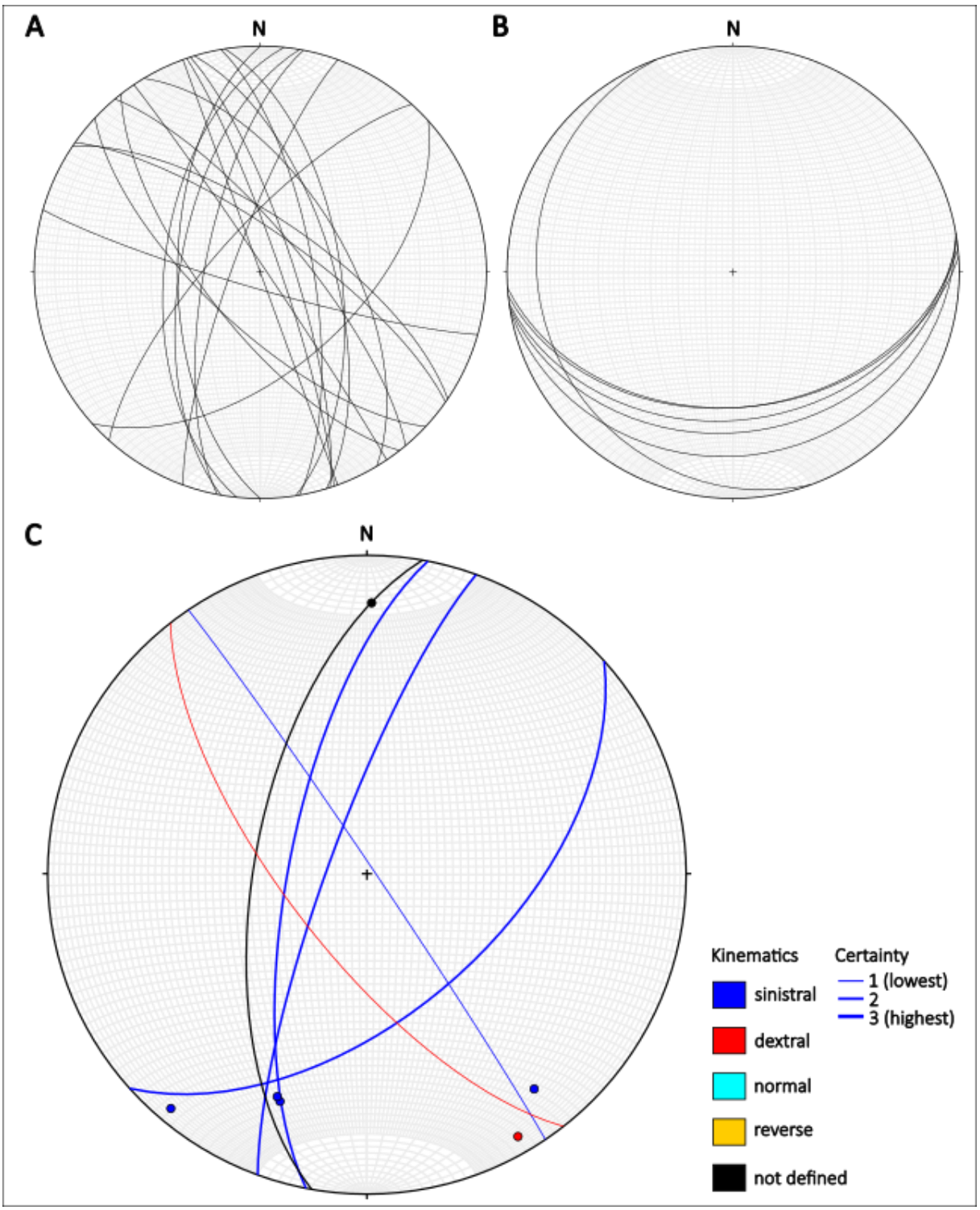

Figure 29: Subregion East of Hornelen basin (7). A: All fractures. B: Foliation. C: Fractures (drawn as half circles) with slicken fibre lineation (drawn as points), coloured after defined kinematic.

Far east (8)

At the far eastern edge of the study area, NNW-SSE to N-S striking fractures have been observed (Figure 30). Only one fracture showed vague dextral kinematics. The foliation is dipping roughly towards south.

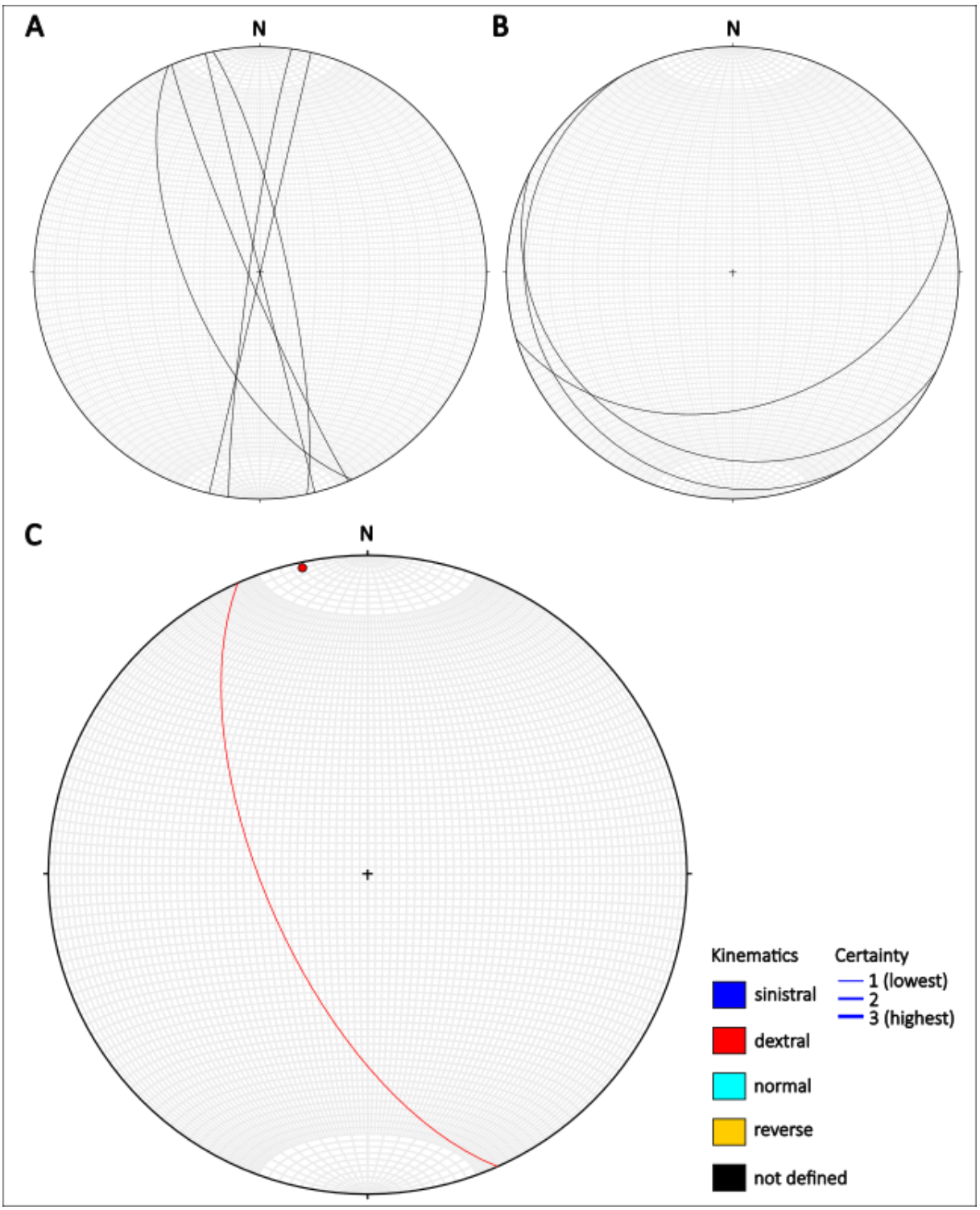

Figure 30: Subregion Far east (8 . A: All fractures. B: Foliation. C: Fractures (drawn as half circles) with slicken fibre lineation (drawn as points), coloured after defined kinematic.

5 Discussion and Interpretation

5.1 Reliability and validity

5.1.1 Apatite fission track analysis

Chi-square test

The 1σ error of all AFT ages obtained is very high., sample VAH_26 shows the highest error. It can be seen that the $p(x^2)$ value is higher and the dispersion smaller, the smaller the error is. In general, a low uranium concentration in a single grain can be observed to result in large single grain errors.

All samples failed the chi-square test ($p(x^2) > 0.05$) with values of 0.00 for $p(x^2)$. Normally, this is expected for sedimentary samples, indicating that there are several single grain age populations in the sample. All samples used in this study are either metamorphic or magmatic and the single grain ages in one sample can only capture one time-temperature history. Contamination may be a reason, however it would be an unlikely coincidence if that was the case for all samples. The same applies for varying compositions of single grains in the samples. As all samples are affected, it is most likely that the reason is either connected to the method in general or to the counting. The samples were counted by another analyst who also received very low values for $p(x^2)$.

A correlation ($R^2>0.29$) between single grain Dpars and single grain ages has been observed for samples VAH_23, 26 and 42, suggesting varying compositions of single grains in the samples. VAH_26 shows the strongest correlation ($R^2=0.47$). For all other samples the correlation can be seen as insignificant ($R^2<0.05$). It can be seen that $p(x^2)$ is smallest for samples with a strong Dpar-age correlation. Some samples showed in addition correlation of single grain uranium concentrations and ages with a tendency of samples with stronger internal Dpar-age correlation to also have stronger uranium-age correlations.

The analysed Durango standards did, expectedly, not fail the chi-square test, except the Durango analysed with sample VAH_26 (see Table 2 in section 4.1.3). It was also one of the two samples where the Durango age deviated strongest from the literature value of the Durango standard (31.44±0.18 Ma; McDowell et al., 2005). It shows in addition the largest error. No Dpars were measured during Durango counting as single grain compositions withing the sample are assumed to be more or less homogenous, which qualifies the Durango as a standard. The correlation of the uranium concentration and age within the Durango could be tested however, and it can be seen that it correlates with the $p(x^2)$ value of the sample. Samples with a high $p(x^2)$ value show a weaker internal uranium-age correlation. Samples VAH_42 and 78, which have the highest $p(x^2)$ values showed only an insignificant correlation

(R^2<0.004). Most Durangos showed a weak correlation of R^2 values between 0.141 and 0.22 and VAH_26, which failed the chi-square test had a R^2 value of 0.30. It can be seen that the analysed Durango ages are in general too low, but most are close within error margins, except for VAH_31 and 26. The reason can either lay in the counting or in the LA-ICP MS measurement.

However, as all samples failed the chi-square-test, not only the ones with a single grain Dpar-age correlation, and the Durango standard also was affected, methodological factors cannot be ruled out. The reason for this phenomenon could not be found as of now. It has to be stressed that LAFT is still a new method and there is a remaining need for basic methodological research. Even though the results seem plausible in comparison to other studies, this has to be kept in mind when putting weight to results from this study.

A possible explanation for the phenomenon may be that in the LAFT method, counting bias or bad counting has a stronger effect than in the EDM, as for the EDM both uranium concentration and number of spontaneous tracks are affected by counting, which is not the case for the LAFT method. Therefore, in the EDM, this effect may be irrelevant as it applies to both components in the equation.

Also 4 of the 59 samples by Ksienzyk et al. (2014) failed the chi-square test, which they could not explain as it was not due to differences in single grain chemistry. Ksienzyk et al. (2014) used the EDM.

LA-ICP-MS

Another source for erroneous ages in LAFT analysis is the placement of the laser spot during LA-ICP-MS measurements. The effect of zonation is avoided by careful selection of the counting area, avoiding internal zonation in the counting area, and placing the laser spot on the same area as counted. In spite of all efforts, slight differences between the placement of the laser spot and the counting area may be sources to errors.

Track length

The case of few measurable track lengths in a sample is seen as the largest source for bias and unreliability of track length measurements, as it is highly likely that not the full track length spectrum of the sample is reflected by the track length distribution if less than about 100 track lengths can be measured. Analyst specific measurement variation is reflected by track length calibration carried out on the Durango standard (section 3.1.3). Comparing with results by other analysts reported by Ketcham et al. (2015) shows that my measurements have a tendency to be slightly shorter (2%) than the average analyst, which is not enough to be in the

way of comparison to other studies. For Dpar measurements the difference is with 43% much higher and has to be considered when comparing to other studies. For both Dpar and track length measurements the calibrated personal factor is implemented into thermal history modelling.

Analyst bias

Analyst bias is the most vulnerable part of the AFT analysis for errors and has the highest impact. Donelick et al. (2005) has extensively described analyst bias, both for the EDM and the LAFT method. AFT analysis is highly dependent on conscious or unconscious decisions made by the analyst (Donelick et al. (2005). These are among others, selection, identification and, in case of counting, the decision whether fission tracks are inside or outside the area to be counted. These decisions are made based on criteria learned and practiced by the analyst. This bias is minimized by analysing standards, provided these decision criteria are the same in every count or measurement (Donelick et al. (2005). Another source for bias is knowledge of expected results and the analyst consciously or unconsciously attempting to produce an expected result. This bias was minimized by lack of knowledge of exact geographical location of the samples prior to analysis and age/MTL calculations carried out after all analysis was finished.

As this study is based on the LAFT method, the full zeta calibration previously required for EDM was not carried out. This means that training was limited and there is a less extensive calibration of the analyst than is common for the EDM. The Durango standard counts yielded ages close to the Durango standard literature age. However, the Durango standard is a nice sample with few dislocations or impurities and may not be a good measure for counting quality of other samples, requiring more sophisticated decision making when identifying which structures are fission tracks and which not.

5.1.2 Thermal history modelling

The inverse modelling is strongly dependent on the start- and end-constraints chosen. The most reliable models are obtained by an input from several methods into the same model, for example adding apatite helium and/or zircon fission track and helium thermochronology. Using only apatite fission track as done in this study, thermal history models are poorly constrained and allow for a great variety of thermal histories. They give a suggestion for a thermal history supported by the sample, however, the true thermal history may be very different.

5.1.3 Structural field work

Measurements should only be influenced by the compass error and the user's selection and understanding of the structure to be measured. During field work it has been observed that the compass is sensitive to moisture and the needle could stop before it was done 'swinging' around the correct strike/dip number on the compass. This may have been a source of error on a few occasions marked as comments in Appendix E. In general, only easily accessible outcrops along roads were used, this can bias the results, as outcrops offroad and less easily accessible, may show very differently oriented fractures and different kinematics and are not samples. Some fracture planes selected for measurement were very small and it is uncertain whether kinematic interpretations from these reflect large scale kinematics/faults. In general, these very small planes were only used if several of these could be found at the same outcrop.

The kinematic interpretation in general is the least reliable part of the method, as it is strongly subjective and dependent on the knowledge and ability of the geologist. It involves recognition and selection of measurable slicken fibres, interpretation of slicken fibre tear-off edges and certainty judgement of the personal interpretation. Interpretations and judgements may be very different between geologists. The same applies for description of lithology and slicken fibre mineralogy.

In addition, kinematic interpretations may be biased by expected kinematics after having had several similar interpretations. However, care was taken that previously defined kinematics in the region were unknown prior to field work. No maps or plots were drawn during field work in order to reduce bias. In addition, regions were visited repeatedly on different days and without having a clear overview of the interpreted kinematics, reducing the likeliness of making similar interpretations due to bias. The results show a variety of kinematic interpretations and patterns, agreeing with results from other studies, can be observed, validating the method.

During field work I preferably measured faults with mineralization or ideally, slicken fibres, in order to obtain information on kinematics. Therefore, fracture orientations without mineral growth may likely be under sampled. Also, most datapoints are therefore in outcrops with many faults with slicken fibres. As fractures without slicken fibres may have very different kinematics than those interpreted from other faults, the total picture may be very different. However, it is not possible to avoid this bias.

5.2 Implications from AFT ages

Apatite fission track ages in Norway range from around 320 to 80 Ma (see e.g., Green et al. 2022). The ages obtained in this study lay inside this range within error margins. Comparing with the overview by Green et al. (2022), the MTL range obtained in this study, based on the 3 samples with 100 or more measurable track lengths, is with 11.91± 1.60 to 12.29±1.67 µm (mean MTL: 12.13 ± 0.20 µm) among the lowest MTL measured in Norway. The MTL of samples from Norway range from about 11.6 to 14 µm, excluding errors and outliers (e.g., Green et al., 2022). This supports the assumption made in section 4.1.2, that the samples show comparably slow cooling.

5.2.1 Age interpreation

The oldest ages (325 ± 41 and 305 ± 32 Ma) in the south match the first Late Carboniferous exhumation period from Green et al. (2022), after the Devonian extension (see Figure 11 in section 4.1.1 for sample loations). However, due to the large error, they could also match early Permian rifting periods or for the oldest sample, Late Devonian extension.
Samples further north showed Triassic to Cretaceous ages. Still south of the Nordfjord, inland, is the only Late Triassic age (223 ± 22 Ma). Two well constrained Early Jurassic ages are located close to the Nordfjord on the southern bank (192 ± 10), and at the coast (187 ± 14). Another coastal sample to the north gave a Middle Jurassic age (166 ± 22). A well constrained Late Jurassic age is located furthest inland to the east (149 ± 9). The youngest sample of Early Cretaceous age is located centrally on the northern bank of the Nordfjord (133 ± 9).
The Late Triassic age could, within error range, correlate with Rift phase 1 in late Permian-Early Triassic. After Fossen et al. (2017), many of the brittle Devonian structures were reactivated (as low-angle normal faults) during the North Sea rift phases. It would be likely, that the Hornelen detachment fault west of the sample may have been reactivated during rift phase 1, exhuming the sample located in the footwall block. Unfortunately, no time-temperature model could be generated for the sample, thus no support for the speculation can be obtained. The two Jurassic ages between the two rift phases may be related to ongoing rift flank uplift, whereas the Late Jurassic-Early Cretaceous samples may be related to rift phase 2. However, the AFT age itself does not necessarily give a sensible estimate, as the thermal history most likely is more complex. In cases of very fast cooling through the PAZ i.e., rapid exhumation, suggested by very long track lengths, the age may approximate the timing of passage though the PAZ. However, in this study, all samples showed very short track lengths,

except for VAH_78 (Late Jurassic) which could not be measured and is therefore lacking this information.

5.2.2 Age offsets and fault activity

The ages do, however, give information relative to each other. From the age-elevation plot in section 4.1.3 it has been seen that ages do not correlate with elevation as is expected from thermochronological data. In addition, several misfits and inconsistencies can be observed, as ages at similar elevation show extreme age differences or similar ages are located at very different elevations. In addition, an inverse relationship of young age at high elevation and old age at low elevation has been observed, which should be opposite for AFT data (compare Figure 31). To accommodate for these misfits and for offsets in ages, tentative normal faults have been drawn in Figure 31. Fault orientations may be very different, and the faults could also be oblique-slip faults, which is likely, as a majority of kinematics observed during field work were either strike-slip or oblique-slip to some degree. Especially for the north of the study area, fault activity is suggested (Figure 31a). Main fault movement is assumed between sample VAH_78 in the east, showing a young age at high elevation, and the samples to the west, in particular VAH_42, showing comparably old age. The samples are separated by the Bortnen fault, therefore fault movements here may result in VAH_78 being in the footwall and VAH_42 in the hanging wall of a moving fault. The Late Jurassic age of VAH_78 may point to fault activity during this time. Fossen et al. (2021) dated the Bortnen fault to Permian-Early Cretaceous, which would be compatible with Late Jurassic faulting. In addition, smaller localized fault movements between the samples to the west are suggested.

VAH_48 in the very north of the study area is suggested to be offset from the samples further south (Figure 31b).

For the samples in the very south of the study area (Figure 31c), it is assumed that there is some kind of offset between the highest sample VAH_26 and VAH_31 to the east. The strongest offset is between VAH_26 and the lowest, coastal sample VAH_23. The ages are very similar, while there is almost 50 m elevation difference between the sample. It is assumed that there is a normal fault between the two samples, however, it would need to be a fault with a rather major offset. In addition, VAH_23 is located in the Florø horst, with major normal faults to the north and south. It seems unlikely for it to be in the hanging wall of a major normal fault to the east. Ksienzyk et al. (2014) suggested reburial (up to 30-50°C) during Cretaceous to earliest Paleogene of coastal samples in the Bergen area. It is possible that VAH_23 was reburied to a depth above the PAZ, the absence of annealing would preserve the old age, while sedimentary burial and flexural uplift may cause the elevation

difference between the two samples, preserved after the erosion of the overlying sediments. However, it is questionable whether this process could account for an elevation difference this large. It may be a combination of both reburial and faulting. Weak normal fault kinematics were observed between the two samples during field work, and the area to the south yielded a variety of normal NE-SW- striking kinematics, supporting the likeliness of normal faults, in different orientation, overprinting the E-W trending faults adjoining the Florø horst. The suggested reburial by Ksienzyk et al. (2014) was tested during thermal modelling by setting constraints after Ksienzyk et al. (2014). Primarily on the coastal sample MLM_134, but for test reasons also on the two samples more inland (VAH_44-2 and 42). All samples could be modelled to be reburied up to 30-50°C during Cretaceous to earliest Paleogene and showed high agreement. This is seen to be an unlikely result, at least for sedimentary burial, as e.g., VAH_42 is located quite far inland and at a present-day elevation of 41 masl. Another process that could cause age offsets is differential erosion of sediment cover or basement rocks, as different rock types are more prone to erosion than others.

Periods of fault activity by Ksienzyk et al. (2016) for the Bergen area are Late Devonian–Early Carboniferous (>340 Ma) related to the decreasing Caledonian orogenic collapse, Carboniferous–Mid Permian (305–270 Ma) related to the onset of phase 1 rifting, minor Late Triassic–Early Jurassic (215–180 Ma) between rift phase 1 and 2, and Early Cretaceous (120–110 Ma) suggested either to be a late response to rift phase 2 or correlated to the initiation of rifting in the North Atlantic. Especially the last two periods may explain fault offsets between the samples in this study, however it is questionable whether the study areas can be compared due to the lateral distance.

K–Ar fault gouge ages by Hestnes et al. (2022) from a study area containing the area of this study, show Late Jurassic to Cretaceous ages. One faulting event points to the Late Jurassic offshore rift phase 2 and two younger extensive faulting events under a WNW–ESE transtensional stress regime during Middle (123–115 Ma) and Late (86–77 Ma) Cretaceous times point to periods of increased tectonic activity in the Norwegian Sea (Hestnes et al. 2022). These observations support the suggestion made in this study that AFT ages are offset due to fault activity. The suggestion of fault offset across the Bortnen fault in Late Jurassic, would fit well with the Late Jurassic faulting event correlating with rift phase 2 suggested by Hestnes et al. (2022).

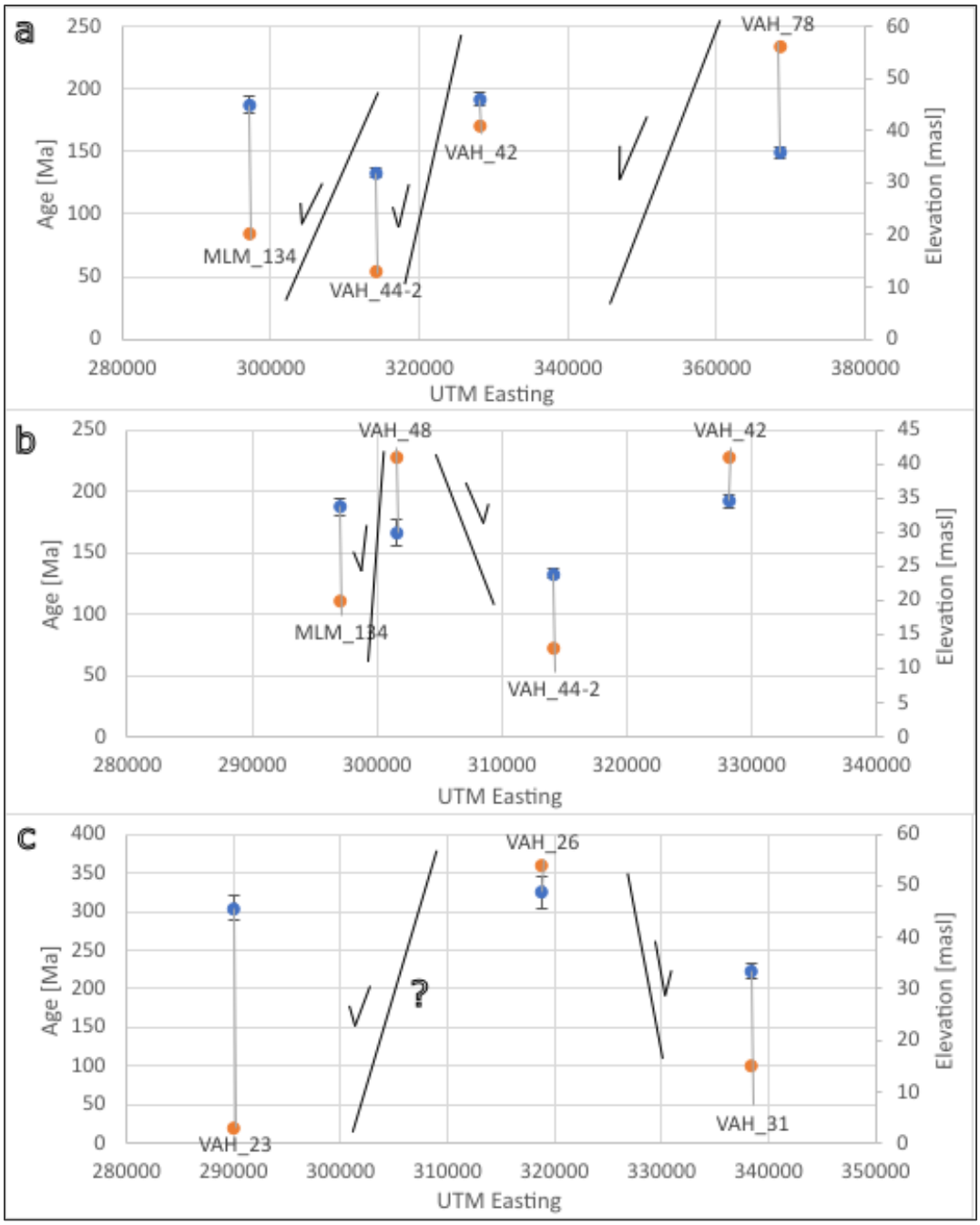

Figure 31: Age – elevation – UTM Easting plot with tentative fault suggestions between the samples. Error margin (1σ) for ages are given. a: samples north of Hornelen basin excluding VAH_48 for better manageability. b: samples north of Hornelen basin excluding VAG_78. C: Samples south/east of Hornelen basin.

5.2.3 Thermal history

The most likely thermal evolution suggested by thermal modelling is cooling i.e., increased exhumation (~1.5-2 °C /Ma), reflecting Devonian extension and continuing through rift phase 1. At the onset of rift phase 2, two of the three modelled sample had exhumed above the PAZ and the third sample was in the process of doing so. No increase in exhumation during rift phase 1 could be seen in the models. However, all models are wide below the PAZ (shown in

Figures 14-16 in section 4.2) and would allow for a less steep cooling during Devonian times and a steeper cooling during rift phase 1. Here, zircon low temperature thermochronology could help constrain the model as the PAZ is located at higher temperatures. The most likely interpretation of the thermal history suggested by the models, based on the data at hand, is comparably fast cooling driven first by Devonian extension and then rift phase 1, either through faulting or rift flank uplift. From around 250-150 Ma until present, the samples were slowly and gradually exhumed until present-day elevation (~0.2-0.4 °C/Ma). From the three samples, the eastern most (VAH_42) passed the PAZ earliest and shows the steepest and most constrained cooling. While the other two samples would allow for more or less gradual cooling until present, this is not the case for this sample. VAH_42 is also at the highest elevation today, 20-30 m higher than the other two samples. From around 240 Ma, it shows slow exhumation until present-day surface. The other two samples are not clear about whether the steep cooling continues through the PAZ until 200 Ma (MLM_134) or 150 Ma (VAH_44-2) or is followed from 250 Ma by a shallower cooling path until present. After the models, all samples are above the PAZ latest by 100 Ma.

The change from fast cooling to slow cooling was also observed in modelling done by Ksienzyk et al. (2014) on samples around Bergen. They reported the change to occur in Early Jurassic (~200-170 Ma). The samples modelled in this study show a change between about 240-225 Ma, 225-200 Ma and 170-150 Ma for each sample respectively, which can be seen as similar. Ksienzyk et al. (2014) reported higher cooling rates of 2-3°C/Ma in Permian-Triassic and much lower cooling rates of <1°C/Ma from the Jurassic. This is in agreement with this study, even though pre-Jurassic cooling rates have not been estimated to exceed 2 °C/Ma.

Johannessen et al. (2013) more inland in the Hardangerfjord region reported two distinct periods of increased cooling (2–6°C/Ma) during Permian-Triassic, explained by flexural rift shoulder uplift, and latest Cretaceous-Cenozoic. Samples in this study can agree with Permian-Triassic flexural rift shoulder uplift as reported by Johannessen et al. (2013). However, to generate as steep a cooling as observed by them, there should be no faster cooling response to Devonian extension and instead a steeper cooling path in Permian-Triassic than the 2 °C/Ma reported in this study. It may be that Johannessen et al. (2013) sat a significantly different start-constraint, which may be explained by regional differences. The models in this study would allow for this cooling history, but the models do favour a cooling history with pronounced cooling through Devonian extension and Permian-Triassic. However, both thermal histories do not necessary conflict. It is very likely that the samples in this study

were first cooled by the Devonian extension and then by Permian-Triassic flexural rift shoulder uplift. The increased colling period in latest Cretaceous-Cenozoic has not been observed in this study.

The first three periods of enhanced exhumation (311–307 Ma, 245–244 Ma and 170–167 Ma) by Green et al. (2022) are in agreement with this study, even though no distinct separate periods have been observed. However, between the samples, VAH_42 shows high agreement with the second period, while VAH_44-2 shows very high agreement with the third period. MLM_134 seems to be a bit in between.
A Miocene peneplanation followed by Miocene uplift as proclaimed by Green et al. (2022) could not be seen in the models, as all three samples were exhumed above the PAZ before 100 Ma at the latest according to the models. Here, an inclusion of apatite (U-Th-Sm)/He data into the models may give a better resolution of the younger history.

The offsets between the models could be explained by the difference in elevation of the samples, but then they should still show the same thermal history. While they still show a very similar thermal history, it is interpreted that they share the same underlying driving mechanisms for exhumation but show overprint and minor offsets due to local fault activities as suggested previously. These local faults may show larger or smaller offsets and be active to different times. From the model offsets, it can be suggested that VAH_42 was influenced by older fault activity, followed by MLM_134 and lastly, VAH_44_2. Timing of exhumation of the samples through the PAZ could set fault activity to an approximated timing of >250, 225 and 170 Ma respectively. The earlier and more pronounced exhumation of VAH_42 is likely due to its position in the footwall of a fault with a downfaulted block to the north-west. As has been discussed before, it is suggested that it is also part of a hanging wall block of a fault to the east based on the age elevation relationship compared to VAH_78.

Redfield et al. (2004, 2005b) studying AFT data in the north across the MTFC, suggested a Mesozoic to Cenozoic exhumation history significantly offset across major structural blocks. Both Ksienzyk et al. (2014) and Johannessen et al. (2013) studying AFT data in the south, stressed the importance of fault activity as the studied AFT ages were offset across faults. They concluded that the sustained topography was most likely periodically rejuvenated during the Cenozoic because of reoccurring tectonic activity. This study is in agreement with these observations and conclusions, suggesting a very similar evolution for the Nordfjord region located between their study areas. The data obtained in this study showing vertical offset

between AFT ages supports previous studies stressing the importance of faulting during post-Caledonian.

5.3 Structural activity in the region

Essentially two main types of fractures have been observed in the study area. The first type is ~ N-S-striking fractures, which are mainly NNW-SSE striking in the north and NNE-SSW striking in the south of Hornelen basin. They are mostly steeply dipping towards the west. They show mainly normal kinematics, closely followed by sinistral kinematics. The second type are E-W to NE-SW striking fractures which show mainly sinistral kinematics, but some normal kinematics have been observed in the south of the study area. They show a less steep dip and are often parallel to the foliation and along older Devonian extensional structures.

Based on the majority of strike-slip followed by normal slip observed in the study area, the overall kinematic regime can be seen as transtensional.

Fossen et al. (2017) also observed a NW, NE and N-S trending (coast parallel) fracture population. As a second type, they also observed a more E-W striking population in areas associated with Devonian basins. They proclaimed that the variety of orientations suggests that the structures did not form in a single stress field and during more than one phase of deformation. After Fossen et al. (2017), the NE-SW striking faults are consistent with Devonian NW-SE brittle extension (Mode III) following ductile Devonian precursors. NE-SW striking faults have been mainly observed in the east and south of the study area (Figure 21, 22). Similar to Fossen et al. (2017), I observed E-W and NE-SW oriented faults associated with the Devonian Hornelen basin and the Bortnen fault. As previously observed by movement along the fault was interpreted to be Young et al. (2011) also I observed mainly sinistral kinematics and some minor normal kinematics. Fossen et al. (2017) also stresses that many of the brittle Devonian structures were reactivated (as low-angle normal faults) during the North Sea rift phases. They interpret the ~N-S trending faults to indicate east–west opening related to the Permo-Triassic rift-related faulting in the North Sea. However, also the NE-SW and E-W striking structures may have been involved in faulting related to the North Sea rift phases. Reeve et al. (2015) pointed to offshore NE-SW trending faults associated with the North Sea rift, which formed in intrabasement weaknesses. They argue that rotations in extension direction are not required to generate multiple fracture set orientations.

Also Fossen et al. (2021) argumented that the onshore basement was significantly involved in North Sea rifting since 70% of illite K–Ar ages of dated faults showed Permian-Early

Cretaceous ages. They dated onshore faults to be active from late Devonian, with distinct Permian and Jurassic peaks in the early stages of the two rift phases.

Hestnes et al. (2022) studied a larger area including the area studied in this study and also observed a N-S, NE-SW and E-W directed trend in fracture orientations. They also observed a minor fraction of NW-SE trending fractures. Slicken line orientations in their study, termed slicken fiber orientations in this study, also showed predominantly strike-slip kinematics, followed by oblique-slip and lastly dip-slip. They state that NE-SW and E-W trending fractures are inherited from brittle precursors, in turn formed in ductile precursors, as they also observed brittle faults in this orientation being parallel to the foliation. They suggest that the N-S and NW-SE trending fractures are newly formed, mainly strike-slip faults. They suggested therefore a Late Devonian to early Carboniferous age of the N–S trending fractures, opposing previous models where N-S trending fractures were interpreted to have mainly originated during the North Sea Permo-Triassic or Jurassic E–W rifting. Contrary to Hestnes et al. (2022), most of the N-S/NNW-SSE striking faults I observed showed normal kinematics, suggesting to not completely abandon the influence of North Sea rift related faulting for the study area.

5.3.1 Paleo-stress field and kinematic regime

In order to estimate a stress field for the study area based on the observed fault and fracture orientations and kinematics, paleostress analysis was carried out using the software WinTensor by Delvaux and Sperner (2003). All data was used and no division in subsets was undertaken. The assumption here is that the program will give out the model fitting most of the data and therefore showing the most dominant stress field. However, it has to be noted that the fractures and kinematics most likely formed and were reactivated/overprinted during different times in different stress fields. A sensible approach here would be to date groups of similar fracture orientations/kinematics and/or use information from the relationship of mineral type of slicken fibres and the temperature regime to define groups of fractures which were active at the same time and in the same stress field, as has been done in a recent study by Hestnes et al. (2022). Concerning the mineralization-temperature regime, however, it has to be added that the relationship may be obscured as the slicken fibre mineralogy may result from temperature and composition of the circulating fluid and not the general temperature in the region.

Of the total 198 fractures measured during field work, 96 faults had measurable slicken fibre orientations and for 92 of those, kinematics could be defined. Those 92 were all included in

the model. The model suggests principal stress axes σ1, σ2 and σ3 and shows an overall strike-slip regime with a N-S directed maximum stress tensor (σ1, compression). The suggested extensional E-W directed stress tensor (σ3) is not well defined by the data, as it is supported by less than 7 faults (hollow arrows, Figure 32). The strike-slip regime suggested by the model makes sense as most kinematics defined were sinistral strike-slip. The N-S compressing stressor in a strike-slip regime may result in opening of N-S trending extensional fractures, as was observed as N-S trending normal faults in the study area.
However, the stress tensors do most likely capture a number of different stress regimes during geological history as the faults and kinematics were most likely formed at different times in different stress fields. As I did not date fault activity, I cannot say when which faults were active and which stress regime they belonged to.

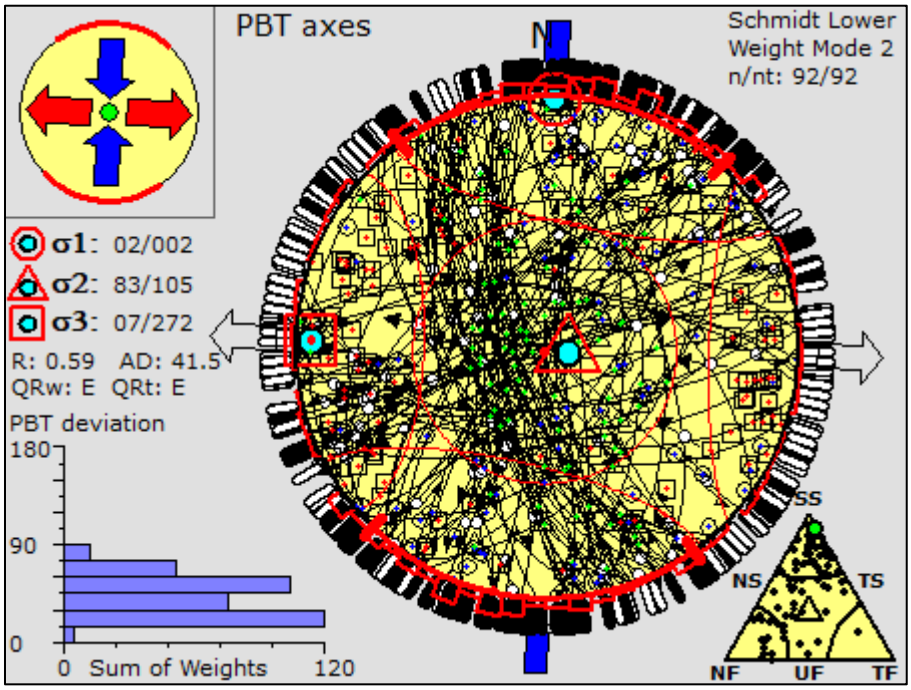

Figure 32: Paleostress analysis using WinTensor showing the principle stress tensors σ1, σ2 and σ3. Hollow arrows indicate stress tensors supported by less than 7 faults. The suggested stress regime based on kinematics shown in the lower right. SS: strike-slip, NF: normal fault, TF: reverse fault, oblique kinematics in between.

Fossen et al. (2017) showed in a summary of fault-slip analyses of a region stretching from the study area of this study until the Hardangerfjord in the south, that extension direction and kinematic regimes show variation across the region. While extension direction is mostly NW-SE, analogue to Devonian extension, in the south, he showed a E-W extension direction in the area approximating the study area of this study, which fits with the results from this study. However, he suggested a general normal faulting kinematic regime and did not talk about strike-slip kinematics.

Phillips et al. (2019) suggested for the northern North Sea, that heterogeneities such as basement shear zones may cause nearby or newly forming faults to locally align with the already existing structure instead of being oriented perpendicular to the extension direction. This may locally perturb the regional stress field. As normal faults show very different orientations in the north (NNW-SSE to N-S) and in the south (NE-SW) of the study area, a test paleostress analysis was carried out in WinTensor for both north and south separately. Due to the orientation, it is assumed that the faults in the south formed in ductile precursors and the orientation does therefore not necessarily reflect the stress field. The result for both areas was that the around west directed σ3 direction (extension) became supported by more than 7 faults (filled arrow), which was not the case in the model using all data (Figure 32: both E and W directed arrow is hollow). For the south, the model rather showed an WNW pointing σ3 direction, and for the north the model showed a rather WSW pointing σ3 direction. It can be assumed that in the model combining all data (Figure 32), these two directions rule each other out. Rather than assuming a different stress field between north and south, it can be suggested that fault orientations determined by heterogeneities or precursor structures, perturb the analysed paleostress field, analogue to Phillips et al. (2019). This points to the suggestion that paleostress field analysis may be less applicable for regions where old basement structures influence fault orientations as is the case for this study area. These structures would still be active in the same stress field even though their orientation is less preferable. It would be likely that this could lead to strike-slip or oblique faults being active in an extensional rift setting where newly formed faults would show normal kinematics. Phillips et al. (2019) states furthermore that faults striking at a high angle to the rift may segment faults and rifts in the North Sea and may transfer strain. Also this may be applicable to this study area and explain sinistral strike-slip kinematics, dominantly around the ~E-W striking Bortnen fault.

Hestnes et al. (2022) worked extensively with paelostress analysis across an area slightly larger than this study area. They interpret epidote-, chlorite- and quartz-bearing fractures and faults to have initiated mainly in the Middle Devonian to early Carboniferous in two distinct paleostress fields. Excluding quartz, epidote and chlorite were the main slicken fibre mineralizations observed in this study. The first field shows NW–SE compression and the second field shows strike-slip stress regimes, where the σ3 direction changes from NW–SE in the south to E–W in the north. They interpreted the change in stress tensor direction to result from increasing strain partitioning closer to the MTFC in the north. This may possibly also explain the N-S differences between the paleostress models observed in this study. The

second field modelled by Hestnes et al. (2022) agrees with the modelling results in this study, with an E-W directed σ3 direction and a strike-slip regime. They only observed few fractures and faults bearing epidote, chlorite and quartz to fit into purely E–W extensional local stress regimes related to North Sea rift phase 1. They stress that the region shows a strike-slip architecture, different to the dip-slip architecture further south, as has been postulated by e.g., Fossen et al. (2017), indicating a more prominent transtensional/strike-slip regime from the Late Devonian onwards north of Sognefjorden.

5.4 Implications from both structural geology and AFT dating

Attempting to explain offsets between AFT ages with the structural field data, it has to be stressed, that due to the simplification of kinematics into dip-slip and strike-slip (see section 3.2.2) in order to be able to show differentiated kinematics, oblique slip is not reflected by the data. However, almost all faults observed during field work showed oblique slip. Only some showed very clearly strike-slip and only at few locations in subregion 2 (Western part of the Nordfjord) clear dip-slip has been observed. This suggests that many of the faults interpreted as strike-slip, may have contained a dip-slip component, allowing for offset of AFT ages.

The abundance of N-S trending normal faults around the western part of the Nordfjord and the fault offsets suggested by the AFT ages, implies extension in the north of the study area. The picture around the Hornelen basin is likely more complex due to the influence of precursor structures such as the NSDZ. It may be that formation of new, preferable fractures is easier in the northern part leading to stronger extension in the north than than in the south. Sinistral strike-slip along Bortnen fault and other around NE/SW and E-W oriented precursor structures may be explained as reactions to balance the built-up stress regime resulting from differential extension. Parts of the Bortnen fault, separated by bends, as shown in Figure 33, may be reactivated either as normal faults or sinistral strike-slip depending on preferences due to the orientation of the respective part. The result could be the transtensional regime observed. This is similar to faults striking at a high angle to the rift segmenting faults and rifts and transferring strain as suggested for the North Sea by Phillips et al. (2019).

On Figure 33 I attempt to incorporate sinistral kinematics into an extensional setting, with sinistral movement taking place along older structures especially further inland. In addition, faults inside the bended Bortnern fault could likely be reactivated with normal kinematics in the more N-S oriented part and with sinistral kinematics in the more E-W directed part. As mentioned before, the movement may be due to balance stresses in the lithosphere due to differential extension and localized, smaller, normal faulting. The estimated faults in the

Figure 33 are based on extrapolations of kinematic interpretations and their fault orientations made during field work. The picture, however, has been simplified and schematized for illustration purposes, with a disproportionately high amount of normal kinematics. It can be seen that faults with normal kinematics around the western part of the Nordfjord are oriented parallel to incisions such as bays trending around N-S, making the suggestion of relevant faults offsetting AFT ages in this area highly likely. The offset between the AFT samples west of the Bortnen fault and the sample east of it, could be explained by partial reactivation of the Bortnen fault as normal faults, possibly during rift phase 1, as suggested above. Similar suggestions have been made by Redfield et al. (2004, 2005b) about the MTFC north of this study area. However, normal kinematics along observed along Bortnen fault are oriented in an angle to the overall fault orientation (see Figure 33). These normal kinematics have been observed on fractures oriented NE-SW, parallel to valleys and fjords in this area. This would make it likely that the ages are not offset by Bortnen fault, but by an unknown, major (or several) NE-SW trending fault. This fault, or similar faults, seems to continue southwards, following the incised valley and fjord, as strike-slip and normal faults east and south of Hornelen basin, are in line with it. Here, normal kinematics on east dipping fractures has been observed, supporting the suggestion the sample VAH_31 to the east may have been downfaulted. Normal kinematics observed between VAH_26 and VAH_23 to the very west, were uncertain and few, as illustrated by a weaker symbol (Figure 33).

Redfield et al. (2005a) also observed different kinematics along the MTFC north of this study area. He observed fault planes which were dominated by both dip-slip (normal) and further north oblique/strike-slip components, which he interpreted as relict of older events. The abundancy of sinistral strike-slip kinematics observed in this study opens for discussion on whether these actually are only Devonian relict structures or whether the onshore response to rifting not only involved normal faulting, but also strike-slip, possibly to balance built up stresses in the area due to localized normal faulting. Observed sinistral strike-slip also along N-S trending faults in this study and by Hestnes et al. (2022), suggests that normal dip-slip and sinistral-strike-slip are most likely closer related in the study area than previously thought.

AFT dating carried out in this study support models involving onshore normal or oblique-slip fault activity during and/or after rift phase 1 and 2, as these are required to explain offset between the AFT ages in this study.

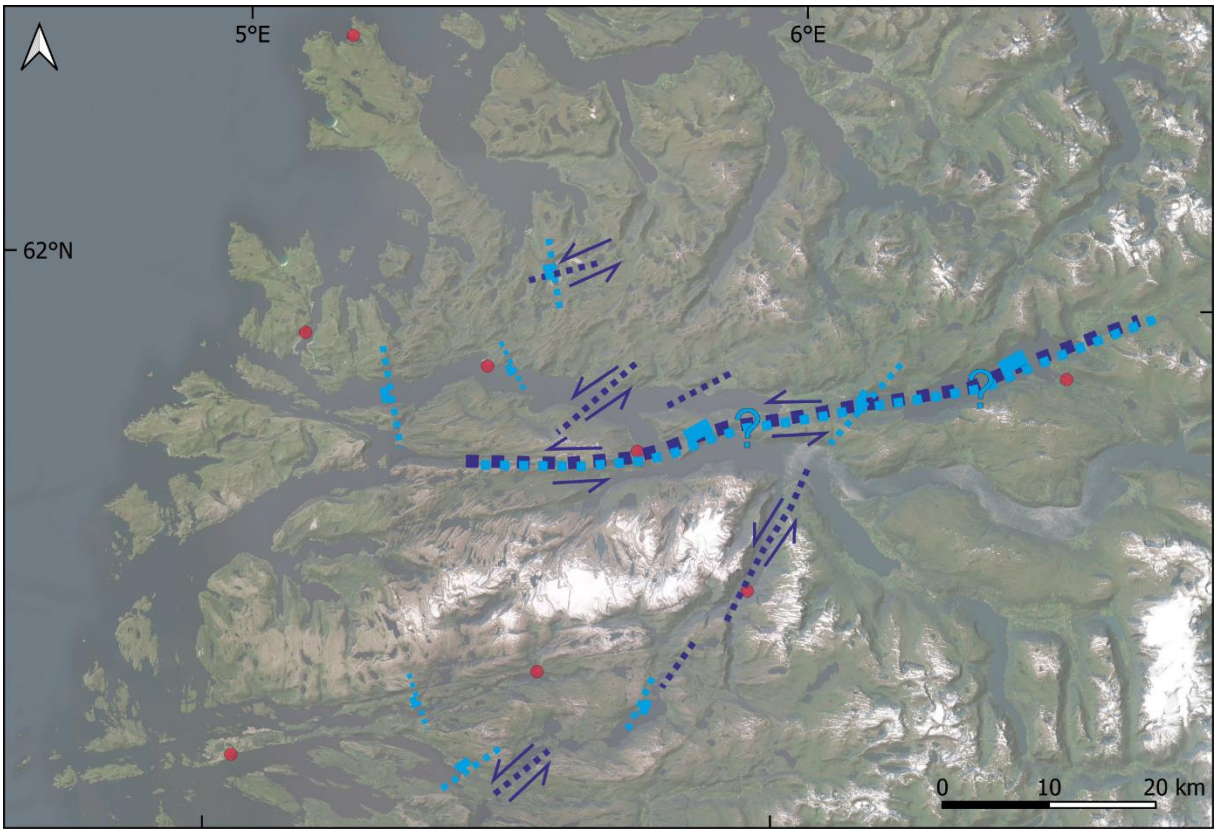

Figure 33: Simplified overview of tentative fault orientations extrapolated from field measurements and kinetic interpretations. ~N-S trending sinistral strike-slip kinematics are ignored for illustration purposes.

6 Conclusions

This study suggests a thermal history of the region consisting of a period of faster cooling (1.5-2°C/Ma) driven first by exhumation due to Devonian extension and then Permian-Triassic flexural rift plank uplift, followed by a period of slower cooling (0.2-0.4°C/Ma) from 250-150 Ma until present. Differences between the models have been explained by localized faulting during exhumation.

Apatite fission track ages do not show a correlation with sample elevation and are strongly offset in the study area, suggesting fault activity during Triassic-Cretaceous between samples.

Essentially, two main types of fractures have been observed in the study area. N-S-striking, mostly steeply west dipping fractures showed mainly normal dip-slip kinematics, closely followed by sinistral strike-slip kinematics. The second type are E-W to NE-SW striking fractures which show mainly sinistral kinematics, but some normal kinematics have been observed in the south of the study area. They show a less steep dip and are often parallel to the foliation and along older Devonian extensional structures. Whereas the N-S trending faults are assumed to have formed possibly as early as Late Devonian-Carboniferous, but mainly in relation to rifting in the North Sea, NE-SW and E-W trending structures parallel ductile

precursors, were most likely formed during Devonian extension. The latter are suggested to have been reactivated as normal or strike-slip faults.

Based on the kinematics a transtensional regime is suggested for the area. The difference to the offshore extensional regime is explained by the influence of old precursor structures and the weaker influence from the offshore rift. A model of localized normal faulting along preferential oriented structures and sinistral strike-slip kinematics along less preferential oriented precursor structures, the latter balancing and releasing stress built up by normal faulting and differential extension, is suggested for the study area during post-Caledonian.

The study stresses the importance of structural inheritance, influencing fault orientations and perturbing the regional stressfield locally, as has been suggested for the North Sea.

Lastly, it can be concluded that LAFT thermochronology has many advantages compared to the EDM method. The LAFT results obtained in this study seem to be reliable in comparison to other studies, but further methodological research is needed to proof trustworthiness of the method and to study influencing factors.

References

Bingen, B., Nordgulen, O., & Viola, G. (2008). A four-phase model for the Sveconorwegian orogeny, SW Scandinavia. *Norsk geologisk tidsskrift*, *88* (1), 43.

Braathen, A. (1999). Kinematics of post-Caledonian polyphase brittle faulting in the Sunnfjord region, western Norway. *Tectonophysics*, *302* (1-2), 99-121.

Cawood, P. A. (2005). Terra Australis Orogen: Rodinia breakup and development of the Pacific and Iapetus margins of Gondwana during the Neoproterozoic and Paleozoic *Earth-Science Reviews*, *69* (3-4), 249-279.

Cogné, N., Chew, D.M., Donelick, R.A. & Ansberque, C. (2020). LA-ICP-MS apatite fission track dating: a practical zeta-based approach. *Chemical Geology*, *531*, 119302.

Delvaux, D. & Sperner, B., (2003). New Aspects of Tectonic Stress Inversion with Reference to the TENSOR Program. *Geological Society Special Publication*, *212*, 75–100.

Donelick, R. A., O'Sullivan, P. B., & Ketcham, R. A. (2005). Apatite fission-track analysis. *Reviews in Mineralogy and Geochemistry*, *58* (1), 49-94.

Doré, A. G., Lundin, E. R., Jensen, L. N., Birkeland, Ø., Eliassen, P. E., & Fichler, C. (1999). Principal tectonic events in the evolution of the northwest European Atlantic margin. *Geological society London, petroleum geology conference series*, 5, 41-61.

Færseth, R. B. (1996). Interaction of Permo-Triassic and Jurassic extensional fault-blocks during the development of the northern North Sea. *Journal of the Geological Society*, *153* (6), 931-944.

Fossen, H. (1992). The role of extensional tectonics in the Caledonides of south Norway. *Journal of structural geology*, *14* (8-9), 1033-1046.

Fossen, H., & Dunlap, W. J. (1999). On the age and tectonic significance of Permo-Triassic dikes in the Bergen-Sunnhordland region, southwestern Norway. *Norsk geologisk tidsskrift*, *79* (3), 169-178.

Fossen, H. (2000). Extensional tectonics in the Caledonides: Synorogenic or postorogenic? *Tectonics*, *19* (2), 213-224.

Fossen, H. (2010a). Extensional tectonics in the North Atlantic Caledonides: a regional view. *Geological Society, London, Special Publications*, *335* (1), 767-793.

Fossen, H. (2010b). *Structural Geology*. Cambridge University Press. 190-192

Fossen, H., Khani, H. F., Faleide, J. I., Ksienzyk, A. K., & Dunlap, W. J. (2017). Post-Caledonian extension in the West Norway–northern North Sea region: the role of structural inheritance. *Geological Society, London, Special Publications*, *439* (1), 465-486.

Fossen, H., Ksienzyk, A. K., Rotevatn, A., Bauck, M. S., & Wemmer, K. (2021). From widespread faulting to localised rifting: Evidence from K-Ar fault gouge dates from the Norwegian North Sea rift shoulder. *Basin Research*, *33* (3), 1934-1953.

Gabrielsen, R. H., Faleide, J. I., Pascal, C., Braathen, A., Nystuen, J. P., Etzelmuller, B. & O'Donnell, S.(2010): Latest Caledonian to Present tectonomorphological development of southern Norway. *Marine and Petroleum Geology 27*, 709-723.

Gee, D. G., Fossen, H., Henriksen, N., & Higgins, A. K. (2008). From the early Paleozoic platforms of Baltica and Laurentia to the Caledonide Orogen of Scandinavia and Greenland. *Episodes Journal of International Geoscience*, *31* (1), 44-51.

Gleadow, A.J., Seiler, C. (2014). Fission Track Dating and Thermochronology. In: Rink, W., Thompson, J. (eds) *Encyclopedia of Scientific Dating Methods* (285-296). Springer, Dordrecht.

Gleadow, A., Kohn, B. & Seiler, C. (2019). The Future of Fission-Track Thermochronology. In: Malusà, M., Fitzgerald, P. (eds) *Fission-Track Thermochronology and its Application to Geology. Springer Textbooks in Earth Sciences, Geography and Environment* (77-92). Springer, Cham.

Green, P. F., Japsen, P., Bonow, J. M., Chalmers, J. A., Duddy, I. R., & Kukkonen, I. T. (2022). The post-Caledonian thermo-tectonic evolution of Fennoscandia. *Gondwana Research 107*, 201-234.

Guibaldo, C. N., Bordese, S., & Simoy, M. I. (2022). Results report of apatite fission-track analysis by LA-ICP-MS and its comparison with the conventional external detector method of dating. *Journal of Analytical Atomic Spectrometry*, *37* (2), 369-380.

Hacker, B. R., Andersen, T. B., Johnston, S., Kylander-Clark, A. R., Peterman, E. M., Walsh, E. O., & Young, D. (2010). High-temperature deformation during continental-margin subduction & exhumation: The ultrahigh-pressure Western Gneiss Region of Norway. *Tectonophysics*, *480* (1-4), 149-171.

Harrison, T.M., Célérier, J., Aikman, A.B., Hermann, J. & Heizler, M.T. (2009). Diffusion of 40Ar in muscovite. *Geochimica et Cosmochimica Acta 73* (4), 1039-1051.

Hestnes, Å., Gasser, D., Scheiber, T., Jacobs, J., van der Lelij, R., Schönenberger, J. & Ksienzyk, A.K. (2022). The brittle evolution of Western Norway – A space-time model based on fault mineralizations, K–Ar fault gouge dating and paleostress analysis. *Journal of Structural Geology 160,* 104621.

Howell, D., Griffin, W.L., Pearson, N.J., Powell, W., Wieland, P., & O'Reilly, S.Y. (2013). Trace element partitioning in mixed-habit diamonds. *Chemical Geology 355*, 134-143.

Hurford, A. J., & Green, P. F. (1982). A users' guide to fission track dating calibration. *Earth and Planetary Science Letters*, *59* (2), 343-354.

Hurford, A. J. (1990). Standardization of fission track dating calibration: Recommendation by the Fission Track Working Group of the IUGS Subcommission on Geochronology. *Chemical Geology: Isotope Geoscience Section*, *80* (2), 171-178.

Hurford, A.J. (2019). An Historical Perspective on Fission-Track Thermochronology. In: Malusà, M., Fitzgerald, P. (eds) *Fission-Track Thermochronology and its Application to Geology. Springer Textbooks in Earth Sciences, Geography and Environment* (3-23). Springer, Cham.

Jaffey, A. H., Flynn, K. F., Glendenin, L. E., Bentley, W. C., & Essling, A. M. (1971). Precision measurement of half-lives and specific activities of 235 U and 238 U. *Physical review C, 4* (5), 1889–1906.

Japsen, P.& Chalmers, J.A. (1999): Neogene uplift and tectonics around the North Atlantic: Overview. *Global and Planetary Change 24*, 165-173.

Johannessen, K. C., Kohlmann, F., Ksienzyk, A. K., Dunkl, I., & Jacobs, J. (2013). Tectonic evolution of the SW Norwegian passive margin based on low-temperature thermochronology from the innermost Hardangerfjord area. *Norwegian Journal of Geology*, *93*, 243-260.

Ketcham, R. A. (2005). Forward and inverse modeling of low-temperature thermochronometry data. *Reviews in mineralogy and geochemistry*, *58* (1), 275-314.

Ketcham, R. A., Carter, A., Donelick, R. A., Barbarand, J., & Hurford, A. J. (2007a). Improved measurement of fission-track annealing in apatite using c-axis projection. *American Mineralogist*, *92* (5-6), 789-798.

Ketcham, R. A., Carter, A., Donelick, R. A., Barbarand, J., & Hurford, A. J. (2007b). Improved modeling of fission-track annealing in apatite. *American Mineralogist*, *92* (5-6), 799-810.

Ketcham, R. A., Carter, A., & Hurford, A. J. (2015). Inter-laboratory comparison of fission track confined length and etch figure measurements in apatite. *American Mineralogist*, *100* (7), 1452-1468.

Ksienzyk, A. K., Dunkl, I., Jacobs, J., Fossen, H., & Kohlmann, F. (2014). From orogen to passive margin: constraints from fission track and (U–Th)/He analyses on Mesozoic uplift and fault reactivation in SW Norway. *Geological Society, London, Special Publications*, *390* (1), 679-702.

Ksienzyk, A. K., Wemmer, K., Jacobs, J., Fossen, H., Schomberg, A. C., Süssenberger, A., Lünsdorf, N. K. & Bastesen, E. (2016). Post-Caledonian brittle deformation in the Bergen area, West Norway: results from K–Ar illite fault gouge dating. *Norwegian Journal of Geology*, *96* (3), 275-299.

Labrousse, L., Jolivet, L., Andersen, T. B., Agard, P., Hébert, R., Maluski, H., & Scharer, U. (2004). Pressure-temperature-time deformation history of the exhumation of ultra-high pressure rocks in the Western Gneiss Region, Norway. *Geological Society of America Special Paper, 380*, 155-184.

Larsen, B. T., Olaussen, S., Sundvoll, B., & Heeremans, M. (2008). The Permo-Carboniferous Oslo Rift through six stages and 65 million years. *Episodes Journal of International Geoscience*, *31* (1), 52-58.

Lisker, F., Ventura, B., & Glasmacher, U. A. (2009). Apatite thermochronology in modern geology. *Geological Society, London, Special Publications*, *324* (1), 1-23.

Longerich, H. P., Jackson, S. E. & Gunther, D. (1996). Laser Ablation Inductively Coupled Plasma Mass Spectrometric Transient Signal Data Acquisition and Analyte Concentration Calculation. *Journal of Analytical Atomic Spectrometry*, *11* (9), 899 - 904.

McDowell, F.W., McIntosh, W.C. & Farley, K.A. (2005). A precise 40Ar–39Ar reference age for the Durango apatite (U–Th)/He and fission-track dating standard. *Chemical Geology, 214* (3-4), 249-263.

Nielsen, S. B., Gallagher, K., Leighton, C., Balling, N., Svenningsen, L., Jacobsen, B. H., Thomsen, E., Nielsen, O. B., Heilmann-Clausen, C., Egholm, D. L., Summerfield, M. A., Clausen, O. R., Piotrowski, J. A., Thorsen, M. R., Huuse, M., Abrahamsen, N., King, C. & Lykke-Andersen, H. (2009). The evolution of western Scandinavian topography: A review of Neogene uplift versus the ICE (isostasy–climate–erosion) hypothesis. *Journal of Geodynamics, 47*, 72-95.

Paton, C., Hellstrom, J., Paul, B.,Woodhead, J. & Hergt, J. (2011). Iolite: Freeware for the visualisation and processing of mass spectrometric data. *Journal of Analytical Atomic Spectrometry, 26*, 2508-2518.

Phillips, T. B., Fazlikhani, H., Gawthorpe, R. L., Fossen, H., Jackson, C. A. L., Bell, R. E., Faleide, J. I. & Rotevatn, A. (2019). The influence of structural inheritance and multiphase extension on rift development, the Northern North Sea. *Tectonics, 38* (12), 4099-4126.

Reeve, M.T., Bell, R.E., Duffy, O.B., Jackson, C.A.L. & Sansom, E. (2015). The growth of non-colinear normal fault systems; what can we learn from 3D seismic reflection data? *Journal of Structural Geology 70*, 141–155.

Redfield, T.F., Torsvik, T.H., Andriessen, P.A.M.M., Gabrielsen, R.H. (2004). Mesozoic and Cenozoic tectonics of the Møre Trøndelag Fault Complex, central Norway: constraints from new apatite fission track data. *Phys. Chem. Earth 29*, 673–682.

Redfield, T.F., Osmundsen, P.T. & Hendriks, B.W.H. (2005a). The role of fault reactivation and growth in the uplift of western Fennoscandia. *J. Geol. Soc. (London), 162*, 1013-1030.

Redfield, T.F., Braathen, A., Gabrielsen, R.H., Osmundsen, P.T., Torsvik, T.H., Andriessen, P.A.M., (2005b). Late Mesozoic to early Cenozoic components of vertical separation across the More-Trøndelag Fault Complex. Norway. *Tectonophys. 395*, 233-249.

Roberts, N. M., & Slagstad, T. (2015). Continental growth and reworking on the edge of the Columbia and Rodinia supercontinents; 1.86–0.9 Ga accretionary orogeny in southwest Fennoscandia. *International Geology Review, 57* (11-12), 1582-1606.

Rohrman, M., van der Beek, P., Andriessen, P., & Cloetingh, S. (1995). Meso-Cenozoic morphotectonic evolution of southern Norway: Neogene domal uplift inferred from apatite fission track thermochronology. *Tectonics, 14* (3), 704-718.

Sobel, E.R. & Seward, D. (2010). Influence of etching conditions on apatite fission-track etch pit diameter. *Chemical Geology, 271 (1-2),* 59-69.

Steer, P., Huismans, R. S., Valla, P. G., Gac, S. & Herman, F. (2012). Bimodal Plio-Quaternary glacial erosion of fjords and low-relief surfaces in Scandinavia. *Nature Geoscience, 5*, 635-639.

Tagami, T. & O'Sullivan, P. B. (2005). Fundamentals of Fission-Track Thermochronology. *Reviews in Mineralogy and Geochemistry*, *58* (1), 19–47

Vermeesch, P. (2018). IsoplotR: a free and open toolbox for geochronology. *Geoscience Frontiers, 9*, 1479-1493.

Wagner, G. A., Gleadow, A. J. W., & Fitzgerald, P. G. (1989). The significance of the partial annealing zone in apatite fission-track analysis: Projected track length measurements and uplift chronology of the Transantarctic Mountains. *Chemical Geology: Isotope Geoscience Section*, *79* (4), 295-305.

Walsh, E.O., Hacker, B.R., Gans, P.B., Wong, M.S. & Andersen, T.B. (2013). Crustal exhumation of the Western Gneiss Region UHP terrane, Norway: 40Ar/39Ar thermochronology and fault-slip analysis. *Tectonophysics*, *608*, 1159–1179.

Wiest, J.D., Jacobs, J., Fossen, H., Ganerød, M., & Osmundsen, P.T. (2021). Segmentation of the Caledonian orogenic infrastructure and exhumation of the Western Gneiss Region during transtensional collapse. *Journal of the Geological Society*, *178*, 1-23.

Young, D. J., Hacker, B. R., Andersen, T. B., & Gans, P. B. (2011). Structure and 40Ar/39Ar thermochronology of an ultrahigh-pressure transition in western Norway. *Journal of the Geological Society*, *168* (4), 887-898.

Basemap in Figures 1, 9, 11, 17, 21, 22 & 33: Esri Satellite, https://server.arcgisonline.com/ArcGIS/rest/services/World_Imagery/MapServer/tile/{z}/{y}/{x} (20.12.2022)

Appendix

A Length measurements

A1 Sample VAH_23

SD - Standard deviation. All measurements in [µm]. Type: T – TINT, C- TINCLE. Extracted from FastTracks: v3.3.4

Length Name	Length no.	Type	Apparent Length	Corrected Z Depth	True Length	Azimuth	Dip	Angle to C-Axis	Dpar Average	Dpar SD
Length01	1	T	9.69	0	9.69	79.28	0	79.28	1.22	0.21
Length01b	1	T	10.91	1.47	11.01	76.48	7.68	76.6	1.22	0.21
Length02	1	T	12.92	0	12.92	59.36	0	59.36	1.1	0.18
Length03	1	T	13.38	0.98	13.42	56.7	4.2	56.8	1.23	0.31
Length04	1	T	13.31	2.94	13.63	68.7	12.48	69.22	1.37	0.56
Length07	1	T	6.8	0.49	6.82	75.36	4.13	75.4	1.25	0.24
Length08	1	T	10.39	0	10.39	58.68	0	58.68	1.17	0.18
Length08c	1	T	8.31	0.98	8.36	68.92	6.74	69.07	1.17	0.18
Length08d	1	T	11.48	1.47	11.58	65.26	7.31	65.47	1.17	0.18
Length10	1	T	15.58	0	15.58	69.05	0	69.05	1.16	0.14
Length11	1	T	13.57	0	13.57	60.81	0	60.81	1.12	0.11
Length12	1	T	14.28	1.47	14.36	37.52	5.89	37.91	1.09	0.19
Length15	1	T	11.48	0.49	11.49	65.33	2.45	65.36	1.15	0.13
Length17b	1	T	13.01	0.49	13.01	79.73	2.16	79.74	1.16	0.1
Length18	1	T	10.81	0.49	10.82	64.56	2.6	64.59	1.43	0.25
Length18	2	T	10.48	0.98	10.52	70.55	5.35	70.64	1.43	0.25
Length18b	1	T	9.26	0	9.26	63.87	0	63.87	1.43	0.25
Length19	1	T	11.75	0.98	11.79	36.2	4.77	36.47	1.02	0.26
Length21	1	T	10.11	2.45	10.41	72.24	13.64	72.76	1.17	0.25
Length21b	1	T	11.94	0.98	11.98	28.05	4.7	28.41	1.17	0.25
Length27b	1	T	11.64	1.96	11.8	36.98	9.58	38.03	1.05	0.36
Length29b	1	T	8.3	0.98	8.35	47.71	6.75	48.07	0.96	0.29
Length30	1	T	10.7	1.47	10.8	71.64	7.83	71.82	1.2	0.25
Length30	2	T	6.42	0.49	6.44	79.7	4.37	79.73	1.2	0.25
Length30b	1	T	12.79	1.96	12.94	54.89	8.72	55.35	1.2	0.25
Length34	1	T	12.92	1.96	13.07	49.04	8.64	49.6	1.08	0.17
Length36b	1	T	12.87	0	12.87	44.57	0	44.57	1.14	0.3
Length36c	1	T	11.29	0.98	11.33	86.91	4.97	86.92	1.14	0.3

A2 Sample VAH_26

SD - Standard deviation. No. – number. All measurements in [µm]. Type: T – TINT, C- TINCLE. Extracted from FastTracks: v3.3.4

Length Name	Length No.	Type	Apparent Length	Corrected Z Depth	True Length	Azimuth	Dip	Angle to C-Axis	Dpar Average	Dpar SD
Length02	1	T	12.57	0	12.57	32.62	0	32.62	1.16	0.22
Length02	2	T	13.81	0.49	13.82	9.17	2.04	9.39	1.16	0.22
Length02	3	T	10.74	1.47	10.84	61.73	7.8	62.02	1.16	0.22
Length03	1	T	11.96	0	11.96	65.94	0	65.94	1.03	0.14
Length05b	1	T	11.08	1.47	11.18	52.07	7.57	52.46	1.15	0.18
Length05c	1	T	8.07	1.96	8.3	41.08	13.68	42.91	1.15	0.18
Length06	1	C	13.7	0.49	13.71	70.07	2.05	70.08	1.3	0.25
Length06b	1	T	13.74	2.45	13.96	31.96	10.13	33.37	1.3	0.25
Length06b	2	T	9.18	4.42	10.18	61.32	25.7	64.38	1.3	0.25
Length06c	1	T	12.73	1.96	12.88	33.98	8.77	34.96	1.3	0.25
Length06c	2	T	12.09	1.47	12.18	71.68	6.94	71.82	1.3	0.25
Length06d	1	T	10	2.45	10.3	81.68	13.79	81.92	1.3	0.25
Length08b	1	T	11.54	2.45	11.8	79.39	12	79.62	0.92	0.14
Length10	1	C	12.62	1.47	12.7	81.12	6.66	81.18	1.13	0.25
Length10b	1	C	11.93	2.45	12.18	82.91	11.63	83.06	1.13	0.25
Length10c	1	C	11.34	0.49	11.35	58.55	2.48	58.58	1.13	0.25
Length10d	1	T	10.76	0.49	10.77	88.26	2.61	88.26	1.13	0.25
Length10d	2	T	10.66	2.45	10.94	44.67	12.97	46.13	1.13	0.25
Length11	1	T	11.98	0	11.98	54.06	0	54.06	1.24	0.2
Length11b	1	T	6.38	1.47	6.55	27.06	13	29.81	1.24	0.2
Length11b	2	T	10.5	1.96	10.68	53.56	10.6	54.28	1.24	0.2
Length11c	1	T	9.69	0	9.69	50	0	50	1.24	0.2
Length11d	1	T	9.52	0.49	9.53	46.82	2.95	46.89	1.24	0.2
Length11e	1	T	14.24	0.98	14.27	47.36	3.94	47.48	1.24	0.2
Length11f	1	T	9.61	0	9.61	53.92	0	53.92	1.24	0.2
Length11g	1	T	11.3	1.96	11.47	86.55	9.86	86.6	1.24	0.2
Length12	1	T	10.35	0.49	10.37	67.07	2.71	67.09	1.23	0.13
Length13	1	T	14.41	0	14.41	46.88	0	46.88	1.19	0.15
Length13b	1	T	9.95	0	9.95	43.69	0	43.69	1.19	0.15
Length13c	1	T	12.39	0	12.39	65.42	0	65.42	1.19	0.15
Length14	1	C	13.44	1.47	13.52	73.5	6.25	73.6	1.13	0.2
Length15	1	C	12.45	0	12.45	20.77	0	20.77	0.99	0.4
Length16b	1	T	12.13	0.49	12.14	53.91	2.32	53.95	1.15	0.21
Length16c	1	T	13.59	0.49	13.6	77.33	2.07	77.33	1.15	0.21
Length17	1	T	12.11	1.47	12.2	58.93	6.93	59.18	1.14	0.11
Length18	1	C	13.82	1.47	13.9	68.34	6.08	68.47	1	0.15

A3 Sample VAH_31

SD - Standard deviation. No. – number. All measurements in [µm]. Type: T – TINT, C- TINCLE. Extracted from FastTracks: v3.3.4

Length Name	Length No.	Type	Apparent Length	Corrected Z Depth	True Length	Azimuth	Dip	Angle to C-Axis	Dpar Average	Dpar SD
Length03b	1	C	12.39	1.47	12.47	58.45	6.78	58.69	1.13	0.23
Length04d	1	T	12.58	1.96	12.73	83.96	8.87	84.03	1.09	0.17
Length05	1	T	11.33	0.98	11.37	30.41	4.95	30.77	0.99	0.15
Length09	1	C	15.09	0	15.09	13.06	0	13.06	1.08	0.28
Length10	1	C	6.06	0	6.06	82.57	0	82.57	0.98	0.11
Length12	1	C	10.48	1.96	10.66	71.09	10.61	71.43	1.02	0.13
Length12b	1	C	10.62	0.49	10.63	67.26	2.65	67.28	1.02	0.13
Length12d	1	C	5.96	0	5.96	80.29	0	80.29	1.02	0.13
Length13	1	C	13.85	2.45	14.07	38.34	10.05	39.44	0.9	0.13
Length14b	1	T	8.69	0.49	8.7	38.38	3.23	38.49	1	0.08
Length14c	1	C	11.82	0	11.82	25.13	0	25.13	1	0.08

A4 Sample VAH_42

SD - Standard deviation. No. – number. All measurements in [µm]. Type: T – TINT, C- TINCLE. Extracted from FastTracks: v3.3.4

Length Name	Length No.	Type	Apparent Length	Corrected Z Depth	True Length	Azimuth	Dip	Angle to C-Axis	Dpar Average	Dpar SD
Length01	1	T	10.7	1.96	10.87	77.67	10.4	77.88	1.3	0.11
Length01b	1	T	11.55	0.98	11.59	35.81	4.86	36.09	1.3	0.11
Length01c	1	T	10.72	0.98	10.77	70.11	5.23	70.2	1.3	0.11
Length02	1	T	9.82	0.49	9.83	54.31	2.86	54.37	1.48	0.29
Length02	2	T	13.01	1.96	13.15	75.05	8.58	75.22	1.48	0.29
Length02b	1	T	12.34	0.49	12.35	40.59	2.28	40.64	1.48	0.29
Length02c	1	T	8.37	0.49	8.38	77.43	3.36	77.45	1.48	0.29
Length03	1	T	10.37	0.49	10.38	71.41	2.71	71.43	1.35	0.18
Length03	2	T	13.65	1.96	13.79	33.88	8.18	34.74	1.35	0.18
Length03	3	T	7.16	0.49	7.17	83.25	3.92	83.26	1.35	0.18
Length03b	1	T	8.67	0.49	8.68	65.03	3.24	65.07	1.35	0.18
Length03c	1	T	14.36	2.45	14.57	49.78	9.7	50.47	1.35	0.18
Length03d	1	T	8.18	0	8.18	80.19	0	80.19	1.35	0.18
Length04	1	T	12.92	1.96	13.06	70.13	8.64	70.36	1.36	0.29
Length05	1	T	11.87	1.96	12.03	79.03	9.39	79.18	1.26	0.09
Length05	2	T	13.15	0.49	13.16	62.91	2.14	62.93	1.26	0.09
Length05b	1	T	11.19	0	11.19	14.25	0	14.25	1.26	0.09
Length06	1	T	12.65	0	12.65	80.46	0	80.46	1.32	0.1
Length06	2	T	11.57	1.47	11.66	51.25	7.26	51.62	1.32	0.1
Length09	1	T	10.08	0.49	10.1	67.5	2.79	67.53	1.31	0.17
Length09b	1	T	13.09	1.47	13.18	60.24	6.42	60.45	1.31	0.17
Length09c	1	T	13.67	0.98	13.7	39.45	4.11	39.63	1.31	0.17
Length09c	2	T	14.33	0.98	14.36	20.49	3.92	20.84	1.31	0.17
Length09c	3	T	10.53	0.49	10.54	52.47	2.67	52.52	1.31	0.17
Length09d	1	T	13.51	0.98	13.55	39.94	4.16	40.12	1.31	0.17
Length09d	2	T	10.42	0.49	10.43	53.36	2.7	53.41	1.31	0.17
Length09d	3	T	6.99	0.49	7.01	21.63	4.01	21.98	1.31	0.17
Length10	1	T	9.86	2.45	10.16	75.14	13.98	75.59	1.26	0.14
Length10b	1	T	10.45	0.98	10.5	32.39	5.36	32.78	1.29	0.14
Length10c	1	T	7.53	1.96	7.78	76.25	14.62	76.7	1.26	0.14
Length10d	1	T	11.75	3.93	12.39	70.07	18.48	71.13	1.26	0.14
Length11	1	T	13.35	0.49	13.36	35.39	2.11	35.44	1.33	0.23
Length11b	1	T	12.87	0.49	12.88	72.76	2.18	72.77	1.33	0.23
Length11b	2	T	13.09	1.96	13.24	76.46	8.53	76.61	1.33	0.23
Length11b	3	T	10.55	1.96	10.73	35.65	10.54	36.98	1.33	0.23
Length12	1	T	10.77	2.94	11.17	65.34	15.29	66.26	1.41	0.2
Length13	1	T	11.73	1.47	11.83	56.16	7.15	56.46	1.4	0.41
Length13	2	T	11.63	0.49	11.64	18	2.42	18.16	1.4	0.41

Length13	3	T	13.23	0	13.23	34.07	0	34.07	1.4	0.41
Length14d	1	T	10.63	1.47	10.73	82.62	7.88	82.69	1.43	0.23
Length14e	1	T	10.61	2.94	11.01	62.9	15.51	63.97	1.43	0.23
Length14f	1	T	12.4	0.49	12.41	34.76	2.27	34.82	1.43	0.23
Length15	1	T	12.6	0	12.6	71.63	0	71.63	1.5	0.18
Length15b	1	T	13.84	0.49	13.85	17.02	2.03	17.14	1.5	0.18
Length15c	1	T	9.05	0.98	9.11	69.88	6.19	70	1.5	0.18
Length15c	2	T	12.87	2.94	13.2	44.07	12.89	45.54	1.5	0.18
Length16	1	T	11.86	1.96	12.02	46.94	9.4	47.66	1.42	0.3
Length18	1	T	11.8	0	11.8	55.99	0	55.99	1.39	0.12
Length18	2	T	11.9	0	11.9	88.73	0	88.73	1.39	0.12
Length19	1	T	12.47	0.98	12.51	44.01	4.5	44.2	1.3	0.27
Length19b	1	T	12.59	0.49	12.6	48.52	2.23	48.55	1.3	0.27
Length19b	2	T	11.92	0.98	11.96	70.12	4.71	70.19	1.3	0.27
Length19c	1	T	12.14	0.98	12.18	70.69	4.62	70.76	1.3	0.27
Length20	1	T	13.62	0	13.62	19.45	0	19.45	1.47	0.18
Length20b	1	T	11.58	0	11.58	37.69	0	37.69	1.47	0.18
Length20c	1	T	11.41	0	11.41	63.96	0	63.96	1.47	0.18
Length20d	1	T	10.27	1.96	10.45	83.46	10.82	83.58	1.47	0.18
Length21	1	T	11.27	0.49	11.28	21.23	2.49	21.37	1.47	0.06
Length22b	1	T	10.69	0	10.69	66.91	0	66.91	1.44	0.31
Length22c	1	T	11.32	0.49	11.34	63.78	2.48	63.81	1.44	0.31
Length23	1	T	12.33	0.98	12.37	78.61	4.55	78.65	1.58	0.14
Length25	1	T	14.03	0.98	14.07	51.32	4	51.43	1.47	0.23
Length25	2	T	11.62	0.98	11.66	11.75	4.83	12.69	1.47	0.23
Length25b	1	T	12.85	0	12.85	60.26	0	60.26	1.47	0.23
Length25d	1	T	11.84	0.98	11.88	66.69	4.74	66.77	1.47	0.23
Length25d	2	T	14.39	0.49	14.4	51.69	1.95	51.72	1.47	0.23
Length25e	1	T	11.24	0.49	11.25	48.94	2.5	48.98	1.47	0.23
Length25f	1	T	13.95	0.98	13.98	13.26	4.03	13.85	1.47	0.23
Length25g	1	T	12.71	2.94	13.05	59.37	13.05	60.24	1.47	0.23
Length26b	1	T	12.72	0.98	12.76	68.06	4.41	68.13	1.41	0.17
Length31	1	T	11.79	1.96	11.96	64.44	9.45	64.82	1.37	0.15
Length31b	1	T	13.34	0.49	13.35	36.19	2.11	36.24	1.37	0.15
Length32	1	T	10.38	1.47	10.48	53.23	8.08	53.65	1.49	0.15
Length33	1	T	11.87	1.47	11.96	39.34	7.07	39.87	1.47	0.11
Length33b	1	T	12.24	2.45	12.49	77.98	11.33	78.22	1.47	0.11
Length34	1	T	14.04	1.47	14.12	3.73	5.99	7.05	1.49	0.14
Length35	1	T	12.87	1.47	12.96	79.66	6.53	79.73	1.4	0.21
Length35	2	T	12.09	1.47	12.18	35.56	6.94	36.14	1.4	0.21
Length35b	1	T	13.99	1.96	14.12	59.44	7.99	59.77	1.4	0.21
Length35c	1	T	10.89	0	10.89	36.92	0	36.92	1.4	0.21
Length36	1	T	9.9	1.47	10.01	45.1	8.46	45.71	1.38	0.11
Length37	1	T	11.18	0.49	11.19	63.21	2.51	63.24	1.5	0.14
Length37	2	T	11.85	0.98	11.9	31.59	4.73	31.9	1.5	0.14

Length38	1	T	14.54	2.45	14.75	75.31	9.58	75.52	1.33	0.09
Length39	1	T	11.6	0.49	11.61	65.93	2.42	65.95	1.48	0.18
Length39	2	T	13.53	1.47	13.61	61.94	6.21	62.12	1.48	0.18
Length39c	1	T	13.16	0	13.16	62.04	0	62.04	1.48	0.18
Length39e	1	T	9.92	0.98	9.97	83.38	5.65	83.41	1.48	0.18
Length40	1	T	12.03	1.96	12.18	55.08	9.27	55.6	1.36	0.09
Length41	1	T	13.53	0.98	13.57	26.5	4.15	26.8	1.37	0.26
Length41	2	T	12.09	2.45	12.34	21.6	11.47	24.32	1.37	0.26
Length41b	1	T	13.59	0	13.59	26.76	0	26.76	1.37	0.26
Length42	1	T	10.02	0.49	10.03	56.04	2.8	56.08	1.05	0.16
Length43	1	T	11.96	1.47	12.05	58.57	7.02	58.83	1.4	0.54
Length45	1	T	13.67	0.98	13.71	67.43	4.11	67.5	1.38	0.36
Length47	1	T	12.4	0.98	12.44	49.61	4.53	49.77	1.46	0.13
Length47b	1	T	11.34	1.47	11.43	82.9	7.4	82.96	1.46	0.13
Length48	1	T	11.45	1.96	11.62	49.08	9.73	49.8	1.48	0.22
Length48b	1	T	11.82	0.98	11.86	17.32	4.75	17.94	1.48	0.22
Length50	1	T	11.9	0.49	11.91	32.66	2.36	32.74	1.45	0.28

A5 Sample MLM_134

SD - Standard deviation. No. – number. All measurements in [µm]. Type: T – TINT, C- TINCLE. Extracted from FastTracks: v3.3.4

Length Name	Length No.	Type	Apparent Length	Corrected Z Depth	True Length	Azimuth	Dip	Angle to C-Axis	Dpar Average	Dpar SD
Length01	1	T	9.75	2.45	10.06	49.67	14.12	51.13	1.41	0.15
Length01b	1	T	13.27	1.47	13.35	45.39	6.33	45.73	1.41	0.15
Length01c	1	T	12.82	4.42	13.56	49.08	19.01	51.74	1.41	0.15
Length02	1	T	13.13	0.49	13.14	52.81	2.14	52.84	1.41	0.1
Length02	2	T	13.23	1.47	13.31	39.83	6.35	40.25	1.41	0.1
Length02	3	T	12.85	2.94	13.19	74.59	12.91	74.99	1.41	0.1
Length02	4	T	9.05	0	9.05	44.15	0	44.15	1.41	0.1
Length02	5	T	13.39	0	13.39	52.43	0	52.43	1.41	0.1
Length02b	1	T	11.69	0.49	11.7	53.98	2.4	54.02	1.41	0.1
Length02b	2	T	14.07	0.49	14.08	43.24	2	43.28	1.41	0.1
Length02b	3	T	9.51	0.49	9.52	23.28	2.95	23.45	1.41	0.1
Length02c	1	T	11.78	0.98	11.82	53.86	4.76	54.01	1.41	0.1
Length02d	1	T	14.8	0.98	14.83	50.07	3.8	50.18	1.41	0.1
Length02d	2	T	13.29	0.98	13.32	54.7	4.23	54.81	1.41	0.1
Length02e	1	T	11.94	2.45	12.19	23.23	11.62	25.83	1.41	0.1
Length02f	1	T	12.25	0.49	12.26	79.98	2.29	79.99	1.41	0.1
Length02h	1	T	13.05	0	13.05	27.98	0	27.98	1.41	0.1
Length02h	2	T	12.02	0.49	12.03	24.38	2.34	24.49	1.41	0.1
Length03	1	T	10.8	0.49	10.81	38.55	2.6	38.63	1.16	0.2
Length04	1	T	14.04	0.98	14.07	87.74	4	87.75	1.25	0.13
Length04b	1	T	12.25	0	12.25	44.82	0	44.82	1.25	0.13
Length04c	1	T	11.72	1.47	11.81	79.7	7.16	79.78	1.25	0.13
Length04c	2	T	10.56	2.45	10.84	29.28	13.08	31.84	1.25	0.13
Length04d	1	T	9.21	0.49	9.22	75.89	3.05	75.91	1.25	0.13
Length05	1	T	12.87	0.98	12.91	34.23	4.36	34.47	1.21	0.11
Length05b	1	T	13.29	0.98	13.32	53.08	4.22	53.2	1.21	0.11
Length05b	2	T	7.23	0	7.23	69.66	0	69.66	1.21	0.11
Length05c	1	T	11.21	0.98	11.25	80.54	5.01	80.57	1.21	0.11
Length05d	1	T	8.7	1.96	8.91	86.97	12.72	87.04	1.21	0.11
Length05e	1	T	12.29	0	12.29	74.77	0	74.77	1.21	0.11
Length05f	1	T	12.73	0.98	12.77	56.24	4.41	56.35	1.21	0.11
Length06	1	T	14.29	0	14.29	30.34	0	30.34	1.24	0.09
Length06	2	T	10.88	1.96	11.06	33.57	10.23	34.92	1.24	0.09
Length06b	1	T	12.32	0	12.32	49.31	0	49.31	1.24	0.09
Length06b	2	T	11.88	1.96	12.04	65.78	9.38	66.13	1.24	0.09
Length06b	3	T	13.45	3.44	13.89	62.69	14.33	63.61	1.24	0.09
Length06c	1	T	11.01	0.49	11.03	65.35	2.55	65.38	1.24	0.09
Length06d	1	T	12.13	1.96	12.29	85.78	9.2	85.83	1.24	0.09

Length07	1	T	13.53	0.98	13.56	82.95	4.15	82.96	1.64	0.16
Length08	1	T	13.76	0.49	13.77	26.96	2.04	27.03	1.43	0.12
Length08b	1	T	14.98	1.96	15.11	64.38	7.46	64.62	1.43	0.12
Length08b	2	T	12.33	0.98	12.37	69.24	4.55	69.3	1.43	0.12
Length08c	1	T	12.91	0.49	12.92	47.72	2.18	47.76	1.43	0.12
Length08c	2	T	12.35	0.49	12.36	20.59	2.28	20.71	1.43	0.12
Length08d	1	T	11.65	0.49	11.66	61.31	2.41	61.34	1.43	0.12
Length08d	2	T	12.44	0	12.44	20.47	0	20.47	1.43	0.12
Length08d	3	T	12.01	3.93	12.63	47.66	18.11	50.19	1.43	0.12
Length08e	1	T	15.49	0.49	15.49	73.87	1.82	73.87	1.43	0.12
Length08e	2	T	9.19	0.49	9.2	64.34	3.06	64.38	1.43	0.12
Length08f	1	T	12.37	0.49	12.38	68.87	2.27	68.89	1.43	0.12
Length08g	1	T	13.66	3.44	14.08	42.73	14.12	44.58	1.43	0.12
Length09	1	T	12.75	2.45	12.99	15.89	10.89	19.18	1.47	0.14
Length09b	1	T	12.45	1.96	12.6	65.94	8.96	66.25	1.47	0.14
Length09b	2	T	12.87	0	12.87	11.18	0	11.18	1.47	0.14
Length09c	1	T	11.31	1.96	11.48	72.08	9.84	72.36	1.47	0.14
Length09d	1	T	11.92	0.98	11.96	24.34	4.71	24.77	1.47	0.14
Length09d	2	T	6.48	0	6.48	60.31	0	60.31	1.47	0.14
Length09e	1	T	12.13	0.98	12.17	36.79	4.63	37.04	1.47	0.14
Length10	1	T	13.22	0.98	13.26	46.6	4.25	46.75	1.48	0.22
Length10	2	T	9.66	1.47	9.77	52.26	8.67	52.76	1.48	0.22
Length10b	1	T	11.75	0	11.75	82.71	0	82.71	1.48	0.22
Length10c	1	T	12.13	2.45	12.38	76.58	11.43	76.85	1.48	0.22
Length10c	2	T	13.05	0	13.05	38.66	0	38.66	1.48	0.22
Length10d	1	T	13.68	1.96	13.82	82.47	8.17	82.55	1.48	0.22
Length10d	2	T	9.74	0.98	9.79	51.73	5.75	51.96	1.48	0.22
Length10e	1	T	12.86	1.47	12.94	46.02	6.53	46.38	1.48	0.22
Length10f	1	T	13	0.98	13.03	37.83	4.32	38.04	1.48	0.22
Length10g	1	T	11.31	1.96	11.48	47.31	9.84	48.09	1.48	0.22
Length10h	1	T	12.61	0	12.61	50.59	0	50.59	1.48	0.22
Length11	1	T	14.81	1.47	14.88	70.81	5.68	70.91	1.35	0.11
Length11b	1	T	14.01	1.47	14.09	24.69	6	25.37	1.35	0.11
Length11e	1	T	11.08	0	11.08	70.1	0	70.1	1.35	0.11
Length11f	1	T	14.09	2.94	14.39	38.66	11.81	40.15	1.35	0.11
Length12	1	T	11.98	0	11.98	68.75	0	68.75	1.37	0.21
Length12b	1	T	11.34	0.98	11.38	77.05	4.95	77.1	1.37	0.21
Length12b	2	T	11.32	2.45	11.58	36.07	12.23	37.82	1.37	0.21
Length13	1	T	11.71	1.96	11.88	72.11	9.51	72.37	1.34	0.09
Length13b	1	T	13.57	0.49	13.57	31.7	2.07	31.76	1.34	0.09
Length14	1	T	12.64	0	12.64	46.45	0	46.45	1.44	0.19
Length14	2	T	12.6	1.47	12.69	73.22	6.66	73.34	1.44	0.19
Length14	3	T	12.96	0.98	12.99	27.88	4.33	28.18	1.44	0.19
Length14	4	T	9.42	0.49	9.44	37.35	2.98	37.45	1.44	0.19
Length14b	1	T	12.83	0	12.83	73.59	0	73.59	1.44	0.19

Length14b	2	T	13.43	2.94	13.75	80.54	12.37	80.76	1.44	0.19
Length14c	1	T	15.16	0	15.16	30.86	0	30.86	1.44	0.19
Length14c	2	T	13.29	0.49	13.3	58.05	2.11	58.08	1.44	0.19
Length14c	3	T	13.98	3.93	14.52	58.74	15.69	60.03	1.44	0.19
Length14d	1	T	13.82	1.47	13.9	51.16	6.08	51.42	1.44	0.19
Length14d	2	T	12.27	1.47	12.36	11.91	6.84	13.71	1.44	0.19
Length14e	1	T	14.26	1.47	14.34	87.7	5.89	87.71	1.44	0.19
Length14f	1	T	12.45	1.96	12.61	51.09	8.96	51.66	1.44	0.19
Length14f	2	T	11.67	2.45	11.92	58.2	11.88	58.95	1.44	0.19
Length15	1	T	11.73	0	11.73	65.37	0	65.37	1.15	0.18
Length15b	1	T	13.55	0.98	13.59	38.86	4.14	39.05	1.15	0.18
Length16	1	T	10.99	0.49	11.01	28.59	2.56	28.7	1.47	0.12
Length16b	1	T	10.44	1.47	10.55	50.38	8.02	50.84	1.47	0.12
Length16c	1	T	13.37	1.47	13.45	11.19	6.29	12.82	1.47	0.12
Length17	1	T	13.13	1.47	13.21	65.92	6.4	66.08	1.59	0.09
Length17d	1	T	12.49	1.96	12.65	15.99	8.93	18.26	1.59	0.09
Length18	1	T	11.34	0.49	11.35	54.42	2.48	54.45	1.23	0.13
Length20	1	T	13.25	3.44	13.68	60.07	14.54	61.12	1.44	0.08
Length21	1	T	12.96	3.44	13.4	64.08	14.85	65	1.37	0.09
Length21b	1	T	12.38	0.98	12.42	56.63	4.53	56.75	1.37	0.09
Length21b	2	T	8.8	1.47	8.93	23.84	9.49	25.55	1.37	0.09
Length21c	1	T	13.61	0.98	13.65	25.05	4.12	25.36	1.37	0.09
Length22	1	T	11.1	0.49	11.11	47.88	2.53	47.93	1.41	0.07
Length23	1	T	12.25	0.49	12.26	44.25	2.29	44.3	1.3	0.14
Length23b	1	T	9.79	1.47	9.9	59.27	8.55	59.65	1.3	0.14
Length24b	1	T	6.49	1.47	6.66	36.13	12.77	38.03	1.37	0.16
Length25	1	T	12.25	1.47	12.34	63.97	6.85	64.17	1.2	0.12
Length25b	1	T	12.87	0.49	12.88	43.58	2.18	43.62	1.2	0.12
Length25c	1	T	12.96	0.49	12.97	73.43	2.17	73.44	1.2	0.12
Length25d	1	T	12.63	0.49	12.64	53.64	2.23	53.67	1.2	0.12
Length25e	1	T	14.27	2.45	14.48	65.08	9.76	65.46	1.2	0.12
Length25f	1	T	9.93	1.47	10.04	70.68	8.43	70.9	1.2	0.12
Length26	1	T	12.3	0	12.3	70.79	0	70.79	1.26	0.12
Length26b	1	T	12.68	0.49	12.69	58.37	2.22	58.39	1.26	0.12
Length26c	1	T	11.54	0.49	11.55	85.53	2.44	85.53	1.26	0.12
Length26g	1	T	11.76	0.49	11.77	48.99	2.39	49.03	1.26	0.12
Length26i	1	T	13.27	0	13.27	54.08	0	54.08	1.26	0.12

A6 Sample VAH_48

SD - Standard deviation. No. – number. All measurements in [µm]. Type: T – TINT, C- TINCLE. Extracted from FastTracks: v3.3.4

Length Name	Length No.	Type	Apparent Length	Corrected Z Depth	True Length	Azimuth	Dip	Angle to C-Axis	Dpar Average	Dpar SD
Length06b	1	T	12.23	0	12.23	49.84	0	49.84	1	0.28
Length08	1	T	5.57	0	5.57	38.71	0	38.71	1.11	0.14
Length09	1	T	9.97	2.45	10.27	76.18	13.82	76.59	1.12	0.14
Length14	1	T	7.18	0.49	7.2	71.55	3.91	71.6	1.06	0.11
Length17	1	T	12	1.96	12.16	81.79	9.29	81.9	1.15	0.16
Length18	1	T	10.99	0.49	11.01	27.15	2.56	27.26	1.06	0.12
Length19	1	T	13.01	2.94	13.34	75.56	12.75	75.92	1.07	0.16
Length20b	1	T	14.56	2.45	14.77	36.42	9.56	37.49	1.19	0.18
Length23	1	T	11.91	0	11.91	52.48	0	52.48	1.05	0.18
Length23b	1	T	11.6	0.49	11.61	34.34	2.42	34.41	1.05	0.18
Length24	1	T	11.73	0.49	11.74	71.98	2.4	71.99	1	0.17
Length25	1	T	10.32	0	10.32	61.7	0	61.7	1.12	0.17
Length26	1	T	7.03	0	7.03	36.78	0	36.78	1.04	0.08
Length27	1	T	6	0.98	6.08	61.34	9.3	61.75	1.04	0.06
Length29	1	T	13.86	0	13.86	72.94	0	72.94	0.98	0.14

A7 Sample VAH_44-2

SD - Standard deviation. No. – number. All measurements in [µm]. Type: T – TINT, C- TINCLE. Extracted from FastTracks: v3.3.4

Length Name	Length No.	Type	Apparent Length	Corrected Z Depth	True Length	Azimuth	Dip	Angle to C-Axis	Dpar Average	Dpar SD
Length01	1	T	12.11	0.49	12.12	65.87	2.32	65.89	1.71	0.27
Length01	2	T	11.84	0.98	11.88	42.96	4.74	43.17	1.71	0.27
Length01	3	T	13.73	0.49	13.74	22.39	2.05	22.48	1.71	0.27
Length01b	1	T	13.18	0.49	13.19	52.16	2.13	52.19	1.71	0.27
Length01c	1	T	14.5	2.45	14.71	23.17	9.6	24.98	1.71	0.27
Length01d	1	T	11.57	0	11.57	86.44	0	86.44	1.71	0.27
Length01e	1	T	12.84	0.98	12.88	81.91	4.37	81.93	1.71	0.27
Length01f	1	T	13.08	0	13.08	46.41	0	46.41	1.71	0.27
Length01g	1	T	14.12	1.47	14.2	23.51	5.95	24.21	1.71	0.27
Length01h	1	T	10.35	2.94	10.76	77.33	15.88	77.82	1.71	0.27
Length02	1	T	11.3	0.98	11.34	58.42	4.96	58.55	1.63	0.15
Length03	1	T	13.7	1.47	13.78	46.76	6.14	47.07	1.55	0.22
Length04	1	T	13.3	0.98	13.33	51.49	4.22	51.61	1.83	0.2
Length04	2	T	11.58	3.93	12.23	54.05	18.73	56.22	1.83	0.2
Length05	1	T	14.87	0.98	14.9	51.21	3.78	51.31	1.54	0.4
Length06	1	T	13.17	0.49	13.18	76.92	2.13	76.93	1.42	0.17
Length07	1	T	12.65	0.49	12.66	80.13	2.22	80.14	1.38	0.05
Length08	1	T	13.86	0.98	13.9	50.81	4.05	50.93	1.82	0.17
Length08d	1	T	13.11	0.49	13.12	43.56	2.14	43.6	1.82	0.17
Length09	1	T	12.79	0.49	12.8	38.66	2.2	38.72	1.63	0.33
Length11	1	T	13.18	0.49	13.19	37.43	2.13	37.48	1.57	0.2
Length11	2	T	11.68	2.45	11.94	40.43	11.86	41.84	1.57	0.2
Length11b	1	T	13.89	0.49	13.9	36.5	2.02	36.55	1.57	0.2
Length11c	1	T	13.51	0.49	13.52	53.47	2.08	53.5	1.57	0.2
Length12	1	T	12.7	0.98	12.73	56.62	4.42	56.73	1.47	0.11
Length13	1	T	11.54	1.96	11.71	61.52	9.65	61.96	1.92	0.18
Length13b	1	T	13.45	2.45	13.67	62.57	10.34	63.05	1.92	0.18
Length14	1	T	10.92	0.49	10.93	76.46	2.57	76.48	1.64	0.08
Length15	1	T	14.75	0.98	14.79	87	3.81	87.01	1.54	0.12
Length16	1	T	13.15	0.49	13.16	44.94	2.14	44.98	1.73	0.09
Length17	1	T	14.25	0.49	14.26	79.33	1.97	79.34	1.55	0.26
Length18	1	T	12.74	0.49	12.75	59.64	2.21	59.67	1.37	0.13
Length19	1	T	10.05	0.49	10.06	58.23	2.8	58.28	1.48	0.15
Length19b	1	T	13.59	0.49	13.6	52.59	2.07	52.62	1.48	0.15
Length19b	2	T	8.28	0.98	8.33	44.63	6.76	45.03	1.48	0.15
Length19c	1	T	12.18	0.49	12.19	75.08	2.31	75.09	1.48	0.15
Length20	1	T	13.02	1.47	13.1	80.51	6.45	80.57	1.4	0.16
Length20b	1	T	14.96	0	14.96	39.2	0	39.2	1.4	0.16

Length21	1	T	10.12	1.47	10.22	70.36	8.28	70.57	1.43	0.25
Length21b	1	T	12.94	1.96	13.09	62.75	8.63	63.09	1.43	0.25
Length22	1	T	13.33	1.47	13.42	29.05	6.3	29.67	1.39	0.17
Length23c	1	T	10.07	0.98	10.12	64.4	5.57	64.53	1.45	0.15
Length23d	1	T	12.67	1.47	12.75	77.23	6.63	77.32	1.45	0.15
Length24	1	T	9.44	0.49	9.45	54.34	2.98	54.4	1.6	0.18
Length24c	1	T	11.09	1.47	11.19	40.5	7.56	41.08	1.6	0.18
Length25	1	T	11.85	0.49	11.86	67.21	2.37	67.24	1.5	0.09
Length25	2	T	12.06	0.98	12.1	68.43	4.65	68.5	1.5	0.09
Length26	1	T	15.09	0.98	15.12	46.51	3.72	46.63	1.49	0.08
Length27	1	T	11.25	1.47	11.35	86.44	7.46	86.47	1.48	0.27
Length27	2	T	9.86	0.49	9.87	35.66	2.85	35.76	1.48	0.27
Length28	1	T	9.69	1.47	9.8	69.28	8.64	69.53	1.38	0.14
Length28b	1	T	12.32	1.96	12.48	73.29	9.05	73.5	1.38	0.14
Length28b	2	T	11.07	0.49	11.08	82.79	2.54	82.8	1.38	0.14
Length29	1	T	12.97	2.94	13.3	67.8	12.79	68.38	1.55	0.16
Length29b	1	T	12.36	0.98	12.4	15.89	4.54	16.51	1.55	0.16
Length29b	2	T	12.33	1.96	12.48	53.73	9.05	54.25	1.55	0.16
Length29d	1	T	10.75	1.47	10.85	68.14	7.8	68.35	1.55	0.16
Length29d	2	T	8.21	0	8.21	67.01	0	67.01	1.55	0.16
Length30	1	T	10.44	0.98	10.49	73.77	5.37	73.84	1.77	0.28
Length30b	1	T	13.21	0.98	13.25	59.64	4.25	59.73	1.77	0.28
Length30c	1	T	13.16	0	13.16	79.29	0	79.29	1.77	0.28
Length30c	2	T	10.2	0.49	10.21	73.55	2.75	73.57	1.77	0.28
Length30d	1	T	12.24	2.45	12.49	48.78	11.33	49.75	1.77	0.28
Length31	1	T	6.17	0.98	6.25	59.88	9.04	60.3	1.64	0.13
Length32	1	T	11.17	1.47	11.27	62.41	7.51	62.66	1.6	0.17
Length32b	1	T	5.96	0	5.96	23.46	0	23.46	1.6	0.17
Length33	1	T	14.68	2.45	14.88	18.19	9.49	20.44	1.57	0.17
Length33b	1	T	8.3	1.47	8.42	56.88	10.07	57.45	1.57	0.17
Length33c	1	T	9.69	1.96	9.89	72.31	11.45	72.67	1.57	0.17
Length33d	1	T	12.45	0.49	12.46	21.45	2.26	21.56	1.57	0.17
Length33e	1	T	13.49	2.94	13.81	56.95	12.31	57.8	1.57	0.17
Length34	1	T	12.26	0.98	12.3	27.6	4.58	27.94	1.44	0.11
Length35	1	T	12.31	1.96	12.47	49.47	9.06	50.08	1.59	0.15
Length35	2	T	12.93	1.47	13.01	15.74	6.5	17	1.59	0.15
Length36	1	T	13.39	2.94	13.71	47.58	12.4	48.79	1.45	0.17
Length36b	1	T	9.76	0.49	9.77	80.27	2.88	80.28	1.45	0.17
Length36c	1	T	11.91	0.49	11.92	60.99	2.36	61.02	1.45	0.17
Length36d	1	T	11.99	0.98	12.03	70.55	4.68	70.62	1.45	0.17
Length36e	1	T	12.76	1.96	12.91	49.82	8.75	50.38	1.45	0.17
Length36f	1	T	12.18	1.47	12.27	57.5	6.89	57.76	1.45	0.17
Length36g	1	T	12.75	1.47	12.83	78.55	6.59	78.63	1.45	0.17
Length37	1	T	12.41	1.47	12.5	42.21	6.77	42.65	1.67	0.26
Length37b	1	T	12.51	0.98	12.55	74.64	4.49	74.69	1.67	0.26

Length38	1	T	12.73	2.45	12.96	74.79	10.91	75.07	1.51	0.22
Length38c	1	T	12.45	0.49	12.46	16.94	2.26	17.08	1.51	0.22
Length38c	2	T	14.22	2.45	14.43	24.58	9.79	26.34	1.51	0.22
Length39	1	T	12.24	0	12.24	53.97	0	53.97	1.47	0.15
Length39b	1	T	14.1	0	14.1	70.53	0	70.53	1.47	0.15
Length40	1	T	14.33	1.47	14.4	42.4	5.87	42.72	1.58	0.13
Length40	2	T	11.12	0.49	11.13	63.78	2.53	63.81	1.58	0.13
Length40b	1	T	12.97	0	12.97	61.25	0	61.25	1.58	0.13
Length40c	1	T	7.07	0.49	7.09	81.25	3.97	81.27	1.58	0.13
Length40d	1	T	14.45	1.96	14.58	42.38	7.74	42.95	1.58	0.13
Length42	1	T	13.95	1.47	14.03	44.04	6.02	44.36	1.31	0.24
Length42b	1	T	11.87	3.44	12.36	70.14	16.14	70.96	1.31	0.24
Length42c	1	T	11.49	2.45	11.75	67.39	12.06	67.91	1.31	0.24
Length43	1	T	9.18	0.98	9.23	40.14	6.11	40.53	1.59	0.11
Length45b	1	T	11.13	0	11.13	54.19	0	54.19	1.72	0.55
Length45d	1	T	10.7	0.49	10.71	32.16	2.63	32.25	1.72	0.55
Length46	1	T	11.2	1.47	11.29	82.67	7.49	82.73	1.22	0.06
Length50	1	T	11.18	0	11.18	45.33	0	45.33	1.22	0.22
Length51	1	T	13.18	1.47	13.27	44.24	6.37	44.6	1.66	0.19
Length51b	1	T	14.39	3.44	14.8	80.62	13.43	80.88	1.66	0.19

A8 Durango A2 Standard

SD - Standard deviation. No. – number. All measurements in [µm]. Type: T – TINT, C- TINCLE. Extracted from FastTracks: v3.3.4

Length Name	Length No.	Type	Apparent Length	Corrected Z Depth	True Length	Azimuth	Dip	Angle to C-Axis	Dpar Average	Dpar SD
Length01	1	T	15.29	0.98	15.32	61.52	3.67	61.58	1.47	0.14
Length01b	1	T	15.87	0	15.87	42.58	0	42.58	1.47	0.14
Length01c	1	T	17.2	0.49	17.21	37.01	1.63	37.04	1.47	0.14
Length01d	1	T	15.62	0	15.62	56.55	0	56.55	1.47	0.14
Length01e	1	T	15.91	0.49	15.92	30.54	1.77	30.59	1.47	0.14
Length01f	1	T	16.17	1.96	16.29	46.3	6.92	46.7	1.47	0.14
Length01g	1	T	14.68	0	14.68	62.59	0	62.59	1.47	0.14
Length01h	1	T	15.74	1.47	15.81	73.87	5.34	73.94	1.47	0.14
Length01i	1	T	14.02	0.49	14.03	83.7	2	83.7	1.47	0.14
Length01j	1	T	15.12	1.96	15.25	62.67	7.4	62.91	1.47	0.14
Length01k	1	T	16.21	1.47	16.28	69.16	5.19	69.25	1.47	0.14
Length01l	1	T	16.04	0.49	16.05	77.08	1.75	77.09	1.47	0.14
Length01m	1	T	15.51	0.98	15.54	62.72	3.62	62.78	1.47	0.14
Length01n	1	T	15.89	0	15.89	65.58	0	65.58	1.47	0.14
Length01o	1	T	14.26	0.98	14.3	59.78	3.94	59.86	1.47	0.14
Length02	1	T	15.94	0.49	15.95	48.86	1.76	48.88	1.44	0.18
Length02b	1	T	15.44	0.98	15.47	77.96	3.64	77.99	1.44	0.18
Length02c	1	T	15.01	1.47	15.09	40.86	5.6	41.17	1.44	0.18
Length02d	1	T	14.87	1.47	14.94	36.85	5.66	37.22	1.44	0.18
Length02e	1	T	15.77	0.49	15.78	20.94	1.78	21.01	1.44	0.18
Length03	1	T	16.09	0.49	16.09	70.85	1.75	70.86	1.33	0.2
Length03b	1	T	16.99	0.49	17	63.64	1.65	63.65	1.33	0.2
Length03c	1	T	15.41	0.49	15.41	50.28	1.82	50.31	1.33	0.2
Length03g	1	T	15.12	0.98	15.15	75.04	3.71	75.08	1.33	0.2
Length05	1	T	15.36	0.49	15.37	36.74	1.83	36.78	1.41	0.27
Length05b	1	T	16.31	0.98	16.34	51.25	3.44	51.34	1.41	0.27
Length05c	1	T	16.05	0	16.05	57.28	0	57.28	1.41	0.27
Length05d	1	T	15.46	0.98	15.49	77.58	3.63	77.6	1.41	0.27
Length06	1	T	15.02	1.47	15.09	53.07	5.6	53.27	1.33	0.15
Length08c	1	T	16.78	0.49	16.78	70.55	1.68	70.56	1.42	0.19
Length08d	1	T	15.76	1.47	15.82	84.15	5.34	84.17	1.42	0.19
Length09	1	T	15.57	1.96	15.69	78.33	7.19	78.42	1.41	0.18
Length09b	1	T	16.05	0.98	16.08	75.62	3.5	75.65	1.41	0.18
Length09c	1	T	16.37	0	16.37	26.78	0	26.78	1.41	0.18
Length09d	1	T	15.26	0	15.26	68.39	0	68.39	1.41	0.18
Length09e	1	T	15.4	0.98	15.43	60.24	3.65	60.31	1.41	0.18
Length09f	1	T	16.91	0.98	16.94	55.77	3.32	55.84	1.41	0.18
Length09g	1	T	16.27	1.47	16.34	64.24	5.17	64.35	1.41	0.18

Length09h	1	T	14.76	1.96	14.89	57.25	7.58	57.57	1.41	0.18
Length09i	1	T	17.3	1.47	17.36	45.38	4.86	45.58	1.41	0.18
Length09j	1	T	14.91	0	14.91	43.22	0	43.22	1.41	0.18
Length09k	1	T	15.41	0.98	15.44	60.97	3.65	61.03	1.41	0.18
Length09l	1	T	15.65	1.96	15.77	69.87	7.15	70.04	1.41	0.18
Length09m	1	T	15.26	0.49	15.26	47.05	1.84	47.08	1.41	0.18
Length09n	1	T	15.27	1.47	15.34	41.6	5.51	41.9	1.41	0.18
Length09o	1	T	14.94	1.96	15.07	61.22	7.48	61.49	1.41	0.18
Length09p	1	T	15.7	1.47	15.77	72.9	5.36	72.98	1.41	0.18
Length09r	1	T	13.06	2.45	13.29	62.94	10.64	63.45	1.41	0.18
Length09s	1	T	13.69	1.96	13.83	22.26	8.16	23.63	1.41	0.18
Length10	1	T	15.05	1.96	15.18	55.14	7.43	55.48	1.37	0.09
Length11	1	T	14.51	3.44	14.91	66.35	13.32	67.03	1.31	0.14
Length11b	1	T	15.64	0.98	15.67	66.17	3.59	66.21	1.31	0.14
Length11c	1	T	14.46	0	14.46	74.45	0	74.45	1.31	0.14
Length11d	1	T	13.34	3.44	13.78	62.4	14.44	63.34	1.31	0.14
Length11d	2	T	13.69	0	13.69	77.21	0	77.21	1.31	0.14
Length11f	1	T	15.95	0.98	15.98	83.96	3.52	83.97	1.31	0.14
Length11g	1	T	15.81	1.96	15.93	78.08	7.08	78.17	1.31	0.14
Length12	1	T	16.32	3.44	16.68	57.06	11.89	57.85	1.37	0.18
Length12b	1	T	16.07	0.98	16.1	49.69	3.5	49.78	1.37	0.18
Length12c	1	T	15.67	0	15.67	70.23	0	70.23	1.37	0.18
Length12c	2	T	15.04	2.94	15.33	77.55	11.08	77.79	1.37	0.18
Length12d	1	T	15.73	1.96	15.86	26.13	7.11	27.01	1.37	0.18
Length12e	1	T	17.22	1.47	17.29	76.88	4.89	76.93	1.37	0.18
Length12f	1	T	16.83	1.96	16.94	74.6	6.65	74.71	1.37	0.18
Length12h	1	T	16.83	1.47	16.89	68.07	5	68.16	1.37	0.18
Length12i	1	T	15.26	1.96	15.39	54.34	7.33	54.67	1.37	0.18
Length12j	1	T	16.34	0.98	16.37	67.77	3.44	67.82	1.37	0.18
Length12k	1	T	16.52	0.49	16.52	63.46	1.7	63.47	1.37	0.18
Length12l	1	T	14.69	2.94	14.99	61.4	11.33	62.01	1.37	0.18
Length12l	2	T	14.94	1.47	15.01	86.71	5.63	86.73	1.37	0.18
Length12m	1	T	15.38	1.47	15.45	59.56	5.47	59.71	1.37	0.18
Length13	1	T	16.77	0	16.77	46.21	0	46.21	1.55	0.48
Length13b	1	T	16.52	1.47	16.58	74.33	5.09	74.39	1.55	0.48
Length13c	1	T	14.6	0.49	14.61	74.25	1.92	74.26	1.55	0.48
Length13d	1	T	13.64	0.49	13.65	85.92	2.06	85.92	1.55	0.48
Length13d	2	T	15.45	1.96	15.57	54.14	7.24	54.47	1.55	0.48
Length14	1	T	17.27	0.49	17.28	54.39	1.63	54.41	1.43	0.18
Length15	1	T	15.83	0	15.83	43.39	0	43.39	1.48	0.19
Length15b	1	T	15.9	1.96	16.02	70.12	7.04	70.28	1.48	0.19
Length15b	2	T	16.38	0.98	16.41	12.09	3.43	12.56	1.48	0.19
Length15c	1	T	15.6	0	15.6	66.62	0	66.62	1.48	0.19
Length15d	1	T	16.98	0	16.98	76.39	0	76.39	1.48	0.19
Length15d	2	T	15.04	0	15.04	51.69	0	51.69	1.48	0.19

Length15e	1	T	16.73	1.47	16.79	79.31	5.03	79.35	1.48	0.19
Length16	1	T	15.94	0.49	15.95	73.64	1.76	73.65	1.33	0.15
Length16b	1	T	15.21	0	15.21	74.87	0	74.87	1.33	0.15
Length16c	1	T	13.62	0.49	13.63	75.24	2.06	75.25	1.33	0.15
Length16d	1	T	15.31	0.49	15.31	82.98	1.84	82.98	1.33	0.15
Length16e	1	T	13.87	1.96	14	42.01	8.06	42.64	1.33	0.15
Length16e	2	T	14.49	2.45	14.7	63.91	9.61	64.3	1.33	0.15
Length16e	3	T	14.54	0.49	14.54	76.38	1.93	76.39	1.33	0.15
Length16f	1	T	13.42	0	13.42	84.83	0	84.83	1.33	0.15
Length16g	1	T	14.76	1.47	14.83	53.69	5.7	53.89	1.33	0.15
Length16h	1	T	15.29	3.93	15.78	71.14	14.41	71.76	1.33	0.15
Length16i	1	T	15.94	1.47	16.01	41.99	5.28	42.26	1.33	0.15
Length16j	1	T	14.05	0.98	14.09	53.34	4	53.44	1.33	0.15
Length16l	1	T	15	0	15	56.23	0	56.23	1.33	0.15
Length17	1	T	15.17	0	15.17	38.32	0	38.32	1.44	0.14
Length17b	1	T	14.31	1.96	14.44	71.99	7.81	72.16	1.44	0.14
Length17c	1	T	16.99	0	16.99	67.38	0	67.38	1.44	0.14
Length17d	1	T	13.98	0.49	13.99	66.85	2.01	66.87	1.44	0.14
Length17f	1	T	14.76	0	14.76	27.18	0	27.18	1.44	0.14

B Count data

B1 Sample VAH_23

Ns- Number of spontaneous tracks, SD- Standard deviation, T-calculated AFT age (IsoplotR version 5.0). ^{238}U mean - uranium concentration (LA-ICP-MS)

Grain no.	Ns	Track Density [tracks/cm²]	Dpar Average [µm]	SD (Dpar)	^{238}U mean [ppm]	2σ(^{238}U)	T [Ma]	1σ(t)	Comment counting	Comment LA-ICP-MS (^{238}U)
Grain01	101	2958286	1.36	0.14	21.54	0.55	260	26	Bad surface, difficult	
Grain02	52	2008606	1.37	0.14	15.59	0.49	244	34	Bad surface, difficult	
Grain03	80	1785720	1.31	0.17	7.38	0.24	451	51	Bad surface, difficult	
Grain04	69	1760643	1.31	0.08	10.93	1.36	304	41	Bad surface, difficult	Zoned
Grain05	69	1775143	1.26	0.14	8.74	0.33	381	46	Bad surface, difficult	
Grain06	131	2584487	1.29	0.1	8.24	0.34	579	52	Bad surface, difficult	
Grain07	42	980264	1.38	0.13	6.92	0.79	268	44	Bad surface, difficult	Zoned
Grain08	47	1349511	1.24	0.08	6.89	0.25	367	54		
Grain09	11	324302	1.22	0.1	2.40	0.17	256	78	dislocations	Zoned
Grain10	36	1021625	1.36	0.12	6.79	0.26	284	48	secure	
Grain11	29	1350510	1.19	0.11	3.75	0.14	660	123		Zoned
Grain12	114	3755026	1.42	0.18	16.02	1.45	437	46		Zoned
Grain16	79	2775577	1.51	0.19	43.30	1.64	123	14		
Grain18	39	1463793	1.24	0.18	5.18	0.28	523	85	unsure, many unclear dots,	Zoned
									bad surface	
Grain19	64	1362915	1.22	0.19	4.86	0.17	520	66		
Grain22	50	1208673	1.1	0.12	5.32	0.19	425	61		
Grain23	53	1118849	1.39	0.13	7.83	0.26	270	37		
Grain24	98	2821754	1.45	0.15	32.67	1.00	165	17		
Grain25	59	2755840	1.44	0.13	28.44	0.90	184	24	uncertain	
Grain26	110	3824448	1.34	0.14	41.96	1.93	174	17		Zoned
Grain36	23	640864	0.99	0.08	2.39	0.12	499	105		
Grain39	45	2067217	1.39	0.18	34.01	2.61	116	18		Zoned

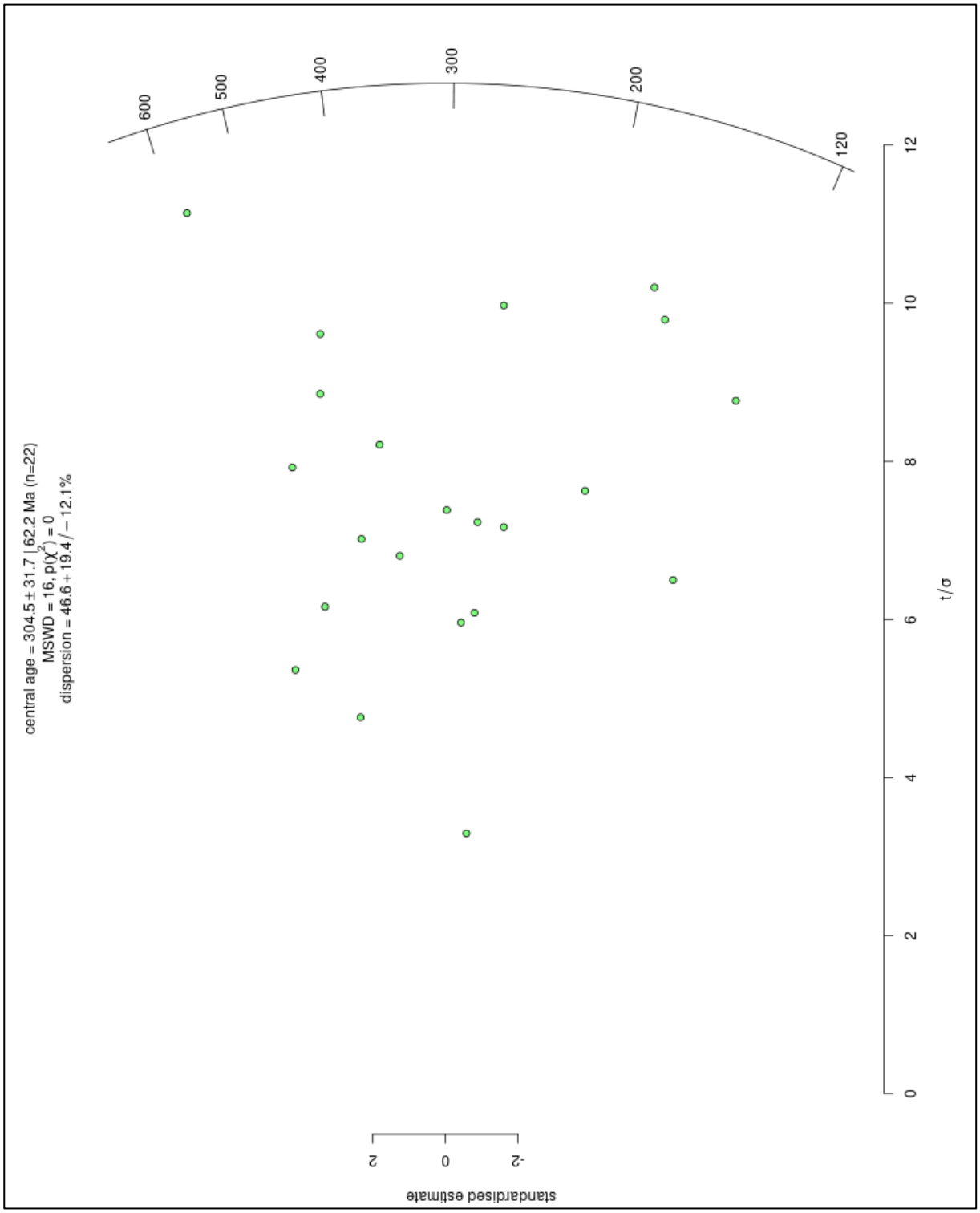

B1.1 Radial plot of single grain ages for the sample (IsoplotR v. 5.0) including the central age. N-number of grains used in calculation. MSWD- Mean Square of the Weighted Deviates. p(x^2)- p-value of a chi-square probability for homogeneity.

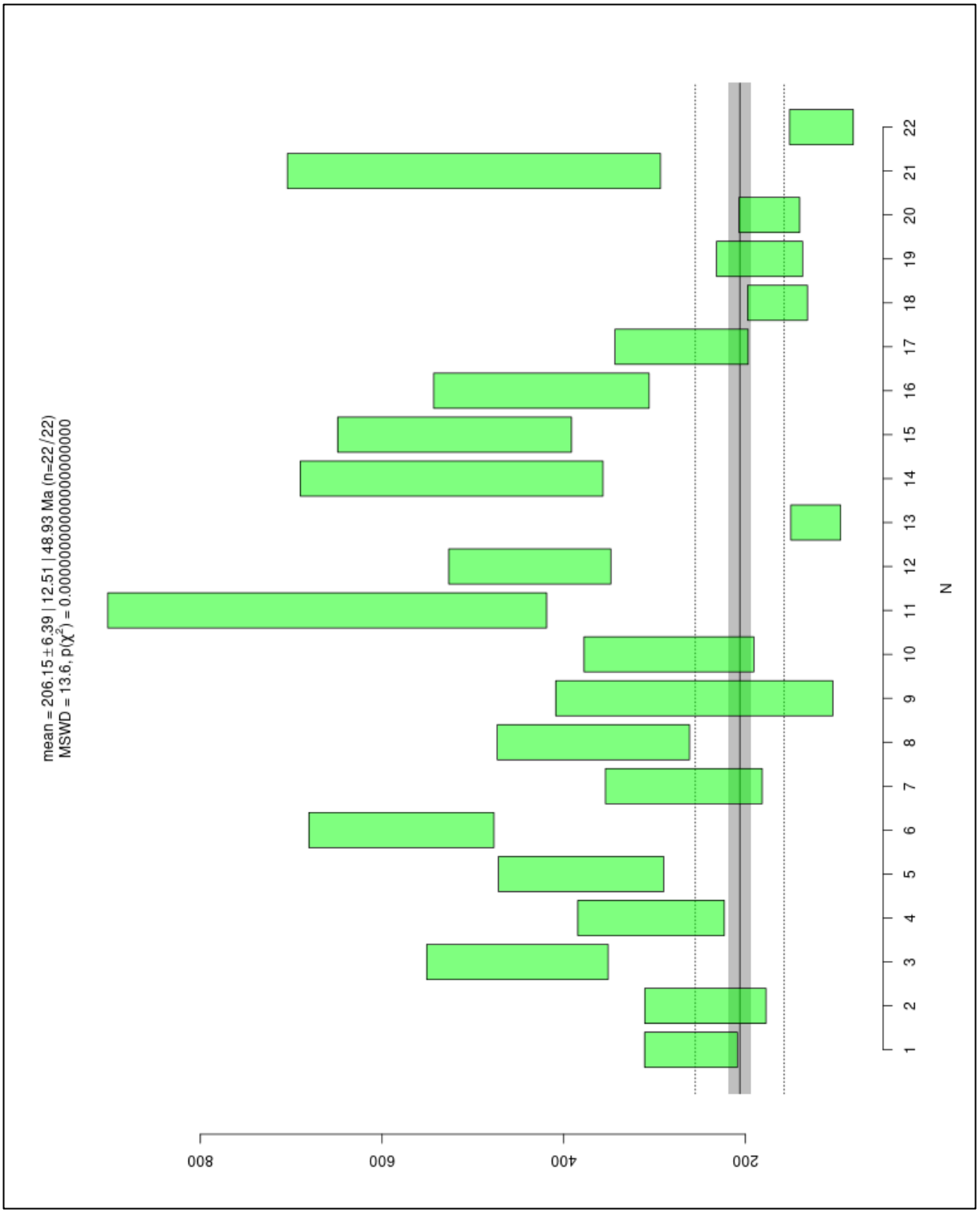

B1.2 Weighted mean plot for the sample (IsoplotR v. 5.0) showing single grain ages including error range. N- number of grains used in calculation/grain number. MSWD- Mean Square of the Weighted Deviates. $p(x^2)$- p-value of a chi-square probability for homogeneity.

B2 Sample VAH_26

Ns- Number of spontaneous tracks, SD- Standard deviation, T-calculated AFT age (IsoplotR version 5.0). ^{238}U mean - uranium concentration (LA-ICP-MS)

Grain no.	Ns	Track Density [tracks/cm²]	Dpar Average [µm]	SD (Dpar)	^{238}U mean [ppm]	$2\sigma(^{238}U)$	t [Ma]	$1\sigma(t)$	Comment counting	Comment LA-ICP-MS (^{238}U)
Grain01	390	7356418	1.17	0.16	55.62	1.20	251	13	Very dense, difficult to count precisely	
Grain04	78	2786235	1.13	0.25	17.61	0.54	299	34		Zoned
Grain07	41	1470277	0.96	0.31	3.39	0.11	788	124	dislocations	Zoned
Grain08	191	5157549	1.21	0.19	48.91	1.07	201	15	Dense, difficult to count precisely	
Grain10	69	3008984	1.01	0.19	13.69	0.56	411	50	Zoned, dense area which was difficult to count precisely	Zoned
Grain11	30	840092	0.96	0.23	2.72	0.09	570	105		Slightly zoned
Grain12	19	672613	1.11	0.18	2.61	0.14	480	111		Zoned
Grain14	109	2255419	0.91	0.13	16.31	0.36	262	25		
Grain16	50	2184859	1.24	0.11	29.30	0.81	142	20	Dislocations	
Grain20	159	4115261	1.44	0.19	37.55	1.21	208	17	Difficult, unidentifiable dots	Zoned
Grain28	28	903703	1.02	0.19	5.06	0.26	336	64	Dislocations	Zoned
Grain29	37	1658922	0.98	0.12	4.37	0.26	695	116	Very uncertain, very dense patch	Zoned
Grain30	43	1853445	1.00	0.18	5.79	0.39	590	92	blurry, difficult to count precise	Zoned
Grain31	48	2303006	1.11	0.19	11.87	0.34	364	53		Zoned
Grain33	32	557173	1.32	0.27	5.78	0.33	184	33	difficult	Zoned
Grain35	20	681443	1.19	0.15	7.09	0.43	183	41		Zoned

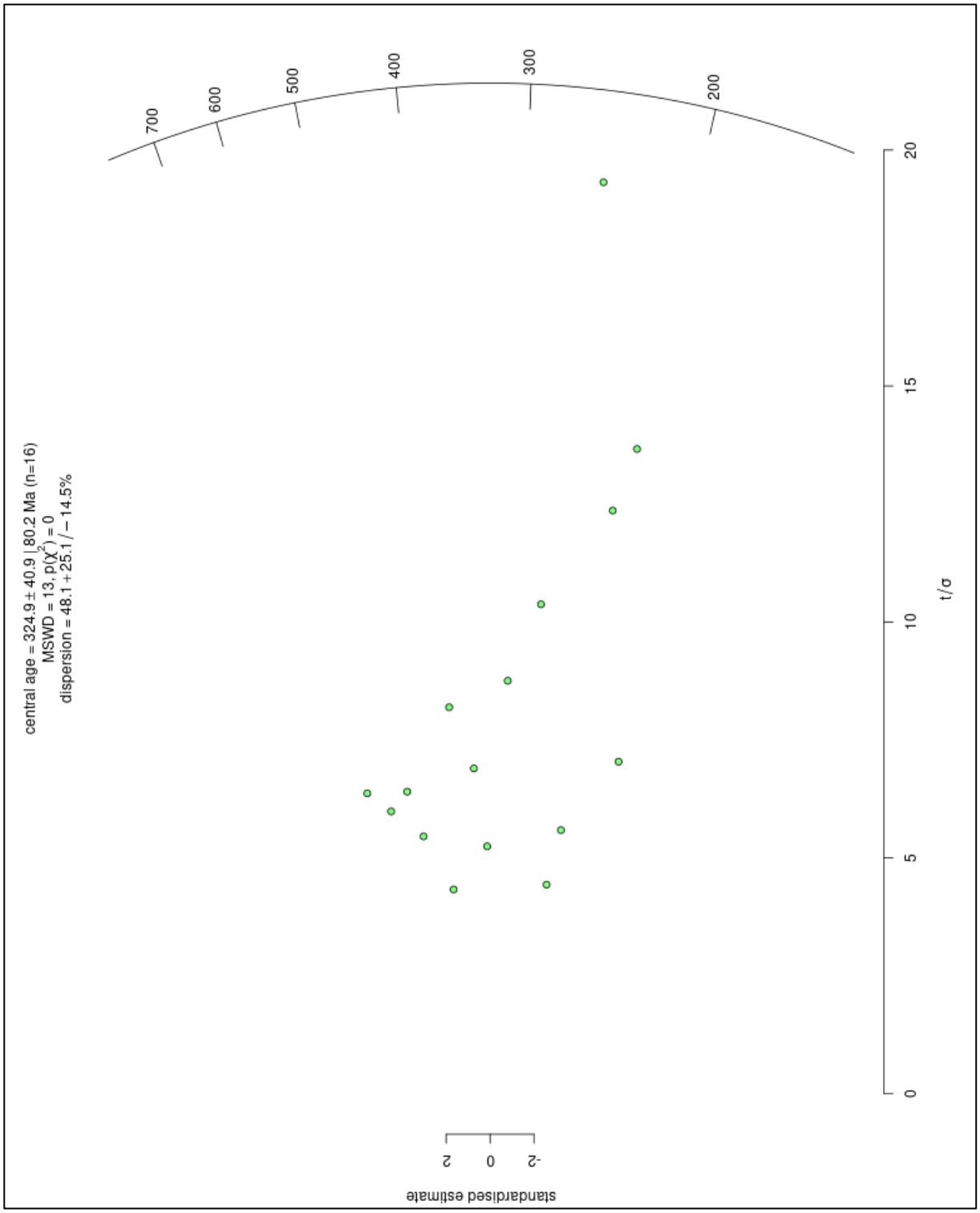

B2.1 Radial plot of single grain ages for the sample (IsoplotR v. 5.0) including the central age. N-number of grains used in calculation. MSWD- Mean Square of the Weighted Deviates. $p(x^2)$- p-value of a chi-square probability for homogeneity.

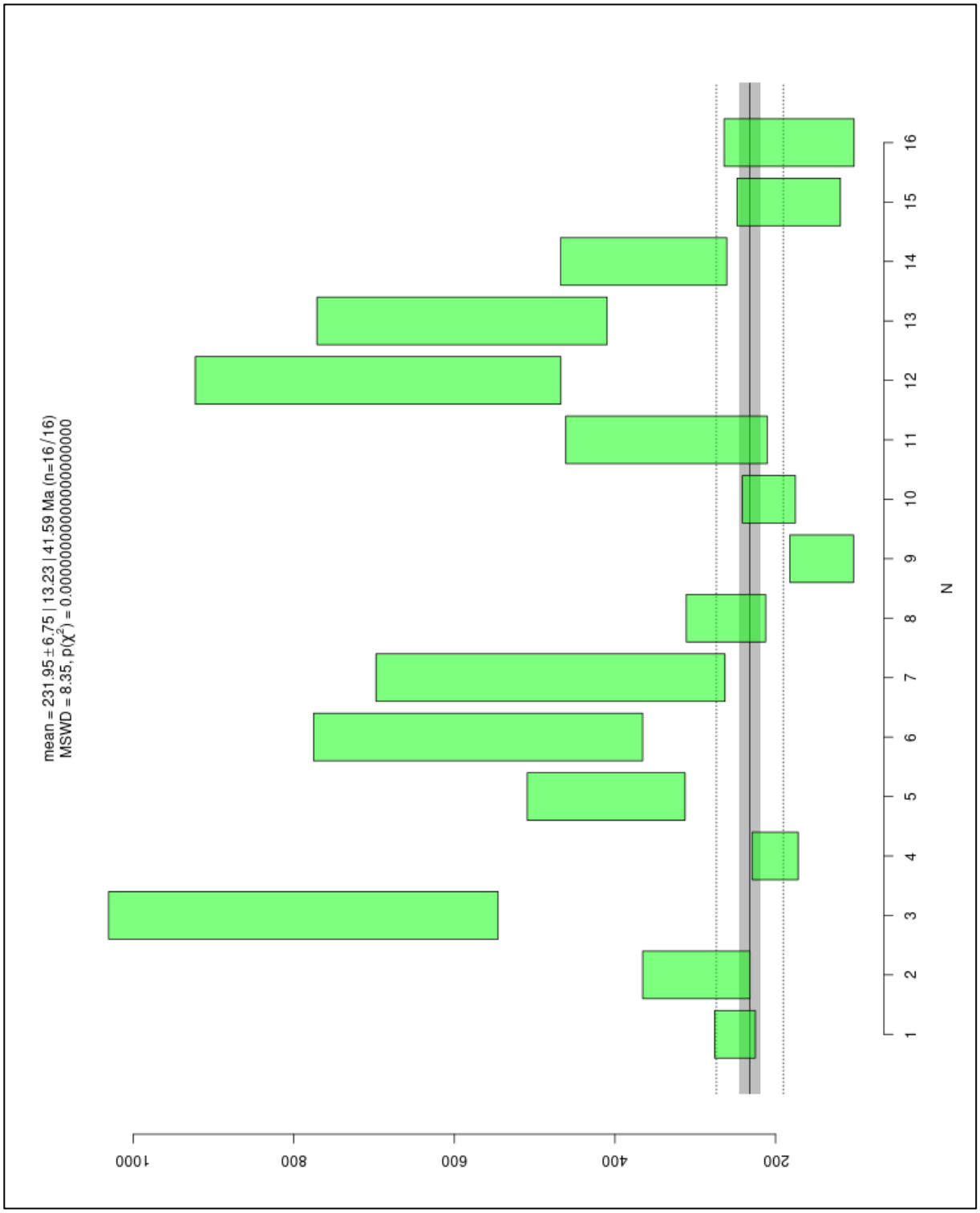

B2.2 Weighted mean plot for the sample (IsoplotR v. 5.0) showing single grain ages including error range. N- number of grains used in calculation/grain number. MSWD- Mean Square of the Weighted Deviates. $p(x^2)$- p-value of a chi-square probability for homogeneity.

B3 Sample VAH_31

Ns- Number of spontaneous tracks, SD- Standard deviation, T-calculated AFT age (IsoplotR version 5.0). ^{238}U mean - uranium concentration (LA-ICP-MS)

Grain no.	Ns	Track Density [tracks/cm²]	Dpar Average [µm]	SD (Dpar)	^{238}U mean [ppm]	2σ(^{238}U)	T [Ma]	1σ(t)	Comment counting	Comment LA-ICP-MS (^{238}U)
Grain01	48	780688	1.13	0.08	6.52	0.24	227	33		Zoned
Grain02	15	334161	0.89	0.11	3.42	0.12	186	48	blurry picture	
Grain17	23	496298	1.02	0.12	5.1	0.30	185	39		
Grain20	42	1292698	1.20	0.08	6.21	0.59	390	63	uncertain	Weakly zoned
Grain21	10	353864	1.19	0.13	3.88	0.21	174	55		
Grain22	21	525809	1.08	0.19	1.95	0.24	501	114		Zoned
Grain23	21	639920	1.13	0.21	2.58	0.26	462	104	uncertain	Weakly zoned
Grain25	43	550708	0.98	0.15	5.64	0.31	186	29		
Grain26	61	693760	0.91	0.13	3.69	0.32	353	48		Weakly zoned
Grain27	42	888818	0.98	0.23	4.94	0.29	338	53		
Grain29	28	424378	1.20	0.14	8.3	0.50	98	19	blurry picture	
Grain31	16	422275	1.13	0.09	6.38	0.36	127	32		
Grain32	8	157765	1.10	0.08	1.71	0.10	176	62		
Grain33	20	433415	1.17	0.12	3.53	0.24	233	53		
Grain34	36	696967	1.23	0.19	9.34	1.23	143	26		Zoned
Grain35	15	505375	1.13	0.04	6.68	0.71	145	38		Zoned
Grain36	22	222500	1.31	0.16	1.86	0.31	227	52		Zoned
Grain37	27	431575	1.21	0.16	4.58	0.26	179	35		
Grain38	31	578703	1.19	0.10	7.03	0.34	157	29		
Grain39	49	737731	1.15	0.09	3.59	0.27	385	57		Zoned
Grain40	26	469332	1.38	0.62	4.10	0.20	217	43		

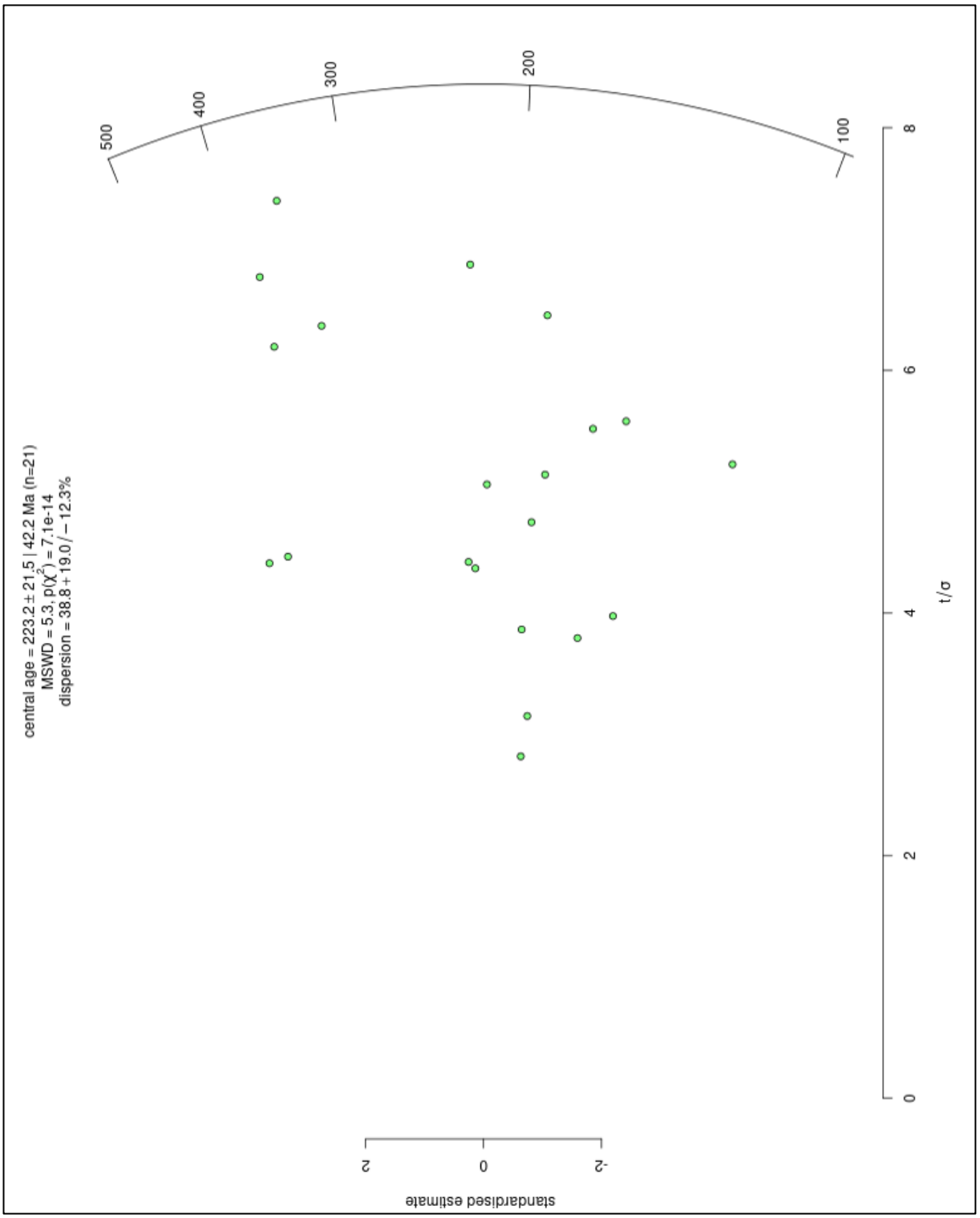

B3.1 Radial plot of single grain ages for the sample (IsoplotR v. 5.0) including the central age. N-number of grains used in calculation. MSWD- Mean Square of the Weighted Deviates. p(x^2)- p-value of a chi-square probability for homogeneity.

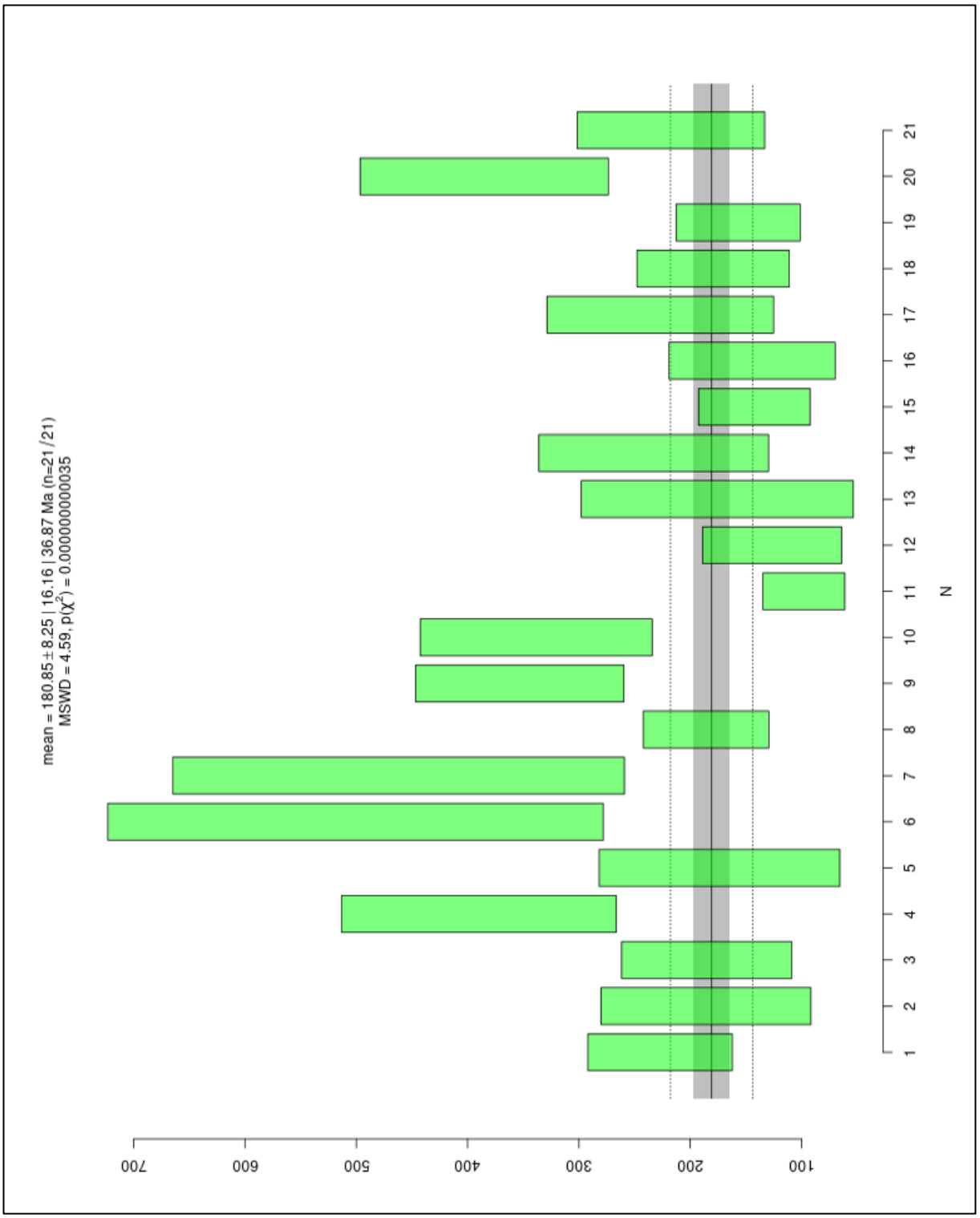

B3.2 Weighted mean plot for the sample (IsoplotR v. 5.0) showing single grain ages including error range. N- number of grains used in calculation/grain number. MSWD- Mean Square of the Weighted Deviates. p(x^2)- p-value of a chi-square probability for homogeneity.

B4 Sample VAH_42

Ns- Number of spontaneous tracks, SD- Standard deviation, T-calculated AFT age (IsoplotR version 5.0). ^{238}U mean - uranium concentration (LA-ICP-MS)

Grain no.	Ns	Track Density [tracks/cm²]	DPar Average [µm]	SD (Dpar)	^{238}U mean [ppm]	$2\sigma(^{238}U)$	T [Ma]	$1\sigma(t)$	Comment counting	Comment LA-ICP-MS (^{238}U)
Grain01	90	1859690	1.39	0.11	26.83	0.59	133	14	picture partly blurry	Weakly zoned
Grain02	82	4369998	1.15	0.14	36.11	1.02	230	26	very blurry	Zoned
Grain04	67	1759714	1.19	0.14	15.43	0.36	217	27	very blurry	Weakly zoned
Grain07	128	3211864	1.19	0.05	29.79	1.60	205	19		Zoned
Grain08	47	2705473	0.98	0.21	15.62	0.70	326	48	blurry	Zoned
Grain12	53	2628360	1.20	0.06	23.82	1.79	210	30		Zoned
Grain14	25	641588	1.09	0.23	6.36	0.34	192	39	blurry, dislocations	Zoned
Grain32	128	3139418	1.10	0.13	23.23	2.05	256	25		Zoned
Grain35	200	6718464	1.22	0.07	76.53	2.03	167	12		
Grain38	28	689286	1.15	0.17	9.45	0.31	139	26	blurry	
Grain40	136	6071236	1.14	0.34	100.63	7.57	116	11		Zoned
Grain41	81	4488651	1.27	0.20	45.33	2.17	188	21	blurry	Zoned
Grain43	66	2132045	1.15	0.13	21.96	0.66	185	23		Zoned
Grain46	65	2793087	0.93	0.29	26.34	1.46	202	26	blurry	Zoned
Grain47	68	2237123	1.07	0.14	16.11	0.91	263	33		
Grain48	86	2915022	1.28	0.23	25.30	1.00	219	24		
Grain49	130	2936314	1.30	0.15	30.79	3.00	182	18		Zoned
Grain50	22	754863	1.34	0.08	10.10	0.98	143	31		
Grain52	76	4534799	1.13	0.08	42.71	2.29	202	24		
Grain55	109	2209008	1.17	0.07	24.88	2.2	169	18		Zoned

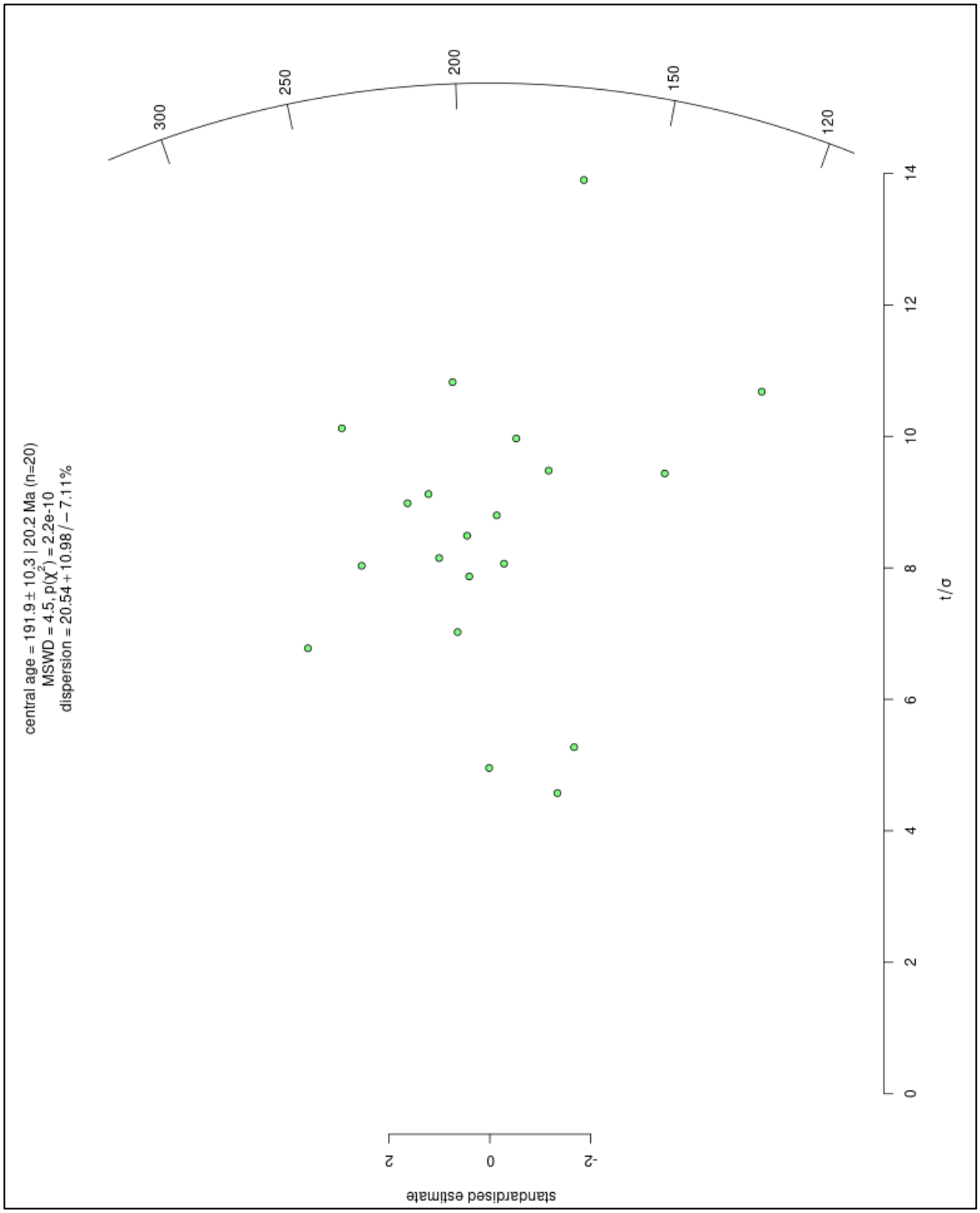

B4.1 Radial plot of single grain ages for the sample (IsoplotR v. 5.0) including the central age. N-number of grains used in calculation. MSWD- Mean Square of the Weighted Deviates. p(x^2)- p-value of a chi-square probability for homogeneity.

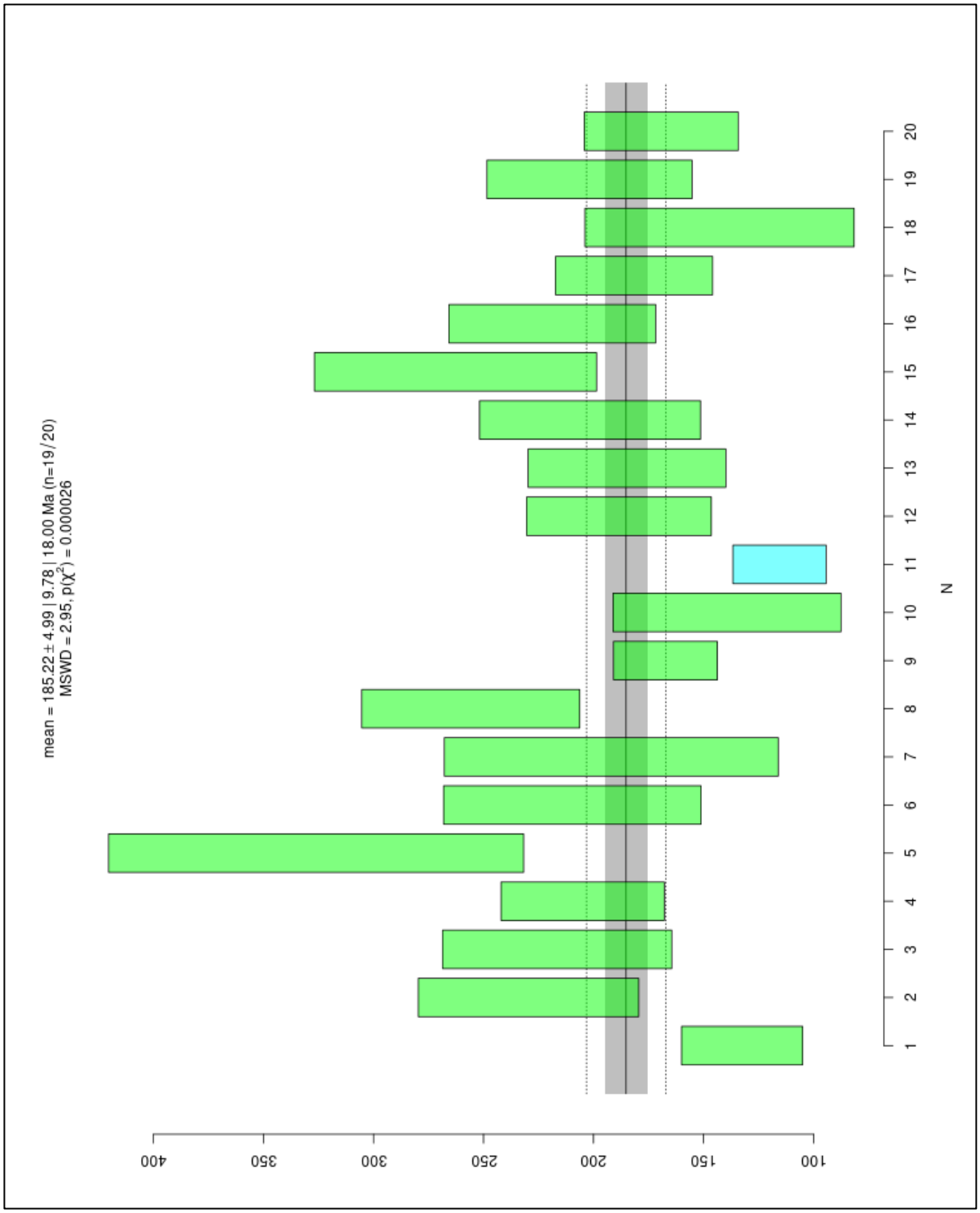

B4.2 Weighted mean plot for the sample (IsoplotR v. 5.0) showing single grain ages including error range. N- number of grains used in calculation/grain number. MSWD- Mean Square of the Weighted Deviates. p(x^2)- p-value of a chi-square probability for homogeneity.

B5 Sample MLM_134

Ns- Number of spontaneous tracks, SD- Standard deviation, T-calculated AFT age (IsoplotR version 5.0). ^{238}U mean - uranium concentration (LA-ICP-MS)

Grain no.	Ns	Track Density [tracks/cm²]	Dpar Average [µm]	SD (Dpar)	^{238}U mean [ppm]	2σ(^{238}U)	T [Ma]	1σ(t)	Comment counting	Comment LA-ICP-MS (^{238}U)
Grain01	9	247259	1.07	0.10	1.67	0.09	280	94		
Grain04	19	610886	1.09	0.12	9.52	0.54	123	28	Dislocations, uncertain count	
Grain05	5	135355	0.89	0.15	0.75	0.06	339	152	Dislocations, uncertain count	
Grain06	141	3044313	1.16	0.08	39.41	1.43	148	13		
Grain08	9	415479	1.06	0.12	3.50	0.13	225	75		
Grain11	32	952984	1.16	0.13	7.62	0.23	237	42		
Grain14	109	3091195	1.26	0.14	29.73	1.48	198	20		
Grain15	40	987830	1.17	0.11	10.92	0.28	172	27	Scarred surface	
Grain17	10	218862	0.97	0.11	0.95	0.05	430	137		
Grain18	39	789443	1.11	0.13	7.37	0.47	204	33		
Grain22	3	82057	0.86	0.21	0.71	0.04	219	127		
Grain23	14	372294	0.98	0.04	6.84	0.22	104	28		
Grain24	51	673496	1.07	0.12	7.59	0.31	169	24		
Grain25	67	2286902	1.05	0.10	25.3	0.67	172	21	Dislocations, scarred surface	
Grain27	2	51182	1.14	0.13	0.64	0.04	153	108		
Grain28	9	267665	1.05	0.03	1.05	0.05	474	159		
Grain30	52	2439040	0.91	0.20	36.33	0.89	128	18	Bad quality image, difficult to see tracks	
Grain31	39	1982652	1.04	0.12	19.68	0.57	192	31	Bad surface	

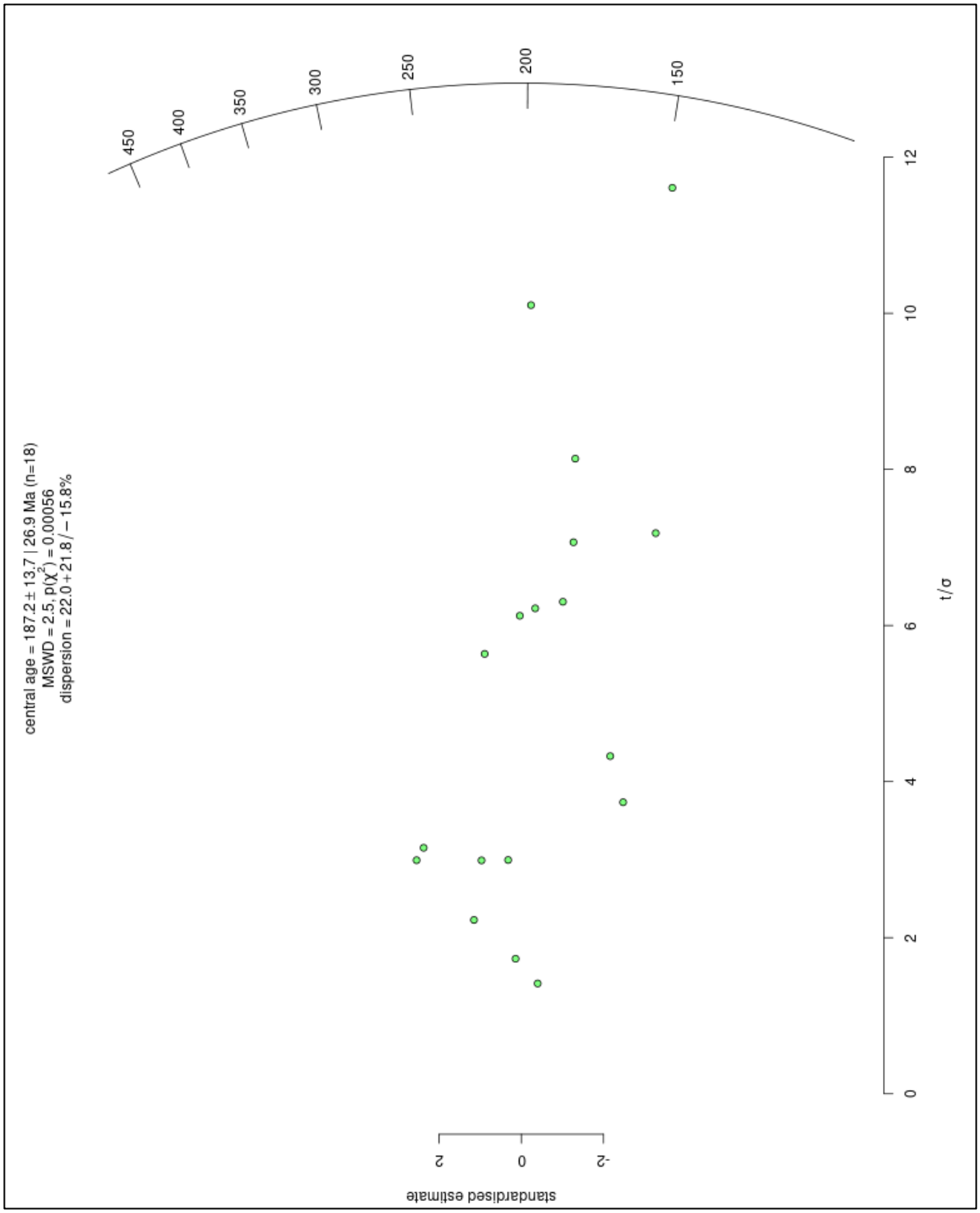

B5.1 Radial plot of single grain ages for the sample (IsoplotR v. 5.0) including the central age. N-number of grains used in calculation. MSWD- Mean Square of the Weighted Deviates. p(x^2)- p-value of a chi-square probability for homogeneity.

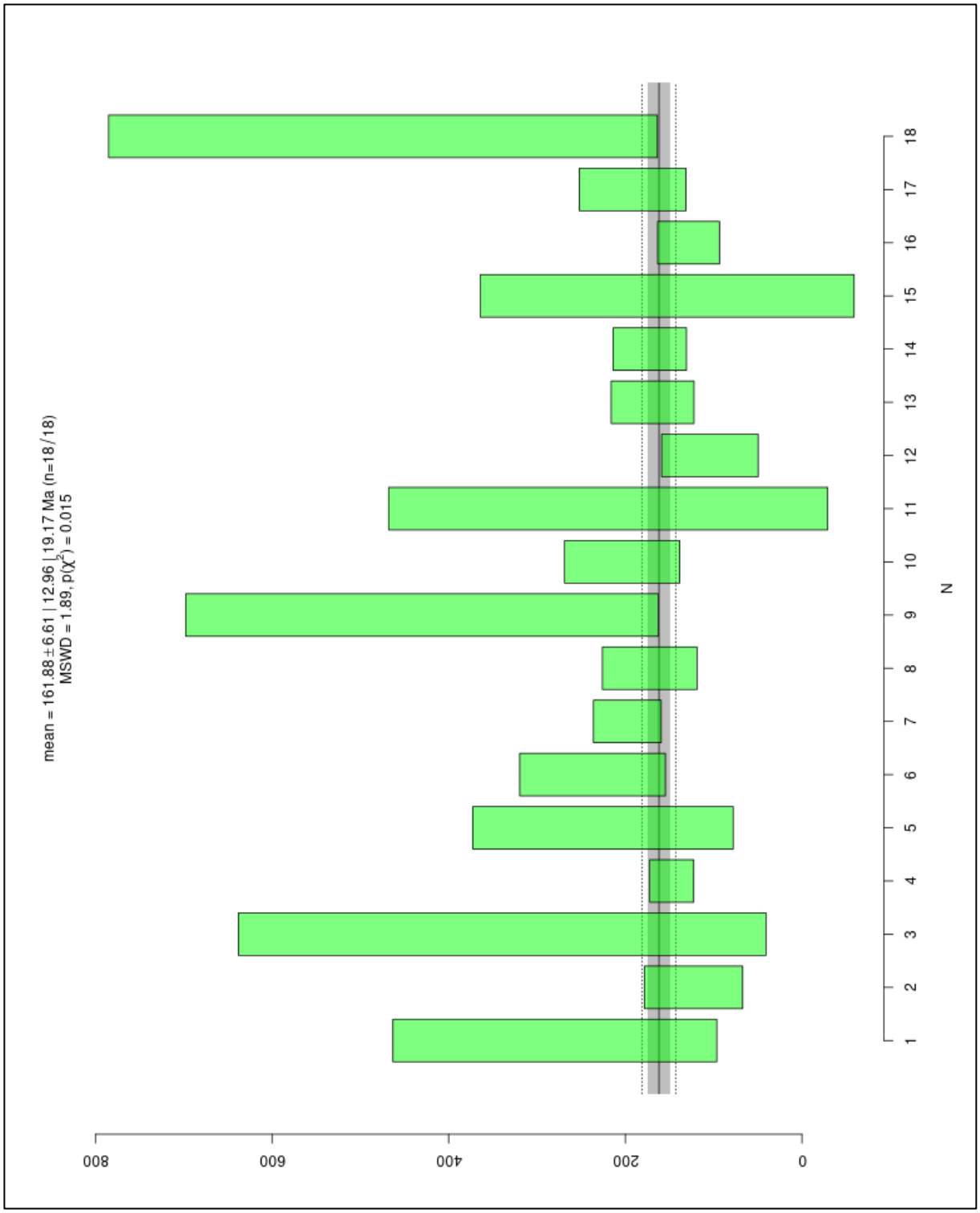

B5.2 Weighted mean plot for the sample (IsoplotR v. 5.0) showing single grain ages including error range. N- number of grains used in calculation/grain number. MSWD- Mean Square of the Weighted Deviates. $p(x^2)$- p-value of a chi-square probability for homogeneity.

B6 Sample VAH_48

Ns- Number of spontaneous tracks, SD- Standard deviation, T-calculated AFT age (IsoplotR version 5.0). ^{238}U mean - uranium concentration (LA-ICP-MS)

Grain no.	Ns	Track Density [tracks/cm²]	Dpar Average [µm]	SD (Dpar)	^{238}U mean [ppm]	2σ(^{238}U)	T [Ma]	1σ(t)	Comment counting	Comment LA-ICP-MS (^{238}U)
Grain25	75	1739992	1.19	0.02	37.61	2.30	89	11		Zoned
Grain26	45	785849	1.21	0.07	5.12	0.16	290	43		Zoned
Grain28	67	1055947	1.22	0.15	7.51	0.40	266	33		Zoned
Grain29	17	273011	1.12	0.20	0.76	0.03	659	160		
Grain31	47	1424710	1.26	0.12	41.55	1.79	66	10		Zoned
Grain35	37	1074120	1.27	0.10	22.17	1.24	93	15		Zoned
Grain36	35	624385	1.05	0.06	5.26	0.46	225	39		Zoned
Grain37	27	970246	1.16	0.11	14.06	1.13	132	26		Zoned
Grain38	33	585386	1.07	0.11	5.10	0.60	218	40		Zoned
Grain39	51	760530	1.04	0.11	10.95	0.28	133	19		
Grain40	52	978890	1.00	0.17	8.81	0.19	211	29		
Grain41	12	250970	1.16	0.11	1.49	0.11	317	92		Zoned
Grain42	48	944347	1.28	0.10	14.13	0.44	128	19		Zoned
Grain44	34	696956	1.08	0.06	9.29	0.56	143	25		Zoned
Grain45	29	368449	1.20	0.09	3.52	0.15	199	37		Zoned
Grain47	11	230958	1.15	0.11	1.47	0.05	296	90		
Grain48	106	2189119	1.17	0.10	27.35	0.74	153	15		
Grain50	67	751323	1.19	0.05	24.88	1.33	58	7		Zoned
Grain51	34	814110	1.13	0.09	10.04	0.30	155	27		Zoned

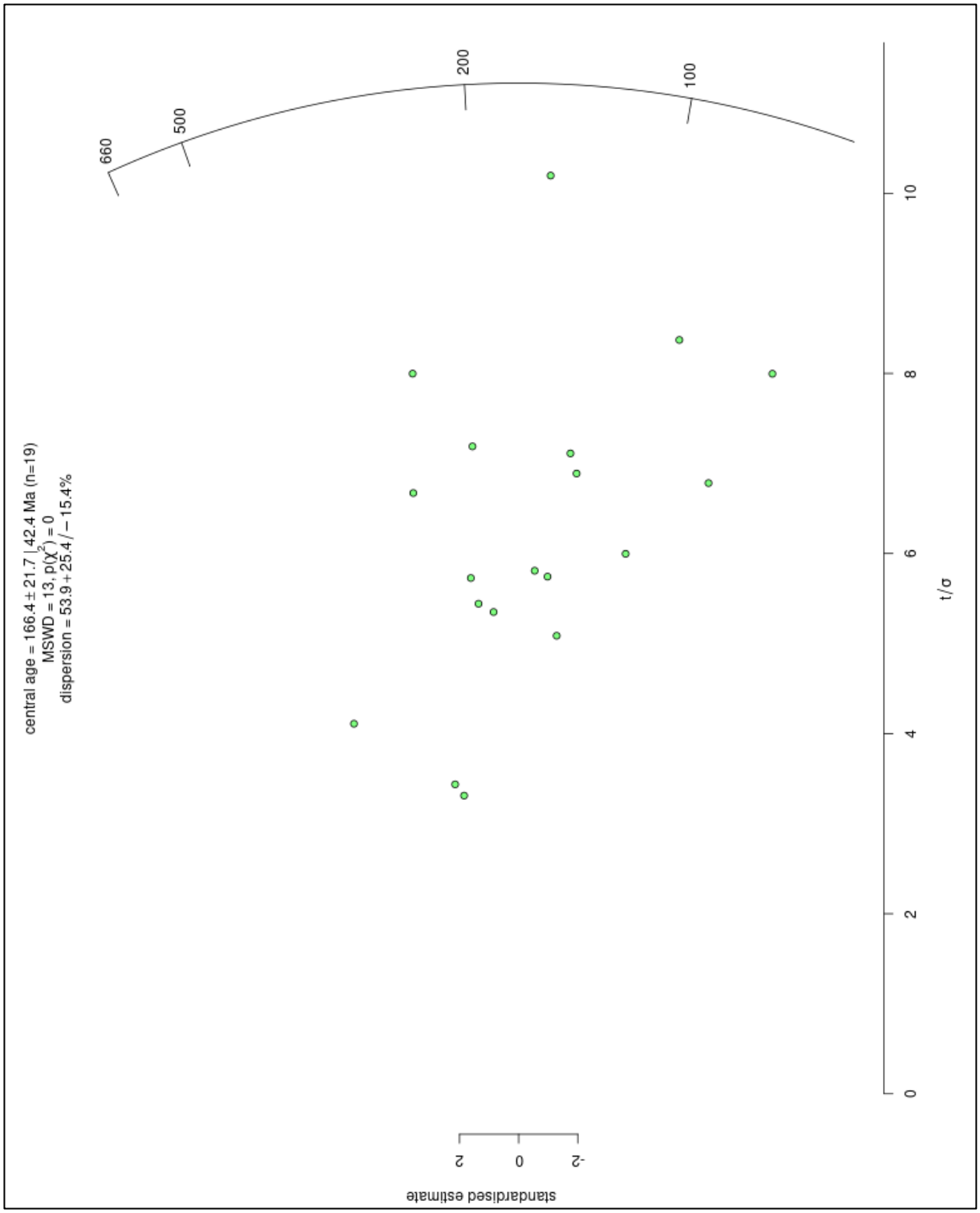

B6.1 Radial plot of single grain ages for the sample (IsoplotR v. 5.0) including the central age. N-number of grains used in calculation. MSWD- Mean Square of the Weighted Deviates. p(x^2)- p-value of a chi-square probability for homogeneity.

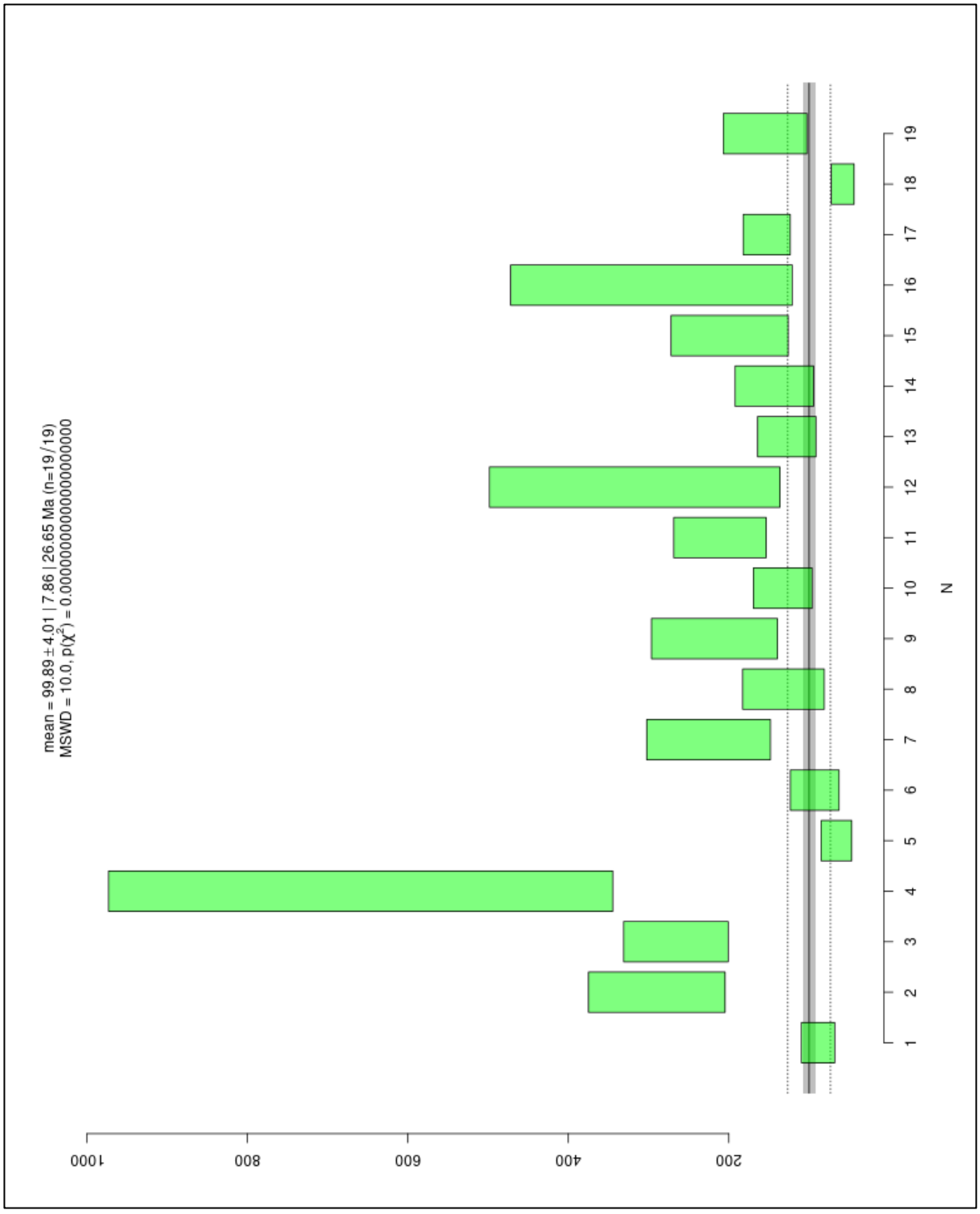

B6.2 Weighted mean plot for the sample (IsoplotR v. 5.0) showing single grain ages including error range. N- number of grains used in calculation/grain number. MSWD- Mean Square of the Weighted Deviates. $p(x^2)$- p-value of a chi-square probability for homogeneity.

B7 Sample VAH_78

Ns- Number of spontaneous tracks, SD- Standard deviation, T-calculated AFT age (IsoplotR version 5.0). ^{238}U mean - uranium concentration (LA-ICP-MS)

Grain no.	Ns	Track Density [tracks/cm²]	Dpar Average [µm]	SD (Dpar)	^{238}U mean [ppm]	2σ(^{238}U)	T [Ma]	1σ(t)	Comment counting	Comment LA-ICP-MS (^{238}U)
Grain01	52	548444	0.99	0.22	4.41	0.14	236	33		
Grain03	77	1216706	1.03	0.18	14.34	0.34	162	19		
Grain05	21	304358	0.83	0.10	6.98	0.17	84	18		
Grain07	36	620283	0.98	0.10	5.54	0.28	213	36		Zoned
Grain09	20	551006	1.00	0.12	8.70	0.29	121	27		
Grain10	8	110876	0.83	0.16	0.82	0.04	256	91		
Grain11	145	1692235	1.06	0.09	20.57	0.59	157	13		
Grain12	77	1738084	1.20	0.20	20.63	2.22	161	20		Zoned
Grain13	6	141353	0.85	0.16	1.23	0.05	218	89		
Grain14	105	2127533	1.01	0.09	21.97	1.07	184	19		Zoned
Grain15	33	661973	0.95	0.11	12.01	0.44	106	19		
Grain17	26	484427	1.05	0.14	6.83	0.25	136	27		
Grain19	50	807086	0.86	0.16	10.21	0.49	151	22		Zoned
Grain20	54	656206	0.80	0.14	7.17	0.31	174	24		
Grain21	34	644048	0.86	0.19	9.35	0.68	132	23		Zoned
Grain23	4	95406	1.07	0.23	0.87	0.12	208	105		Zoned
Grain25	25	776571	0.98	0.08	13.16	0.50	113	23		
Grain27	34	1216867	1.04	0.09	25.56	1.33	91	16		
Grain29	24	330900	1.03	0.21	6.16	0.24	103	21		
Grain30	69	1606777	1.12	0.08	21.19	0.97	145	18		Weakly zoned
Grain39	13	351369	0.98	0.08	3.93	0.18	170	47		

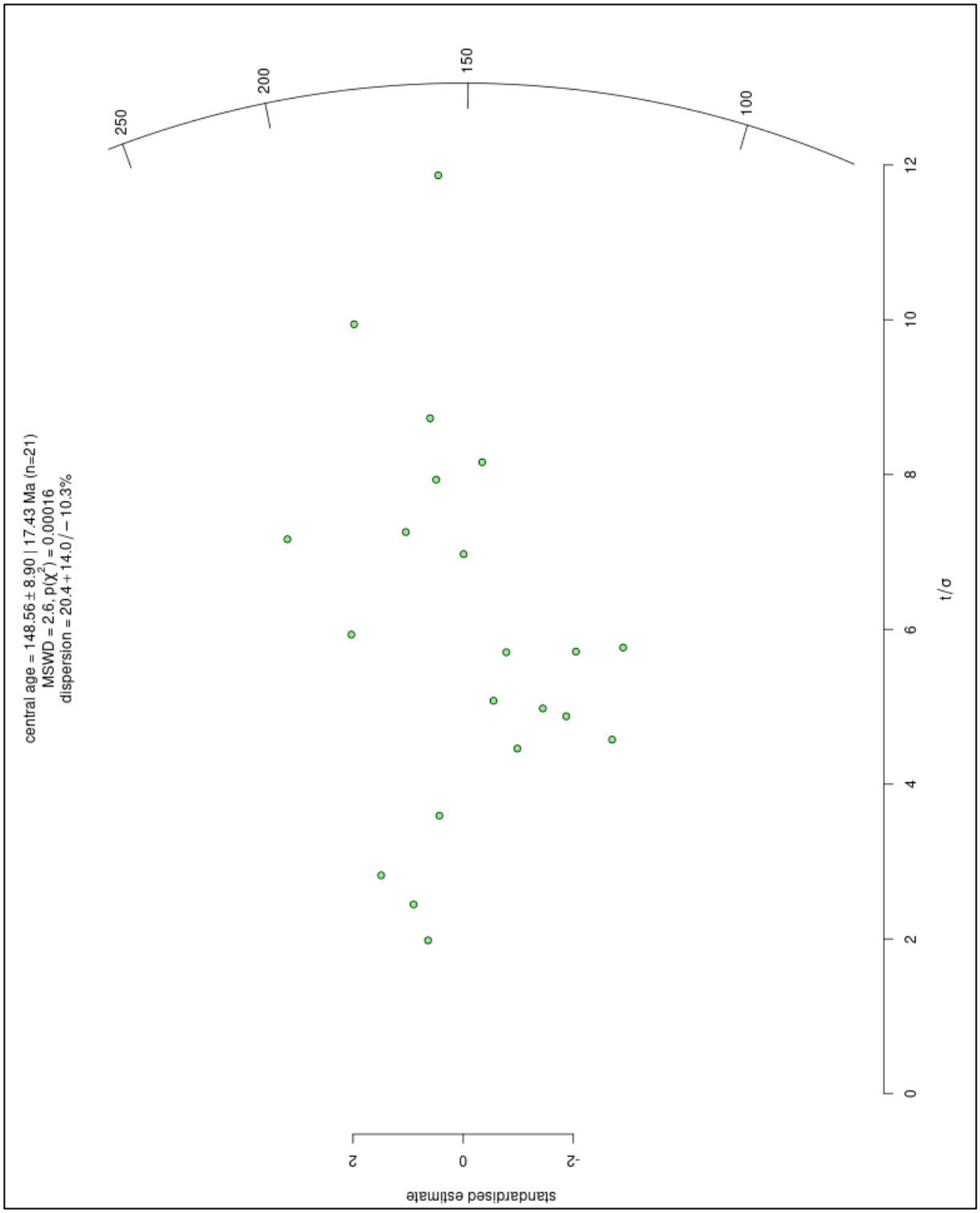

B7.1 Radial plot of single grain ages for the sample (IsoplotR v. 5.0) including the central age. N-number of grains used in calculation. MSWD- Mean Square of the Weighted Deviates. p(x^2)- p-value of a chi-square probability for homogeneity.

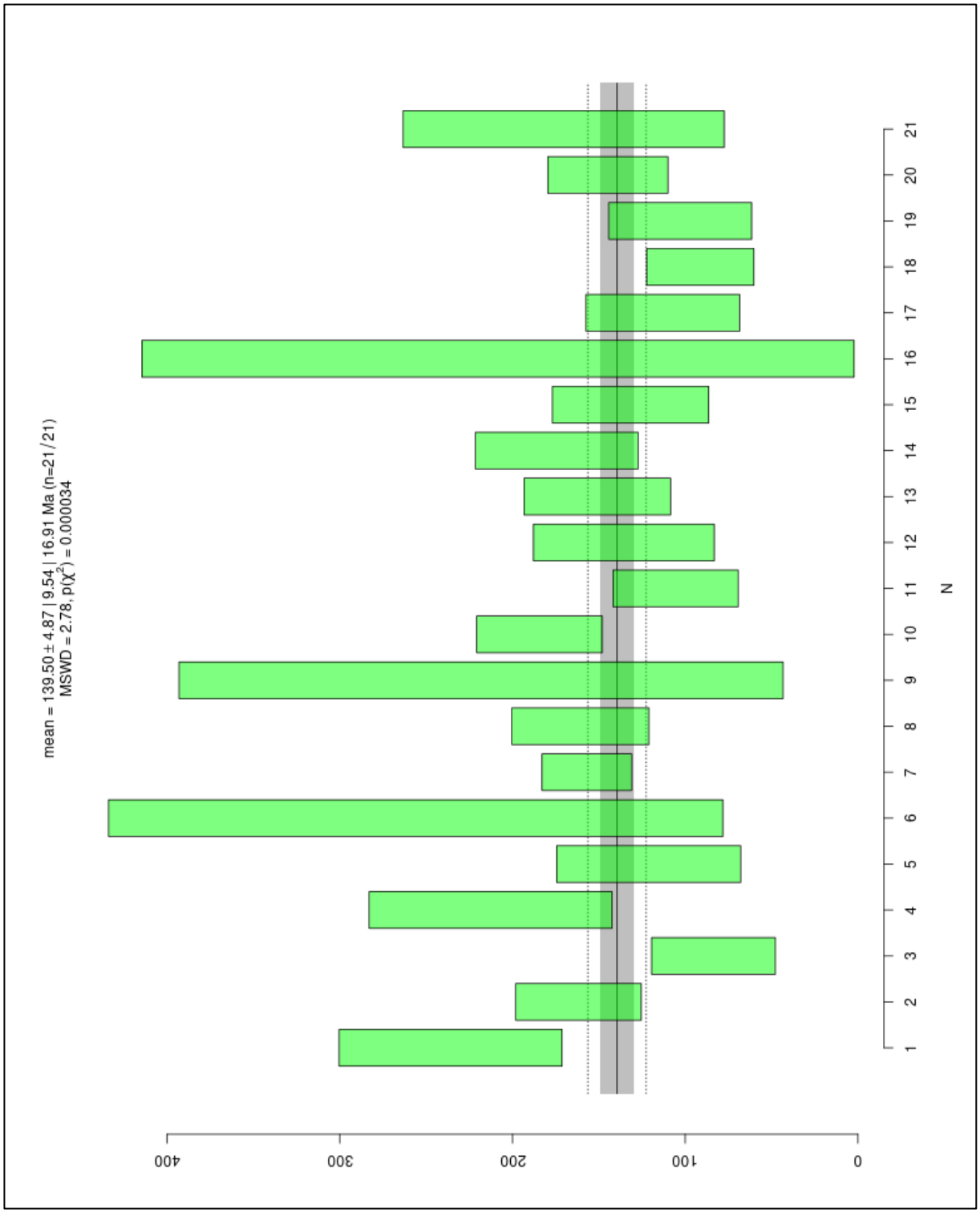

B7.2 Weighted mean plot for the sample (IsoplotR v. 5.0) showing single grain ages including error range. N- number of grains used in calculation/grain number. MSWD- Mean Square of the Weighted Deviates. p(x^2)- p-value of a chi-square probability for homogeneity.

B8 Sample VAH44_2

Ns- Number of spontaneous tracks, SD- Standard deviation, T-calculated AFT age (IsoplotR version 5.0). ^{238}U mean - uranium concentration (LA-ICP-MS)

Grain no.	Ns	Track Density [tracks/cm²]	Dpar Average [µm]	SD (Dpar)	^{238}U mean [ppm]	2σ(^{238}U)	t [Ma]	1σ(t)	Comment counting	Comment LA-ICP-MS (^{238}U)
Grain01	86	1320005	1.03	0.05	17.66	0.30	143	15		
Grain02	46	1023074	1.30	0.14	22.67	0.50	87	13		Weakly zoned
Grain03	87	1441633	1.30	0.08	30.7	0.90	90	10		
Grain04	55	1808044	1.25	0.13	20.17	0.59	171	23		
Grain05	186	2625871	1.15	0.17	40.17	1.43	125	9		
Grain06	28	470055	1.07	0.09	7.31	0.28	123	23		
Grain07	89	1263334	1.25	0.17	25.13	1.02	96	10		
Grain08	58	1087598	1.13	0.16	15.47	0.91	134	18		Zoned
Grain09	43	1159412	1.28	0.09	12.49	0.60	177	27		Zoned
Grain10	70	1510052	1.19	0.08	18.98	0.99	152	19		Zoned
Grain11	98	1273337	1.40	0.17	20.62	0.95	118	12		
Grain13	60	860474	1.17	0.16	12.28	0.58	134	18		
Grain14	14	186784	1.07	0.25	2.58	0.19	138	37		Zoned
Grain15	143	3093061	1.20	0.14	44.26	1.16	134	11		
Grain17	79	1121914	1.20	0.14	9.11	0.53	234	27		Zoned
Grain18	58	1232692	1.30	0.21	29.27	1.23	81	11	transmitted light picture too dark	
Grain19	42	770133	1.14	0.24	7.31	0.36	200	31	transmitted light picture too dark	
Grain21	23	540346	1.20	0.10	7.45	0.30	139	29		
Grain22	4	129656	1.09	0.17	2.63	0.13	95	47		
Grain23	97	1469999	1.26	0.10	14.08	0.57	199	21		
Grain45	9	163656	1.11	0.09	3.41	0.21	92	31		Zoned

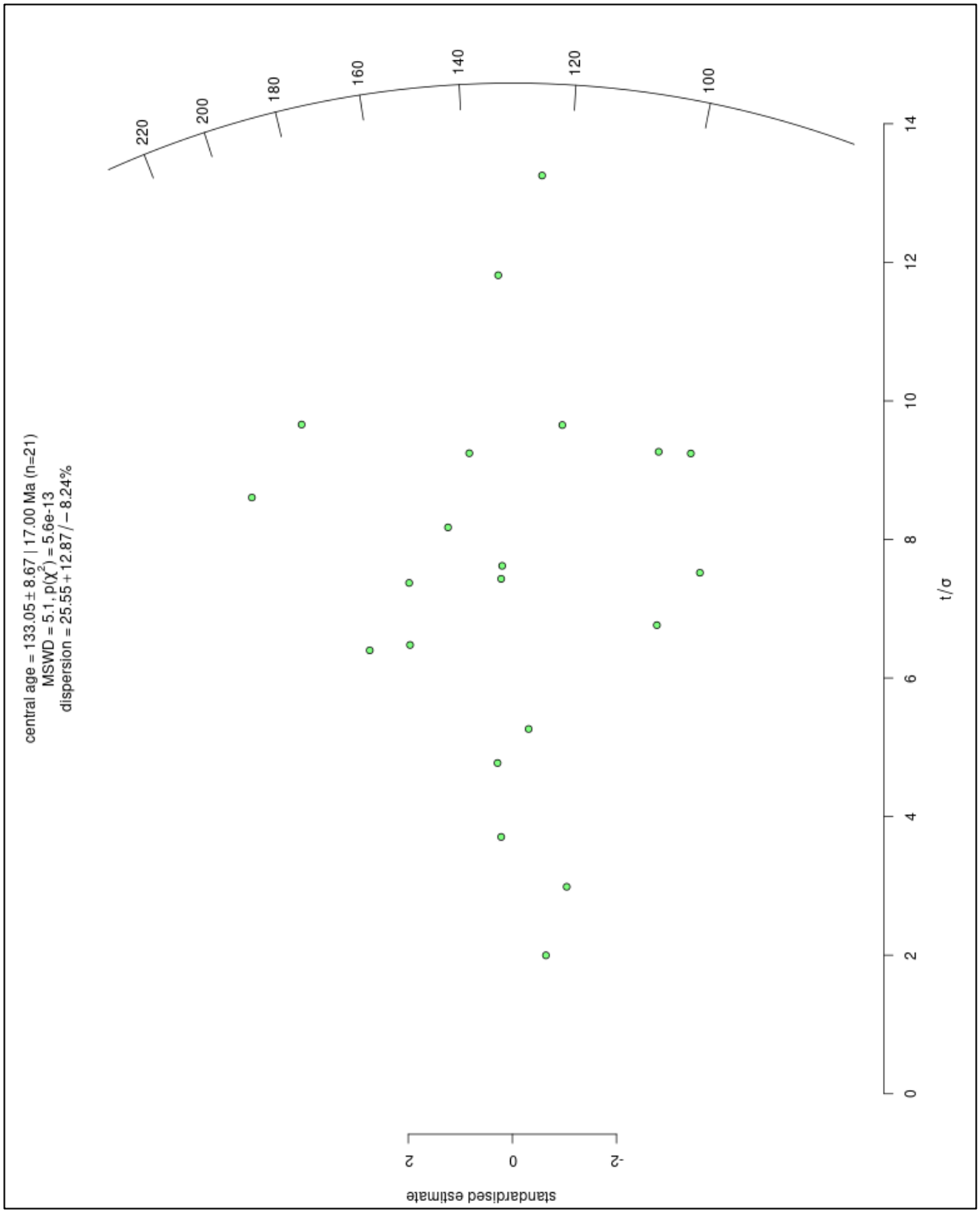

B8.1 Radial plot of single grain ages for the sample (IsoplotR v. 5.0) including the central age. N-number of grains used in calculation. MSWD- Mean Square of the Weighted Deviates. p(x^2)- p-value of a chi-square probability for homogeneity.

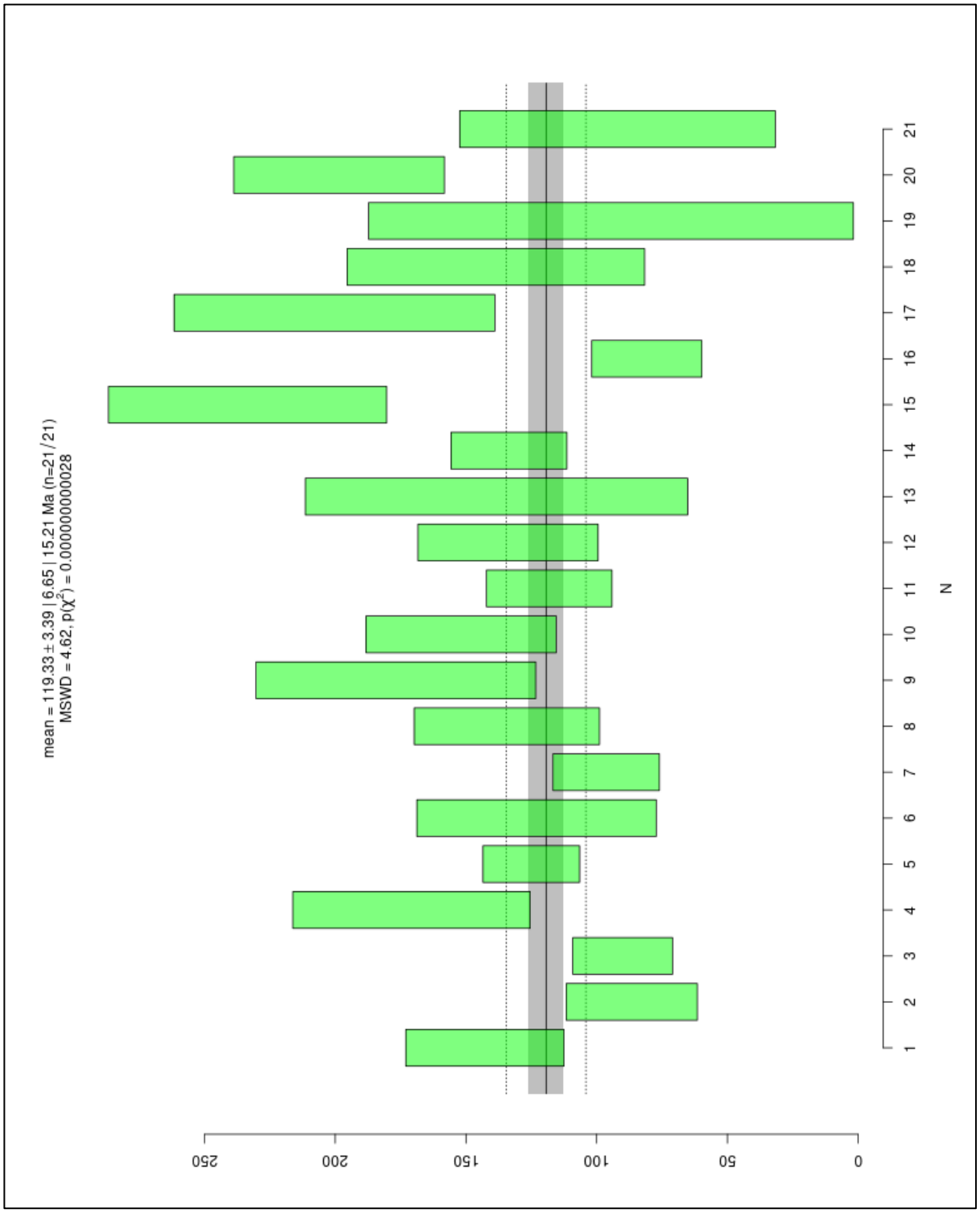

B8.2 Weighted mean plot for the sample (IsoplotR v. 5.0) showing single grain ages including error range. N- number of grains used in calculation/grain number. MSWD- Mean Square of the Weighted Deviates. $p(x^2)$- p-value of a chi-square probability for homogeneity.

C Durango A2 Standard count data

Ns- Number of spontaneous tracks, SD- Standard deviation, t -calculated AFT age (IsoplotR version 5.0). ^{238}U - uranium concentration (LA-ICP-MS)

Sample	Grain no.	Ns	Area [µm^2]	^{238}U [ppm]	2σ (^{238}U]	t [Ma]	1σ(t)
VAH-23	Grain95	67	21536.73	22.38	0.58	26.8	3.3
	Grain96	80	21536.73	22.57	0.60	31.7	3.6
	Grain97	70	21536.73	22.94	0.66	27.3	3.4
	Grain98	69	21536.73	22.40	0.64	27.6	3.4
	Grain99	76	21536.73	22.49	0.60	30.2	3.6
	Grain100	80	21536.73	22.09	0.66	32.4	3.8
	Grain101	69	21536.73	22.80	0.68	27.1	3.4
	Grain102	64	21536.73	22.10	0.65	25.9	3.3
	Grain103	57	21536.73	22.64	0.70	22.5	3.1
	Grain104	64	21536.73	22.54	0.67	25.4	3.3
	Grain105	79	21536.73	22.65	0.75	31.2	3.7
	Grain106	83	21536.73	22.30	0.67	33.3	3.8
	Grain107	69	21536.73	22.15	0.71	27.9	3.5
	Grain108	85	21536.73	22.30	0.73	34.1	3.9
	Grain109	90	21536.73	21.98	0.65	36.6	4.0
	Grain110	77	21536.73	21.84	0.64	31.5	3.7
	Grain111	74	21536.73	21.96	0.67	30.2	3.6
VAH-26	Grain112	69	21536.73	21.91	0.42	28.2	3.4
	Grain113	80	21536.73	22.51	0.45	31.8	3.6
	Grain114	53	21536.73	22.51	0.47	21.1	2.9
	Grain115	72	21536.73	22.49	0.48	28.7	3.4
	Grain116	69	21536.73	22.22	0.48	27.8	3.4
	Grain117	64	21536.73	22.11	0.43	25.9	3.3
	Grain118	50	21536.73	22.31	0.48	20.1	2.9
	Grain119	62	21536.73	22.06	0.45	25.2	3.2
	Grain120	54	21536.73	22.61	0.41	21.4	2.9
	Grain121	54	21536.73	23.48	0.54	20.6	2.8
	Grain122	44	21536.73	23.47	0.51	16.8	2.6
	Grain123	74	21536.73	22.15	0.51	29.9	3.5
	Grain124	60	21536.73	23.30	0.49	23.1	3.0
	Grain125	66	21536.73	23.03	0.52	25.7	3.2
	Grain126	55	21536.73	22.47	0.51	21.9	3.0
	Grain127	83	21536.73	22.23	0.47	33.4	3.7
	Grain128	65	21536.73	22.25	0.50	26.1	3.3
	Grain129	63	21536.73	21.88	0.44	25.8	3.3
VAH-31	Grain130	64	21536.73	22.47	0.43	25.5	3.2
	Grain131	66	21536.73	21.15	0.46	27.9	3.5
	Grain132	63	21536.73	18.76	0.35	30.0	3.8
	Grain133	72	21536.73	19.00	0.39	33.9	4.1

	Grain134	65	21536.73	23.93	0.46	24.3	3.1
	Grain135	59	21536.73	23.45	0.44	22.5	3.0
	Grain136	46	21536.73	23.29	0.55	17.7	2.6
	Grain137	52	21536.73	19.54	0.45	23.8	3.4
	Grain138	58	21536.73	18.96	0.44	27.4	3.7
	Grain139	49	21536.73	22.54	0.53	19.5	2.8
	Grain140	49	21536.73	20.41	0.52	21.5	3.1
	Grain141	61	21536.73	20.43	0.51	26.7	3.5
	Grain142	66	21536.73	23.08	0.60	25.6	3.2
	Grain143	74	21536.73	23.09	0.60	28.7	3.4
	Grain144	50	21536.73	20.04	0.53	22.3	3.2
	Grain145	54	21536.73	20.60	0.51	23.5	3.2
	Grain146	53	21536.73	20.48	0.49	23.2	3.2
	Grain147	64	21536.73	19.80	0.51	28.9	3.7
VAH-42	Grain148	73	21536.73	21.77	0.43	30.0	3.6
	Grain149	67	21536.73	21.27	0.40	28.2	3.5
	Grain150	71	21536.73	21.10	0.41	30.1	3.6
	Grain151	57	21536.73	21.80	0.43	23.4	3.1
	Grain152	69	21536.73	21.34	0.38	28.9	3.5
	Grain153	55	21536.73	21.17	0.43	23.3	3.2
	Grain154	71	21536.73	21.54	0.42	29.5	3.6
	Grain155	68	21536.73	21.45	0.43	28.4	3.5
	Grain156	69	21536.73	21.57	0.45	28.6	3.5
	Grain157	74	21536.73	21.38	0.43	31.0	3.7
	Grain158	68	21536.73	21.35	0.46	28.5	3.5
	Grain159	68	21536.73	21.81	0.51	27.9	3.4
	Grain160	63	21536.73	21.56	0.44	26.2	3.3
	Grain161	66	21536.73	21.56	0.42	27.4	3.4
	Grain162	74	21536.73	21.76	0.51	30.4	3.6
	Grain164	63	21536.73	21.58	0.46	26.1	3.3
	Grain165	72	21536.73	21.72	0.47	29.7	3.6
	Grain166	74	21536.73	21.62	0.43	30.6	3.6
VAH-44_2	Grain167	57	21536.73	21.68	0.41	23.5	3.2
	Grain168	56	21536.73	21.76	0.40	23.0	3.1
	Grain169	56	21536.73	22.14	0.41	22.6	3.1
	Grain170	63	21536.73	21.09	0.44	26.7	3.4
	Grain171	65	21536.73	20.95	0.43	27.8	3.5
	Grain172	75	21536.73	21.91	0.49	30.6	3.6
	Grain173	76	21536.73	18.72	0.47	36.3	4.3
	Grain174	73	21536.73	19.56	0.45	33.4	4.0
	Grain175	55	21536.73	16.20	0.33	30.4	4.1
	Grain176	58	21536.73	17.39	0.42	29.8	4.0
	Grain177	45	21536.73	16.94	0.36	23.8	3.6
	Grain178	50	21536.73	17.13	0.35	26.1	3.7
	Grain179	51	21536.73	15.84	0.35	28.8	4.1

	Grain180	60	21536.73	16.00	0.34	33.5	4.4
	Grain181	58	21536.73	15.57	0.38	33.3	4.5
	Grain182	63	21536.73	16.95	0.36	33.2	4.3
	Grain183	62	21536.73	16.94	0.45	32.7	4.3
	Grain184	58	21536.73	17.21	0.49	30.2	4.1
VAH-48	Grain203	81	21536.73	23.05	0.55	31.4	3.6
	Grain204	66	21536.73	22.56	0.48	26.2	3.3
	Grain205	72	21536.73	22.88	0.48	28.2	3.4
	Grain206	62	21536.73	23.32	0.55	23.8	3.1
	Grain207	70	21536.73	22.51	0.52	27.8	3.4
	Grain208	79	21536.73	21.86	0.47	32.3	3.7
	Grain209	81	21536.73	21.73	0.46	33.3	3.8
	Grain210	77	21536.73	22.03	0.49	31.3	3.6
	Grain211	75	21536.73	22.36	0.45	30.0	3.5
	Grain212	74	21536.73	22.17	0.53	29.9	3.5
	Grain213	61	21536.73	22.78	0.67	24.0	3.2
	Grain214	70	21536.73	22.53	0.54	27.8	3.4
	Grain215	73	21536.73	22.92	0.52	28.5	3.4
	Grain216	56	21536.73	22.72	0.55	22.1	3.0
	Grain217	83	21536.73	22.97	0.50	32.3	3.6
	Grain218	74	21536.73	23.11	0.56	28.7	3.4
	Grain219	55	21536.73	22.62	0.49	21.8	3.0
	Grain220	54	21536.73	22.41	0.52	21.6	3.0
MLM-134	Grain260	66	21536.73	17.68	0.49	33.4	4.2
	Grain261	63	21536.73	19.66	0.62	28.7	3.7
	Grain262	58	21536.73	19.44	0.65	26.7	3.6
	Grain263	62	21536.73	17.52	0.50	31.7	4.1
	Grain265	55	21536.73	17.22	0.41	28.6	3.9
	Grain266	70	21536.73	18.07	0.54	34.6	4.3
	Grain267	70	21536.73	20.71	0.58	30.2	3.7
	Grain268	68	21536.73	20.74	0.56	29.3	3.6
	Grain269	72	21536.73	20.51	0.59	31.4	3.8
	Grain270	62	21536.73	20.65	0.57	26.9	3.5
	Grain271	77	21536.73	20.39	0.54	33.8	4.0
	Grain272	51	21536.73	20.67	0.59	22.1	3.2
	Grain273	53	21536.73	20.87	0.51	22.7	3.2
	Grain274	64	21536.73	20.25	0.63	28.3	3.6
	Grain275	56	21536.73	18.16	0.54	27.6	3.8
VAH-78	Grain299	79	21536.73	21.00	0.49	33.6	3.9
	Grain300	67	21536.73	20.40	0.46	29.4	3.7
	Grain301	68	21536.73	22.21	0.51	27.4	3.4
	Grain302	76	21536.73	23.18	0.63	29.3	3.5
	Grain303	89	21536.73	22.90	0.64	34.8	3.8
	Grain304	76	21536.73	21.56	0.66	31.5	3.7
	Grain305	58	21536.73	19.33	0.66	26.9	3.6

	Grain306	68	21536.73	18.07	0.57	33.7	4.2
	Grain307	73	21536.73	17.37	0.57	37.6	4.6
	Grain308	54	21536.73	17.87	0.59	27.0	3.8
	Grain309	73	21536.73	17.92	0.74	36.4	4.5
	Grain310	61	21536.73	18.36	0.66	29.7	4.0
	Grain311	69	21536.73	18.18	0.68	33.9	4.3
	Grain312	59	21536.73	21.62	0.84	24.4	3.3
	Grain313	55	21536.73	17.96	0.61	27.4	3.8
	Grain317	55	21536.73	18.02	0.68	27.3	3.8
	Grain318	51	21536.73	17.49	0.66	26.1	3.8
	Grain319	55	21536.73	17.78	0.65	27.7	3.9
	Grain320	59	21536.73	17.94	0.57	29.4	3.9
	Grain321	63	21536.73	17.86	0.69	31.6	4.2
	Grain322	60	21536.73	17.81	0.59	30.1	4.0

D LA-ICP-MS analysis

D1 Instrumentation and operational settings for apatite trace element analysis

Laboratory & Sample Preparation	
Laboratory name	Department of Earth Science, University of Bergen
Sample type/mineral	Apatite
Sample preparation	Conventional mineral separation, cold mounting (Epofix) 1 mm thickness, polishing. See chapter 3.1.2 for further details
Imaging	Zeiss Axiolmager Z2m microscope, IDS digital colour camera, highest magnification (1000x)
Laser ablation system	
Make, Model & type	RESOlution M-50 LR with a Coherent COMPexPRO® 110 193 nm ArF excimer laser
Ablation cell & volume	Two volume
Laser wavelength	193 nm
Pulse duration	20 ns
Fluence	2.5 $J.cm^{-2}$
Repetition rate	5 Hz
Blank duration (s)	15
Ablation duration (s)	30
Washout duration (s)	35
Spot diameter	26 µm
Sampling mode/pattern	Static spot ablation/circular
Carrier gas	He (0.75 l/min) with small amounts of N_2 (0.004 ml/min) mixed in before entering the ICP-MS to increase sensitivity.
Signal smoothing device	"Squid" connected between the laser and the ICP-MS
ICP-MS Instrument	
Make, Model & type	Nu Instruments, Nu Attom HR, SC-ICP-MS
Sample introduction	Ablation aerosol from laser ablation
RF power	1300W
Cool gas	Ar 13 l/min
Aux gas	Ar 0.7 l/min
Make-up gas flow	Ar 0.41 l/min
Detection system	MasCom Electron Multiplier
Masses measured	29Si, 43Ca, 147Sm, 232Th, 238U
Integration time per peak/dwell times	98 µs, 121 µs, 237 µs, 209 µs, 208 µs
Number of sweeps per cycle	1
Total time per cycle	0.2 s
Analysis method	FastScan Mode (LinkScan)

IC Dead time	14 ns
Detection Mode	Ion counting mode and ion-attenuated mode
Data Processing	
Calibration strategy	Standard-sample bracketing approach with **NIST612** used as **external standard** (standard values are from the GeoRem database as of 2018-07-09). Durango is used as secondary standard for validation of data.
Data processing package used	Iolite4 (v. 4.4.5) for background subtraction and normalization to an external and internal standard (Paton et al. 2011).
Limit of Detection (LOD)	Calculated with Iolite using Howell et al. (2013).
Data reduction	Trace Elements Next (Longerich et al. 1996).
Internal Standard	43Ca
Blank and instrumental bias correction	Spline_AutoSmooth
Uncertainty level	Reported as 2SE (two standard error) / 2σ
Quality control / Validation	See appendix D2 for secondary standard values.

D2 Quality control / validation

Trace element values of the Durango A2 Standard

LOD -limit of detection, σ-standard error

Sample	Grain no.	Duration [s]	Si29 [ppm] mean	2σ	Sm147 [ppm] mean	2σ	Th232 [ppm] mean	2σ	U238 [ppm] mean	2σ
VAH 23	Grain95	26.17	BelowLOD	5660.95	295.97	6.63	412.35	15.40	22.38	0.58
	Grain96	26.16	BelowLOD	5502.28	294.46	6.52	423.18	10.86	22.57	0.60
	Grain97	26.15	BelowLOD	5691.83	300.15	7.24	421.71	10.07	22.93	0.66
	Grain98	26.15	BelowLOD	5961.08	294.89	6.28	410.81	13.46	22.40	0.64
	Grain99	26.15	BelowLOD	5141.25	293.06	6.35	423.82	10.95	22.49	0.60
	Grain100	26.15	BelowLOD	5203.87	289.40	6.63	411.90	11.92	22.09	0.65
	Grain101	26.15	BelowLOD	5061.71	297.82	6.80	422.62	12.54	22.80	0.68
	Grain102	26.15	BelowLOD	4936.78	294.66	6.53	418.00	11.28	22.10	0.65
	Grain103	26.15	12055.82	4823.16	297.56	7.21	399.07	10.70	22.64	0.70
	Grain104	26.15	BelowLOD	5550.80	298.37	7.93	397.08	10.06	22.54	0.67
	Grain105	26.15	BelowLOD	5084.35	295.43	7.51	416.83	13.57	22.65	0.75
	Grain106	26.15	BelowLOD	6440.71	298.45	6.90	401.52	10.81	22.30	0.67
	Grain107	26.15	13696.11	5800.21	291.76	6.87	403.15	13.70	22.15	0.71
	Grain108	26.05	BelowLOD	6758.79	294.15	7.46	400.30	12.05	22.29	0.73
	Grain109	26.16	10013.20	4403.81	292.75	6.35	385.84	9.99	21.98	0.65
	Grain110	26.15	BelowLOD	5683.76	292.88	7.18	365.59	10.60	21.84	0.64
	Grain111	26.15	BelowLOD	4759.94	291.37	7.21	397.04	11.96	21.96	0.67
	Group Stats		2857.18	2794.72	294.89	1.41	406.52	7.47	22.36	0.15
	Reference Values		1246.81	279.96	237.15	43.12	210.17	65.88	15.24	6.20
VAH 26	Grain112	26.15	BelowLOD	4760.90	291.50	5.33	381.03	13.02	21.91	0.42
	Grain113	26.16	BelowLOD	5170.56	296.38	5.28	406.02	13.99	22.51	0.45
	Grain114	26.15	BelowLOD	5740.24	295.29	5.01	422.79	9.70	22.51	0.47
	Grain115	26.15	BelowLOD	5329.04	297.00	5.97	414.22	12.13	22.48	0.48
	Grain116	26.15	BelowLOD	5452.35	294.12	5.58	411.38	8.38	22.22	0.48
	Grain117	26.15	BelowLOD	5659.32	296.03	5.31	426.45	9.68	22.11	0.43
	Grain118	26.15	BelowLOD	5547.29	299.18	4.75	410.16	7.74	22.31	0.48
	Grain119	26.15	BelowLOD	5002.64	299.65	5.74	412.60	7.83	22.06	0.45
	Grain120	26.15	BelowLOD	4688.12	249.75	4.12	408.41	8.36	22.61	0.41
	Grain121	26.06	12763.50	5285.99	245.16	4.54	429.53	9.76	23.48	0.54
	Grain122	26.05	BelowLOD	4823.58	251.59	3.96	422.81	9.14	23.47	0.51
	Grain123	26.15	BelowLOD	5715.31	243.38	5.05	414.10	9.69	22.15	0.51
	Grain124	26.15	BelowLOD	4676.39	246.59	4.38	420.66	9.22	23.30	0.49
	Grain125	26.15	BelowLOD	4579.41	242.86	4.75	429.14	11.20	23.03	0.52
	Grain126	26.15	11048.93	4371.18	245.65	4.00	415.95	8.47	22.47	0.51
	Grain127	26.15	21705.98	4138.67	244.77	4.86	401.59	8.72	22.23	0.47
	Grain128	26.15	BelowLOD	5210.66	228.36	4.55	414.68	8.44	22.25	0.50
	Grain129	26.15	15481.72	4620.58	226.34	4.02	402.76	9.07	21.88	0.44
	Group Stats		5676.61	3011.17	266.31	13.28	413.57	5.50	22.50	0.24
VAH 31	Grain130	26.15			240.61	4.65	427.37	8.51	22.47	0.43
	Grain131	26.15			224.12	4.19	412.77	7.96	21.15	0.46
	Grain132	26.15			213.63	3.98	380.96	7.64	18.76	0.35
	Grain133	26.15			212.32	3.91	376.19	7.77	19.00	0.39
	Grain134	26.06			251.08	5.02	437.28	10.15	23.93	0.46

	Grain135	26.17			235.84	4.15	431.66	9.37	23.45	0.44
	Grain136	26.16			245.56	4.25	426.01	9.52	23.29	0.55
	Grain137	26.16			219.92	4.91	392.30	8.91	19.54	0.45
	Grain138	26.15			218.62	4.79	379.11	8.55	18.96	0.44
	Grain139	26.17			234.26	4.50	415.04	10.47	22.54	0.53
	Grain140	26.05			222.58	4.39	403.17	10.31	20.41	0.52
	Grain141	26.15			220.25	4.18	400.69	10.02	20.43	0.51
	Grain142	26.15			237.61	5.13	440.00	11.98	23.08	0.60
	Grain143	26.15			244.00	5.56	427.84	11.54	23.09	0.60
	Grain144	26.15			220.85	4.54	394.51	10.45	20.04	0.53
	Grain145	26.15			225.82	4.27	409.12	10.43	20.60	0.51
	Grain146	26.16			224.72	4.92	402.02	8.41	20.48	0.49
	Grain147	26.15			221.97	4.26	396.50	9.60	19.80	0.51
	Group Stats				228.54	5.43	408.48	9.47	21.17	0.82
	Reference Values				237.15	43.12	210.17	65.88	15.24	6.20
VAH 42	Grain148	26.15	BelowLOD	5094.12	233.03	4.85	420.25	7.52	21.77	0.43
	Grain149	26.15	BelowLOD	4505.60	239.57	4.11	402.94	6.93	21.27	0.40
	Grain150	26.15	BelowLOD	4471.01	240.19	4.45	401.87	6.99	21.10	0.41
	Grain151	26.16	BelowLOD	4329.13	245.89	3.81	417.52	7.57	21.80	0.43
	Grain152	26.15	BelowLOD	4757.78	238.74	3.89	408.16	7.28	21.34	0.38
	Grain153	26.05	BelowLOD	4646.49	244.07	4.22	419.66	7.78	21.17	0.43
	Grain154	26.15	BelowLOD	4419.88	243.58	4.74	418.95	8.39	21.54	0.42
	Grain155	26.15	BelowLOD	4812.50	245.27	4.44	423.56	7.87	21.45	0.43
	Grain156	26.15	BelowLOD	4749.36	249.39	4.28	412.21	9.14	21.57	0.45
	Grain157	26.15	BelowLOD	4392.14	242.66	4.18	411.53	8.78	21.38	0.43
	Grain158	26.15	BelowLOD	5292.63	241.86	4.31	414.93	7.62	21.35	0.46
	Grain159	26.16	BelowLOD	4625.47	244.60	4.31	423.14	7.90	21.81	0.51
	Grain160	26.15	BelowLOD	5153.09	251.76	4.21	428.45	8.16	21.56	0.44
	Grain161	26.18	BelowLOD	4687.73	241.44	4.16	419.78	7.41	21.56	0.42
	Grain162	26.15	BelowLOD	4691.36	245.69	4.10	414.77	7.63	21.76	0.51
	Grain164	26.15	BelowLOD	4113.48	248.09	4.75	418.57	9.35	21.58	0.46
	Grain165	26.15	BelowLOD	5170.07	249.17	4.77	419.00	9.08	21.72	0.47
	Grain166	26.05	BelowLOD	4237.06	249.74	4.57	412.85	7.99	21.62	0.43
	Group Stats		1860.99	1200.29	244.15	2.20	416.01	3.26	21.52	0.10
	Reference Values		1246.81	279.96	237.15	43.12	210.17	65.88	15.24	6.20
VAH 44_2	Grain167	26.15	BelowLOD	8587.99	249.78	4.51	424.42	8.73	21.68	0.41
	Grain168	26.16	BelowLOD	7998.07	249.74	4.53	420.58	8.04	21.76	0.40
	Grain169	26.05	BelowLOD	9157.63	253.86	4.33	428.07	8.78	22.14	0.41
	Grain170	26.16	BelowLOD	8507.32	242.78	4.92	409.46	9.70	21.09	0.44
	Grain171	26.15	BelowLOD	8071.79	245.93	4.66	407.44	8.86	20.95	0.43
	Grain172	26.05	BelowLOD	9333.36	253.11	4.75	420.80	9.44	21.91	0.49
	Grain173	26.06	BelowLOD	7955.20	245.26	4.03	356.30	8.46	18.72	0.47
	Grain174	26.15	BelowLOD	8147.53	241.94	4.88	376.15	9.98	19.56	0.45
	Grain175	26.15	BelowLOD	7220.64	243.72	4.56	330.46	7.59	16.20	0.33
	Grain176	26.17	BelowLOD	6847.26	246.31	4.87	346.72	8.69	17.39	0.42
	Grain177	26.15	BelowLOD	7034.65	238.41	4.22	341.96	7.99	16.94	0.36
	Grain178	26.15	BelowLOD	7087.66	241.65	4.91	350.53	9.00	17.13	0.35
	Grain179	26.15	BelowLOD	6576.18	247.46	5.45	322.59	8.23	15.84	0.35
	Grain180	26.15	BelowLOD	6789.89	250.47	4.62	329.08	8.44	16.00	0.34

	Grain181	26.06	BelowLOD	6339.93	249.09	4.74	321.78	7.87	15.57	0.38
	Grain182	26.16	BelowLOD	6284.53	248.36	4.97	340.95	8.67	16.95	0.36
	Grain183	26.15	BelowLOD	6392.62	249.40	5.56	339.35	10.12	16.94	0.45
	Grain184	26.15	BelowLOD	6990.05	257.15	6.29	338.02	10.09	17.21	0.49
	Group Stats				247.47	2.24	366.92	18.72	18.56	1.14
	Reference Values				237.15	43.12	210.17	65.88	15.24	6.20
VAH 48	Grain203	26.15	BelowLOD	5569.80	277.71	6.63	418.25	16.89	23.05	0.55
	Grain204	26.15	BelowLOD	5383.17	273.36	5.42	405.12	16.59	22.56	0.48
	Grain205	26.15	BelowLOD	5715.20	268.39	4.39	384.98	14.00	22.88	0.48
	Grain206	26.15	BelowLOD	5598.45	279.84	5.68	410.23	14.89	23.32	0.55
	Grain207	26.15	BelowLOD	5223.18	261.77	4.89	410.09	12.28	22.51	0.52
	Grain208	26.15	BelowLOD	5368.78	257.98	5.04	399.82	13.08	21.86	0.47
	Grain209	26.15	BelowLOD	5067.71	254.94	4.45	413.28	11.63	21.73	0.46
	Grain210	26.15	BelowLOD	5530.32	258.52	4.43	412.12	13.18	22.03	0.49
	Grain211	26.15	BelowLOD	5069.86	263.10	4.84	415.12	14.67	22.36	0.45
	Grain212	26.16	BelowLOD	5029.31	258.59	4.99	412.43	13.18	22.17	0.53
	Grain213	26.16	BelowLOD	5627.26	265.85	5.63	431.93	9.91	22.78	0.67
	Grain214	26.15	BelowLOD	5498.71	257.23	4.61	394.95	14.38	22.53	0.54
	Grain215	26.16	BelowLOD	4732.42	270.92	4.90	438.57	16.96	22.92	0.52
	Grain216	26.16	BelowLOD	4640.10	265.94	5.13	401.81	14.74	22.72	0.55
	Grain217	26.15	BelowLOD	5471.94	267.66	4.76	415.63	14.02	22.97	0.50
	Grain218	26.15	BelowLOD	4606.11	273.93	5.36	428.29	13.11	23.11	0.56
	Grain219	26.15	BelowLOD	5169.14	279.22	5.49	431.91	18.01	22.62	0.49
	Grain220	26.20	BelowLOD	5478.10	262.54	4.73	418.21	10.06	22.41	0.52
	Group Stats		BelowLOD	2751.25	266.53	3.72	413.49	6.42	22.58	0.21
	Reference Values				237.15	43.12	210.17	65.88	15.24	6.20
MLM 134	Grain260	25.88	BelowLOD	13672.36	288.88	6.83	375.83	10.35	17.68	0.49
	Grain261	25.62	BelowLOD	13260.55	319.45	8.91	418.18	12.76	19.66	0.62
	Grain262	26.05	BelowLOD	10988.15	307.54	8.54	414.25	14.61	19.44	0.65
	Grain263	26.15	BelowLOD	13690.75	284.99	7.81	359.19	10.96	17.52	0.50
	Grain265	26.15	BelowLOD	13035.80	284.74	6.59	341.28	8.27	17.22	0.41
	Grain266	26.07	BelowLOD	11399.31	294.29	6.98	357.06	11.05	18.07	0.54
	Grain267	26.05	BelowLOD	6498.61	295.13	6.72	381.83	10.99	20.71	0.58
	Grain268	26.15	BelowLOD	7582.08	286.83	7.43	388.66	10.28	20.74	0.56
	Grain269	26.15	BelowLOD	7712.71	279.52	6.84	381.88	11.30	20.51	0.59
	Grain270	26.15	BelowLOD	9068.31	288.13	6.71	371.67	11.35	20.65	0.57
	Grain271	26.15	BelowLOD	7972.16	290.57	7.10	388.99	12.09	20.39	0.54
	Grain272	26.15	BelowLOD	8327.12	287.46	6.70	390.13	12.63	20.67	0.59
	Grain273	26.15	BelowLOD	8234.01	289.51	6.16	366.87	11.60	20.87	0.51
	Grain274	26.06	BelowLOD	8065.56	288.56	6.91	378.42	13.29	20.25	0.63
	Grain275	26.20	BelowLOD	7035.22	293.90	6.83	351.64	10.83	18.16	0.54
	Group Stats				291.97	5.10	377.73	10.99	19.50	0.71
	Reference Values				237.15	43.12	210.17	65.88	15.24	6.20
VAH 78	Grain299	26.05	BelowLOD	9902.20	289.91	5.83	397.93	7.85	21.00	0.49
	Grain300	26.15	BelowLOD	10585.37	285.73	6.58	382.66	8.05	20.40	0.46
	Grain301	26.15	BelowLOD	11465.80	291.78	5.75	423.93	8.70	22.21	0.51
	Grain302	26.15	BelowLOD	9485.34	303.56	7.78	454.65	10.99	23.18	0.63
	Grain303	26.15	BelowLOD	9969.04	300.16	6.57	445.18	11.26	22.90	0.64

	Grain304	26.06	BelowLOD	10323.48	298.66	7.53	420.57	11.97	21.56	0.66
	Grain305	26.16	BelowLOD	11149.23	311.27	8.80	387.43	12.98	19.33	0.66
	Grain306	26.07	BelowLOD	9956.38	289.47	7.56	364.66	10.77	18.07	0.57
	Grain307	26.15	BelowLOD	9333.04	281.17	7.37	364.93	11.44	17.37	0.57
	Grain308	26.15	BelowLOD	11339.31	282.87	7.09	369.76	12.56	17.87	0.59
	Grain309	26.06	BelowLOD	7786.05	281.71	9.48	372.43	14.72	17.92	0.74
	Grain310	26.09	BelowLOD	10588.07	283.89	8.17	381.96	14.22	18.36	0.66
	Grain311	26.06	BelowLOD	10938.87	280.30	8.44	379.84	14.38	18.18	0.68
	Grain312	26.16	BelowLOD	10470.86	300.06	8.40	441.79	16.02	21.62	0.84
	Grain313	26.15	BelowLOD	8610.68	268.93	7.17	371.67	13.45	17.96	0.61
	Grain317	26.15	BelowLOD	7189.72	270.80	8.55	362.94	13.20	18.02	0.68
	Grain318	26.06	BelowLOD	7454.57	267.92	8.74	366.30	15.52	17.49	0.66
	Grain319	26.08	BelowLOD	7552.77	274.52	8.25	371.57	14.57	17.78	0.65
	Grain320	26.06	BelowLOD	5964.56	281.10	8.44	373.20	13.95	17.94	0.57
	Grain321	26.06	BelowLOD	5927.94	282.53	9.12	373.91	15.39	17.86	0.69
	Grain322	26.16	BelowLOD	5806.73	289.64	9.36	369.79	13.21	17.81	0.59
	Group Stats				286.48	5.05	389.39	12.79	19.28	0.86
	Reference Values				237.15	43.12	210.17	65.88	15.24	6.20

E Structural field data

(Table starting on next page)
Columns from left to right using abbreviations: Outcrop number, locality ID, coordinates (longitude, latitude), lithology, foliation (dip direction, dip), fractures (dip direction, dip), slicken fibre/slickenlines (trend, plunge), mineral (slicken fibre mineralogy), quality/clarity (Q) of the slicken fibre orientation/slickenlines (3 very good, 1 very vague), interpreted kinematics, certainty (C) of the kinematic interpretation (3 certain, 1 uncertain), defined kinematics based on >45° pitch of slicken fibers: dip-slip (normal/reverse), <44° pitch of lineation: strike-slip (sinistral/dextral), selected notes from the field book. The question marks in the "mineral" and "notes" columns indicate uncertainty.

Division in subregions is indicated through colour-coding: 0: no colour, 1: purple, 2: grey, 3: green, 4: red, 5: orange, 6: pink, 7: yellow, 8: blue. For more information see section 4.3.3 and 4.3.4.

*here: Bedding measurement, not foliation

Outcr. no.	Loc. ID	Coordinates [DD]		Lithology	Foliation		Fractures		Slicken fibers		Mineral	Q	Kin.	C	Def. kin.	Notes
					Dip dir.	Dip	Dip dir.	Dip	Trend	Plunge						
1.1	1a	5.19861	61.71972	Sandstone	041*	15*	265	76	189	32	Calcite	1	sinistral, normal	1	sinistral	Hornelen
1.2	2a	5.94028	61.74944	Augengneiss	250	15	73	64					dextral	1		
	2b	5.94028	61.74944				80	71								
	2c	5.94028	61.74944				59	59								
	2d	5.94028	61.74944				50	75								
1.3	3a	6.05333	61.83056	Diorite? Gneiss	171	30	290	80	201	25	Chlorite, Epidote, Quartz?	2	sinistral, normal	2	sinistral	
	3b	6.05333	61.83056				281	70	202	26	Chlorite, Epidote, Quartz?	2	sinistral, normal	2	sinistral	
1.4	4a	5.99694	61.82889	Gneiss			56	88	142	16	Chlorite, Epidote	1	sinistral, normal	1	sinistral	
	4b	5.99694	61.82889				71	83			Chlorite, Epidote					
	4c	5.99694	61.82889				250	90								
	4d	5.99694	61.82889				72	78								
1.5	5a	5.98111	61.79056	Augengneiss	172	35	138	55	220	5	Chlorite, Epidote	2	sinistral	2	sinistral	
2.1	6a	5.57306	61.67389	Gneiss	290	18										Top to W (290)
	6b	5.57306	61.67389	Paragneiss	13	46										Further up street
	6c	5.57306	61.67389		8	50										
	6d	5.57306	61.67306		355	49										Ductile kin.: Top to W (296/35)
	6e	5.57306	61.67306		10	65	266	85								
	6f	5.57306	61.67306				267	80								
2.2	7a	5.55528	61.66472	Altered Anorthosite?	186	20	279	88								
2.3	8a	5.53028	61.65972	Gneiss	194	64	110	90								

	8b	5.53028	61.65972				190	69								
2.4	9a	5.3775	61.6431	Gneiss	17	12	220	89	130	18	Epidote?	1	sinistral, normal	1	sinistral	Uncertain about kinematics
	9b	5.3775	61.6431				244	80	162	8	Epidote, Zeolite?, Chlorite, Fe	1	dextral	1	dextral	
	9c	5.3775	61.6431				238	80	152	3	Epidote, Zeolite?, Chlorite, Fe	1	dextral	1	dextral	
	9d	5.3775	61.6431				252	85	339	26	Chlorite, Epidote, Zeolite?	2	dextral, normal	1	dextral	possibly younger sinistral kinematics, Zeolite on top without lineation
	9e	5.3775	61.6431				250	58	304	44	Chlorite, Epidote, Zeolite?	1	dextral, normal	1	normal	
	9f	5.3775	61.6431				243	76	320	36	Chlorite, Epidote, Zeolite?	1	dextral, normal	1	dextral	
	9g	5.3775	61.6431				255	85			Epidote?					
	9h	5.3775	61.6431				251	75			Epidote?					
Kyst muse et	10a	5.0430	61.5891	Gneiss	350	25										
2.5	11a	5.5522	61.5892	Mylonite	22	40	302	80	34	0	Chlorite	1	sinistral	2	sinistral	
	11b	5.5522	61.5892				310	86	33	11	Chlorite	2	sinistral, normal	2	sinistral	
2.6	12a	5.5536	61.6033	Paragneiss	347	51	6	70	8	70	Chlorite	1	normal	1	normal	Very unsure, difficulties with Riedel structures. Possibly a younger strike-slip direction on top (?)
	12b	5.5536	61.6033				356	65	10	60	Chlorite	1	normal	1	normal	
3.1	13a	4.8869	61.7861	Granodiorite			134	75								
	13b	4.8869	61.7861				110	75								

	13c	4.8869	61.7861				103	80								
	13d	4.8869	61.7861				52	88								
3.2	14a	4.9128	61.7756	Granodiorite			268	85								
	14b	4.9128	61.7756				88	80								
	14c	4.9128	61.7756				251	85								
	14d	4.9128	61.7756				4	66			Epidote					
	14e	4.9128	61.7756				356	52			Epidote					
	14f	4.9128	61.7756				350	50			Epidote					
	14g	4.9128	61.7756				350	45			Epidote					
	14h	4.9128	61.7756				354	54			Epidote					
	14i	4.9128	61.7756				0	56			Epidote					
	14j	4.9128	61.7756				356	50			Epidote					
	14k	4.9128	61.7756				356	44			Epidote					
	14l	4.9128	61.7756				350	42	267	15	Epidote	1	sinistral	2	sinistral	
	14m	4.9128	61.7756				0	70					normal	3		Offset can be seen (about 30 cm), cut orthogonal to fault plane
	14n	4.9128	61.7756				261	73	180	10	only host?	2	sinistral	3	sinistral	
3.3	15a	4.9272	61.7708	Granodiorite			352	85	264	25	Epidote, Quartz?	1	sinistral	1	sinistral	
	15b	4.9272	61.7708				160	90	71	5	Epidote	1	sinistral	1	sinistral	
	15c	4.9272	61.7708				40	83			Epidote?, Quartz/Zeolite, black brownish mineral?					
	15d	4.9272	61.7708				284	73								
	15e	4.9272	61.7708				358	76								
	15g	4.9272	61.7708				8	71	98	20	Chlorite, Epidote?	1	sinistral	1	sinistral	Trend/Plunge estimated!
	15h	4.9272	61.7708				20	75								

	15i	4.9272	61.7708				166	89	258	10	Chlorite, Epidote?	1	dextral	1	dextral	Very weak lineation
4.1	16a	5.5772	62.0047	Peridotite			260	54	208	44	Chlorite, talc?	3	normal	2	normal	
	16b	5.5772	62.0047				171	70	266	20	Quartz?/ Zeolite?	2	sinistral	2	sinistral	
	16c	5.5778	62.0050				161	60	250	10	Chlorite, Epidote/ Olivine?, Calcite	2	sinistral, normal	2	sinistral	Along foliation (?)
	16d	5.5778	62.0050				316	35	238	15		2	sinistral, normal	2	sinistral	
	16e	5.5778	62.0050				176	70	262	30		2	sinistral, reverse	2	sinistral	
	16f	5.5778	62.0050				122	50	50	5		1	sinistral	2	sinistral	Possibly along foliation?
	16g	5.5778	62.0050				196	55	286	35		2	sinistral	1	sinistral	Insecure, very irregular
	16h	5.5778	62.0050				192	60	280	30		2	sinistral, normal	2	sinistral	
	16i	5.5778	62.0050				90	65	2	25		2	dextral, normal	1	dextral	Curved, along foliation?
	16j	5.5778	62.0050				88	59	348	20		2	dextral, normal	1	dextral	Curved, along foliation?
	16k	5.5778	62.0050				80	52	352	20		2	dextral, normal	2	dextral	
	16l	5.5778	62.0050				234	85	154	55	Chlorite? (very dark)	1	sinistral, normal	1	normal	
	16m	5.5778	62.0050				320	63	284	60		1	normal	2	normal	Wavy
	16n	5.5778	62.0050				354	45	52	30						Difficult fracture plane, originally normal fault?, mineral growth showing reverse fault? Very unsure
4.2	17a	5.5744	62.0158	Foliated Peridotite	158	65	248	73			Mucovite?					Muscovite growing on top, younger

	17b	5.5744	62.0158				240	65	234	70	Chlorite, Epidote?	3	normal	3	normal	
	17c	5.5744	62.0158				174	85	258	35	Chlorite, Epidote, Zeolite?	3	dextral, normal	3	dextral	
	17d	5.5744	62.0158				264	75	215	60	Chlorite	2	normal	2	normal	
4.3	18a	5.3869	62.0519	Gneiss	140	75	220	40								
5.1	19a	5.5064	61.9319	Peridotite			230	60	278	55	Serpentine, Talc, Soapstone? (pink)	1	reverse	1	reverse	Lefdal data mine
	19b	5.5064	61.9319				165	33								could be foliation?
	19c	5.5064	61.9319				228	60	284	50	Talc? Fibrous	1	normal	1	normal	
	19d	5.5064	61.9319				258	80	330	35	Serpentine, Talc?	2	sinistral, reverse	2	sinistral	
	19e	5.5064	61.9319				262	75	346	10	Chlorite, Serpentine, Soapstone?	3	sinistral	3	sinistral	
5.2	20a	5.5567	61.9231	Gneiss	59	43	71	80								
	20b	5.5567	61.9231		12	50	28	75								
5.3	21a	5.6658	61.9161	Gneiss	138	83	138	80	52	28	Serpentine(?), Epidote, Chlorite, Zeolite?	1	sinistral, normal	1	sinistral	
	21b	5.6658	61.9161				138	80	50	25	Serpentine(?), Epidote, Chlorite, Zeolite?	3	sinistral, normal	3	sinistral	
5.4	22a	6.2056	61.9069	Gneiss	145	75	148	70								

	22b	6.2056	61.9069				252	65	338	15	Epidote, Chlorite	1	sinistral, normal	1	sinistral	Gorge, tiny fracture plane inside/parallel gorge measured
	22c	6.2056	61.9069		148	75	218	70					(sinistral)			No mineralisation, Riedel
	22d	6.2050	61.9069				122	80	214	50	Epidote, Chlorite, Zeolite?	1	normal, sinistral	1	normal	
	22e	6.2050	61.9069				254	65	216	60	Epidote	1	normal, sinistral	1	normal	
	22f	6.2050	61.9069				260	70	202	55	Epidote	1	normal, (sinistral)	1	normal	
	22g	6.2050	61.9069				310	65	240	35	Epidote	2	sinistral, normal	2	sinistral	
	22h	6.2050	61.9069				122	85	208	43	Epidote	1	dextral	1	dextral	
	22i	6.2050	61.9069				158	85								
5.5	23a	6.4956	61.9378	Gneiss	6	55	316	80			Barite?					Quarry, AFT+UPB Calcite loc. but no Calcite found
	23b	6.4956	61.9378				246	85			Barite?					
5.6	24a	6.1969	61.9078	Gneiss	156	85	234	80			Quartz? Tiny white crystals					
	24b	6.1969	61.9078				156	85	246	16	Chlorite?	2	sinistral, normal	2	sinistral	
	24c	6.1969	61.9078				336	87	246	20	Chlorite?	2	sinistral, normal	2	sinistral	Same plane as measurement before, plane is wavy around 90° dip
	24d	6.1969	61.9078				160	75	248	18	Chlorite?	2	sinistral, normal	2	sinistral	
5.7	25a	5.8500	61.9189	Flaser-Gneiss			330	82	60	20	? Chlorite again?	2	sinistral, normal	2	sinistral	
	25b	5.8500	61.9189				332	85	63	5	Lination in host?	1	sinistral	2	sinistral	
5.8	26a	5.1947	61.9242	Gneiss			244	65	330	10	Epidote, Chlorite	1	dextral	1	dextral	Quarries Magnar

	26b	5.1947	61.9242				248	60			Epidote, Chlorite					
	26c	5.1947	61.9242				238	48			Epidote, Chlorite					
	26d	5.1947	61.9242				240	51			Epidote, Chlorite					
5.9	27a	5.2847	61.9119	Gneiss	0	60	265	80	350	52	Zeolite? Quartz?	1	normal	1	normal	uncertain
	27b	5.2847	61.9119				3	75	270	10	? Mint green/ black + whitish/brownish	1	dextral	1	dextral	
5.10	28a	5.4597	61.9269		333	82	333	82			Mica, Zeolite?		sinistral?			Foliation parallel
6.1	29a	5.7300	61.8653	Gneiss	332	65	332	65			Chlorite		sinistral			Foliation parallel, slickenside trend too weak to measure
	29b	5.7283	61.8647		326	55	326	55	248	5	Chlorite	1	sinistral	3	sinistral	Difficult measurement of slicken fibre lineation
	29c	5.7283	61.8647				330	62	64	10	Chlorite	2	sinistral	2	sinistral	
6.2	30a	5.6317	61.8936	Gneiss	314	80	308	70	42	10	Epidote? (no lineation: Actinolite/Zeolite?)	2	sinistral	2	sinistral	
	30b	5.6317	61.8936				305	70	35	15	Epidote? (no lineation: Actinolite/Zeolite?)	1	sinistral	1	sinistral	
	30c	5.6317	61.8936				102	88	191	15	Chlorite?	1	sinistral	1	sinistral	

	30d	5.6317	61.8936				314	80	44	10	Epidote	1	sinistral	1	sinistral	Lowest mineral (older) very unsure about kinematic
	30e	5.6317	61.8936				300	6	218	5	Chlorite? (Black)	1	sinistral	1	sinistral	Same surface as previous measurement, mineralization seems to be on top (?) (younger)
6.3	31a	5.4169	61.9150	Gneiss/Eclogite	133	53	36	55	96	35	Muscovite	1	sinistral, reverse	1	sinistral	Eclogite fold
6.4	32a	5.3786	61.9044	Gneiss			160	80			Muscovite		reverse?			
	32b	5.3786	61.9044				154	80								also Phengite (UHP) growing on small surface (?)
6.5	33a	5.3661	61.8992	Gneiss	354	70	104	75			Epidote, Zeolite?					"Outcrop: Big wall", very few mineralizations
	33b	5.3661	61.8992				86	80			Epidote, Zeolite?		reverse?			
6.6	34a	5.3828	61.8481		182	80	80	65			Chlorite, Epidote		sinistral, reverse?			
	34b	5.3828	61.8481				250	90								
	34c	5.3828	61.8481				63	55	123	35	Chlorite, Epidote?	1	sinistral	1	sinistral	Difficult trend measurement, measured on field book. Transfomed via Schmidt net (Original measurement of lineation: 182/60 (reverse)).
	34d	5.3828	61.8481				290	75								
	34e	5.3828	61.8481				240	70	252	70	Chlorite, Epidote?					
	34f	5.3828	61.8481		168	90	70	85								
6.7	35a	5.3128	61.8700	Gneiss/Eclogite	352	50	82	80	352	55	Chlorite	2	reverse, dextral	2	reverse	
	35b	5.3128	61.8700				242	75	308	60	Chlorite, Epidote, Zeolite? Or Quartz?	2	normal, dextral	2	normal	

	35c	5.3128	61.8700				250	65	276	65		1	normal	1	normal	
	35d	5.3128	61.8700				240	75	290	65	Chlorite	1	normal	1	normal	
	35e	5.3128	61.8700				84	85	350	75	Chlorite	3	reverse, dextral	3	reverse	
	35f	5.3128	61.8700				250	80	338	40		1	dextral, normal	1	dextral	
	35g	5.3128	61.8700				244	85	310	75	Chlorite	3	normal, dextral	3	normal	
	35h	5.3103	61.8697	Gneiss			250	75	322	55	Chlorite, Epidote	2	normal, dextral	1	normal	
1.1	36	6.7181	61.8680	Gneiss	163	40	246	64	348	2	Chlorite, Zeolite?, Fe,Epidote?	1	dextral	1	dextral	uncertain
1.2	37	6.5636	61.8289	Augengneiss			256	90								big
	38	6.5636	61.8289				78	80								smaller
1.3	39	6.5436	61.8181	Gneiss	240	10	278	86			Epidote, Zeolite?, purple crystals?					assumed sinistral
	40	6.5436	61.8181				283	90			Epidote					
1.4	41	6.4956	61.7922	Gneiss	206	20	247	86			Zeolite?radial growing minerals/ pink-red/white					some edges, but no lineation (sinistral, 0°dip - that would be around 157/00 trend/plunge)
2.1	42	5.4578	61.5928	Gneiss/ Mylonite	338	16										no mineralisations, not really any measurable fractures
2.2	43	5.4839	61.5853	darker Gneiss/ Mylonite	345	20	96	86	9	15	Chlorite, Fe, Pyrite	1	dextral	1	dextral	lineation seems parallel to foliation
	44	5.4839	61.5853				112	20								

2.3	45	5.4794	61.5869	dark Gneiss same as 2.2, finer foliation	336	20	127	70	60	45	Chlorite, Fe, Pyrite	2	sinistral, normal	2	normal	small, two of these
	46	5.4794	61.5869				310	66	246	55	Chlorite, Fe, Zeolite?	2	sinistral, normal	2	normal	2-3 m in size, cuts the smaller fractures
	47	5.4794	61.5869				255	90								6 m, very weathered, several of these
2.4	48	5.5144	61.5744	Gneiss	355	11	130	90	214	20	white Zeolite?, Chlorite	1	sinistral	2	sinistral	Climbing during measurement
2.5	49	5.5350	61.5750	Gneiss	27	53	132	90	48	14	white Zeolite?, Chlorite	3	sinistral	3	sinistral	Many small fractures like this one
2.6	50	5.5592	61.6089	Light/ pinkish Gneiss	325	24	180	60	260	15	white+ pink Zeolite?, Epidote, some black spots	3	sinistral	3	sinistral	
2.7	51	5.6333	61.6172	Light/pinkis h Gneiss	299	30	113	80								Several of these, without mineralisation
2.8	52	5.6914	61.6183	dark red Gneiss/ Augengneiss	6	26	282	85								Several, some with Chloride, some without mineralisation
3.1	53	5.7217	61.6344	Gneiss white/pinkis h mica rich	231	18	255	85	162	6	white/yel lowish min.	1	dextral	1	dextral	Very insecure! Almost no lineation visible
	54	5.7217	61.6344				260	86								
3.2	55	5.7269	61.6364	Gneiss white/pinkis h mica rich same as 3.1	43	20	336	85			white Zeolite?					no lineation, but seems sinistral

	56	5.7269	61.6364				200	85								
3.3	57	5.7335	61.6395	Contact Gneiss 3.2/3.1 to dark Mylonite	203	20										
3.4	58	5.7389	61.6411	Dark mylonite from 3.3	182	10	272	70	260	60	Chlorite	3	normal	3	normal	small, several of these, slightly irregular
	59	5.7389	61.6411				280	67								weathered, lichen cover, no mineralisation to be seen
	60	5.7389	61.6411				206	90								
3.5	61	5.7678	61.6483	Dark mylonite from 3.3, very weathered	244	36	332	78	237	10	Chlorite	1	sinistral	1	sinistral	uncertain whether lineation is from foliation, very dark mineralisation, or is it just weathering?
	62	5.7678	61.6483				328	65	255	24	Chlorite	1	sinistral	1	sinistral	very uncertain as well!
	63	5.7678	61.6483		254	24	276	65	17	1	Chlorite	2	dextral	2	dextral	Climbing
3.6	64	5.7722	61.6494	Light/ pinkish Gneiss from 2.6	290	20	118	66	77	60	White and red Zeolite?	3	normal	3	normal	
	65	5.7722	61.6494		264	14	293	89	24	16	White and red Zeolite?	1	dextral	1	dextral	
3.7	66	5.7772	61.6606	Light Gneiss/Quartzite, very weathered	255	20	21	85								many, straight fractures, measured two examples
	67	5.7772	61.6606				194	85								
3.8	68	5.8022	61.6897	Dark Gneiss, mylonitic	163	90	163	90	254	25	Chlorite, white mineral?	2	sinistral	2	sinistral	uneven, only fracture with mineralization; strongly foliated/folded, fract = fol

3.9	69	5.8919	61.7372	Mica rich Gneiss	328	39	107	86								
	70	5.8919	61.7372				72	82								
	71	5.8919	61.7372				68	71								
	72	5.8919	61.7372				288	76								
	73	5.8919	61.7372		344	29	84	85								
4.1a	74	5.7847	61.6711	Gneiss, pink/darkish, well foliated	193	55	112	85			mossgreen (Chlorite ?), Fe, mica, Pyrite					
	75	5.7847	61.6711				310	60			Chlorite					
	76	5.7847	61.6711				101	46			Chlorite					
	77	5.7847	61.6711				288	75			Chlorite, Epidote?, Fe					
4.1b	78	5.7847	61.6717	Gneiss, same	194	75	300	80	32	20	white Zeolite? Or just host rock?	1	sinistral	1	sinistral	Almost the same location as 4.1a, walked a bit further for more measurements
	79	5.7847	61.6717				98	38			Chlorite					
4.2	80	6.0692	61.8197	Dark Gneiss	174	40	280	61	1	16	Chlorite, Fe	1				
	81	6.0692	61.8197				270	60								
4.3	82	6.0781	61.8150	Same dark gneiss	176	40	196	84								
	83	6.0781	61.8150				223	70								
	84	6.0781	61.8150				34	70								road parallel, big --> uncertain
	85	6.0781	61.8150				312	74								
	86	6.0781	61.8150				35	75								
	87	6.0781	61.8150				81	61								

	88	6.0781	61.8150				232	70	150	6	Chlorite, Fe (?)	1	dextral	1	dextral	
	89	6.0789	61.8144		170	20	276	55								
4.4	90	5.1358	61.9361	Gneiss	55	56	248	55								uncertain whether fracture = foliation, foliation folded here
4.5	91	5.1403	61.9367	Gneiss	266	11	245	76								several of these
	92	5.1403	61.9367				44	65								moss cover
4.6	93	5.1433	61.9375	Granulite			7	61			whitish/ red min., muscovite					big
4.7	94	5.0519	61.9431	Granitic gneiss	35	21	267	81	185	35	Epidote	1				
	95	5.0519	61.9431				283	76								compass unreliable (moisture)
	96	5.0519	61.9431				257	86			some epidote					
4.8	97	5.0542	61.9322	Granitic gneiss	75	25	76	88	166	10	Chlorite, muscovite	1	sinistral	1	sinistral	
4.9	98	5.0606	61.9286	Dark gneiss	102	20	310	90								
	99	5.0606	61.9286		80	15	311	80								
	100	5.0606	61.9286				260	75								
	101	5.0606	61.9286				123	90								